

Sustainable Civil Infrastructures

Jinwoo An  
Jizhe Zhang  
Juan Xie *Editors*

# New Approaches of Geotechnical Engineering: Soil Characterization, Sustainable Materials and Numerical Simulation

Proceedings of the 6th GeoChina  
International Conference on Civil &  
Transportation Infrastructures: From  
Engineering to Smart & Green Life Cycle  
Solutions – Nanchang, China, 2021



 Springer

# **Sustainable Civil Infrastructures**

## **Editor-in-Chief**

Hany Farouk Shehata, SSIGE, Soil-Interaction Group in Egypt SSIGE, Cairo, Egypt

## **Advisory Editors**

Khalid M. ElZahaby, Housing and Building National Research Center, Giza, Egypt

Dar Hao Chen, Austin, TX, USA

**Sustainable Civil Infrastructures (SUCI)** is a series of peer-reviewed books and proceedings based on the best studies on emerging research from all fields related to sustainable infrastructures and aiming at improving our well-being and day-to-day lives. The infrastructures we are building today will shape our lives tomorrow. The complex and diverse nature of the impacts due to weather extremes on transportation and civil infrastructures can be seen in our roadways, bridges, and buildings. Extreme summer temperatures, droughts, flash floods, and rising numbers of freeze-thaw cycles pose challenges for civil infrastructure and can endanger public safety. We constantly hear how civil infrastructures need constant attention, preservation, and upgrading. Such improvements and developments would obviously benefit from our desired book series that provide sustainable engineering materials and designs. The economic impact is huge and much research has been conducted worldwide. The future holds many opportunities, not only for researchers in a given country, but also for the worldwide field engineers who apply and implement these technologies. We believe that no approach can succeed if it does not unite the efforts of various engineering disciplines from all over the world under one umbrella to offer a beacon of modern solutions to the global infrastructure. Experts from the various engineering disciplines around the globe will participate in this series, including: Geotechnical, Geological, Geoscience, Petroleum, Structural, Transportation, Bridge, Infrastructure, Energy, Architectural, Chemical and Materials, and other related Engineering disciplines.

**SUCI series is now indexed in SCOPUS  
and EI Compendex.**

More information about this series at <http://www.springer.com/series/15140>

Jinwoo An · Jizhe Zhang ·  
Juan Xie  
Editors

# New Approaches of Geotechnical Engineering: Soil Characterization, Sustainable Materials and Numerical Simulation

Proceedings of the 6th GeoChina International  
Conference on Civil & Transportation  
Infrastructures: From Engineering  
to Smart & Green Life Cycle  
Solutions – Nanchang, China, 2021

 Springer

*Editors*

Jinwoo An  
Civil and Mechanical Engineering  
University of Mount Union  
Alliance, OH, USA

Jizhe Zhang  
School of Qilu Transportation  
Shandong University  
Jinan, China

Juan Xie  
School of Traffic  
and Transportation Engineering  
Changsha University of Science  
and Technology  
Changsha, China

ISSN 2366-3405

Sustainable Civil Infrastructures

ISBN 978-3-030-79640-2

<https://doi.org/10.1007/978-3-030-79641-9>

ISSN 2366-3413 (electronic)

ISBN 978-3-030-79641-9 (eBook)

© The Editor(s) (if applicable) and The Author(s), under exclusive license  
to Springer Nature Switzerland AG 2021

This work is subject to copyright. All rights are solely and exclusively licensed by the Publisher, whether the whole or part of the material is concerned, specifically the rights of translation, reprinting, reuse of illustrations, recitation, broadcasting, reproduction on microfilms or in any other physical way, and transmission or information storage and retrieval, electronic adaptation, computer software, or by similar or dissimilar methodology now known or hereafter developed.

The use of general descriptive names, registered names, trademarks, service marks, etc. in this publication does not imply, even in the absence of a specific statement, that such names are exempt from the relevant protective laws and regulations and therefore free for general use.

The publisher, the authors and the editors are safe to assume that the advice and information in this book are believed to be true and accurate at the date of publication. Neither the publisher nor the authors or the editors give a warranty, expressed or implied, with respect to the material contained herein or for any errors or omissions that may have been made. The publisher remains neutral with regard to jurisdictional claims in published maps and institutional affiliations.

This Springer imprint is published by the registered company Springer Nature Switzerland AG  
The registered company address is: Gewerbestrasse 11, 6330 Cham, Switzerland

# Introduction

This volume contains eight papers that were accepted and presented at the GeoChina 2021 International Conference on Civil & Transportation Infrastructures: From Engineering to Smart & Green Life Cycle Solutions, held in Nanchang, China, during September 18–19, 2021. The articles presented in this volume cover new approaches of geotechnical engineering introduced by researchers, engineers and scientists to address contemporary issues in geotechnical engineering such as the usage of sustainable materials in soil, soil characterization with new methods and numerical simulations to predict material properties. This information should lead to smart and green life cycle solutions in engineering. Various types of research were used in the various studies, including field measurements, numerical analyses and laboratory measurements. It is anticipated that this volume will support decisions regarding the optimal management and maintenance of civil infrastructures to support a more sustainable environment for infrastructure users.

# Contents

<b>CBR Strength of Treated Subgrade Soils</b> . . . . .	1
Hari Kumar Reddy Yarrapureddi, Gokhan Saygili, and Mena I. Souliman	
<b>HVSR and Site Characteristics of the Seismic and Strong-Motion Stations in Gansu Province, China</b> . . . . .	9
Xu Rong, Wang Lanmin, and Edward W. Woolery	
<b>Analysis of the Bearing Capacity of Press-in Pile with Installation Assistance into Stiff Ground</b> . . . . .	21
Naoki Suzuki and Yasumasa Kimura	
<b>On Earth Dam Leak Detection Based on Using Fiber-Optic Distributed Temperature Sensor (Case Study: Canal Embankment on the Rhône River, France)</b> . . . . .	44
P. Abbasimaedeh, M. Tatin, V. Lamour, H. Vincent, S. Bonelli, and A. Garandet	
<b>Comparative Evaluation of Morphometric Parameters on Runoff Estimation of Savitri Watershed, India</b> . . . . .	58
Sudarshan Bobade, Arun Dhawale, Vaibhav Garg, Anand Tapase, Digvijay Kadam, and N. K. Patil	
<b>Numerical Modeling of Excavation in Shanghai Soft Clays Using the New Small Strain Shanghai Constitutive Model</b> . . . . .	80
Afnan Younis Tanoli and Guan-lin Ye	
<b>Computational Studies of Passive Vortex Generators for Flow Control on High-Speed Train</b> . . . . .	95
Aqib Aziz, Yang Zhang, and Chen Gang	

**The Study on Extraction of Falling Rock Source Using Aerial Laser Data to Improve the Efficiency of Falling Rock Measures . . . . . 109**  
Yuqing Zhang, Koki Sakita, Satoshi Nishiyama, and Takeharu Sato

**Author Index. . . . . 117**



## About the Editors

**Dr. Jinwoo An** is an assistant professor of Civil and Mechanical Engineering in the School of Engineering at the University of Mount Union. He received his Ph.D. in Civil Engineering from the University of Central Florida in 2015 and his Master in Civil Engineering from the University of Texas at Austin in 2012. He is an experienced and energetic engineer, researcher and educator. He previously worked at a structural engineering company as an assistant engineer to finish a structural design of a multipurpose building with 29 floors (Macroscale). For his dissertation, he conducted a research on the mechanical and structural performance of cement composite materials, which incorporated sustainable materials (mesoscale). During his postdoctoral career, he deeply explored the effects of micro- and nanomaterials as additives in cement composite materials (micro- and nanoscale). He also authored, co-authored and edited more than 50 technical reports, journal and conference papers.

**Dr. Jizhe Zhang** is an associate professor of the School of Qilu Transportation, Shandong University. He is a professionally registered pavement engineer with a research interest in moisture damage of asphalt mixture, composite modification of bituminous materials, asphalt mixture recycling and solid waste utilization in asphalt pavement. He completed his graduate studies at the Wuhan University of Technology, China, and obtained his doctorate from the University of Nottingham, UK. He has published over 50 journal papers and ten conference papers. He is the young academic editor of the Journal of Traffic and Transportation Engineering (English Edition). He is a member of technical committee in the World Transportation Convention and a member of the expert committee of iFRAE 2021.

**Professor Juan Xie** is from School of Traffic & Transportation Engineering of Changsha University of Science & Technology. She completed her graduate studies at Donghua University (China) and Princeton University (The United States). She has published more than 20 journal papers and two academic monographs. Five of her national invention patents have been authorized, and one of them has been translated into actual production. She is the reviewer of many journals such as

Polymers, Materials, Frontiers in Materials and International Journal of Hydrogen Energy. Her research and practical interests include design and preparation of functional materials, new building materials, asphalt and modified asphalt technology and comprehensive utilization of material waste residue. She has completed a number of national, provincial and ministerial scientific research projects as the host. She has worked significantly on rubber powder modified asphalt and has been researching on molecular design and techniques to improve the performance of modified asphalt.



# CBR Strength of Treated Subgrade Soils

Hari Kumar Reddy Yarrapureddi<sup>1</sup>, Gokhan Saygili<sup>2</sup>, and Mena I. Souliman<sup>3</sup>✉

<sup>1</sup> Department of Civil Engineering, The University of Texas at Tyler, 3900 University Blvd, Tyler, TX 75701, USA

<sup>2</sup> Department of Civil Engineering, The University of Texas at Tyler, 3900 University Blvd, RBS 1007, Tyler, TX 75701, USA  
gsaygili@uttyler.edu

<sup>3</sup> Department of Civil Engineering, The University of Texas at Tyler, 3900 University Blvd, RBS 1008, Tyler, TX 75701, USA  
msouliman@uttyler.edu

**Abstract.** Calcium-based stabilizing agents have been extensively used to improve the engineering properties of base and subgrade layers of pavement systems. Recently, polymers and chemical stabilizers have become popular due to cost efficiency, ease of application, and fast curing times. This study presents a comprehensive laboratory testing program quantifying the strengths of treated subgrade soils. Here, the strength is defined in terms of California Bearing Ratio (CBR) values. The results of the CBR tests showed that non-traditional stabilizing agents significantly increased the strength characteristics of subgrade soils.

## 1 Introduction

A typical pavement structure consists of three layers including asphalt, base, and subgrade layers. The subgrade layer is made up of native soil and it acts as the foundation that provides stability to the pavement structure. Effectively designed pavements are expected to last for long periods but throughout the service life pavements experience distresses in terms of fatigue cracking (alligator cracking), rutting, bleeding, and potholes. Distresses significantly reduce the overall strength and durability of a pavement system and put additional costs on the rehabilitation and maintenance budgets of state and federal transportation agencies. Numerous researches are actively working on developing methods and products to increase the pavement resistance over distresses. The stabilization of subgrade and base layers improves the strength, compressibility, and durability characteristics of pavements.

Calcium-based stabilizers including cement and lime have been effectively used by the U.S. transportation departments. Cement stabilization depends on hydration products immediately created by the calcium silicates and calcium aluminates present in the cement itself. Excess free lime produced during hydration also allows for long term pozzolanic reactions to occur. Since base courses typically have low plasticity, cement is often used to improve the strength characteristics of these materials. Research findings also reveal that cement treated soils show a brittle behavior which is often the reason for shrinkage cracks in the stabilized layer. Reflection cracks through the asphalt

surfaces typically follow the same patterns as the cracks in a cement treated base [1]. Soluble sulfates present in soils can induce chemical reactions between cement/lime and residual soils resulting in significant loss of strength and heaving. Sulfates cannot be efficiently removed from the soil; therefore, non-traditional stabilizers have been recently recommended as alternative base stabilization products. Introduced as a non-traditional stabilizer for soil stabilization and erosion control, polymer and chemical stabilizers have become popular also due to cost efficiency, ease of application, and fast curing times. In this paper, an extensive laboratory testing program was executed to determine the CBR strength characteristics of subgrade soils after polymer and Claycrete (a chemical stabilizer) treatment. Parametric sensitivity analyses were carried out to evaluate the effects of subgrade soil type and stabilizing agent treatment levels.

## 2 Literature Review

In the literature, calcium-based stabilizers including cement and lime have been documented by numerous researchers. Kayak and Akyarli [2] studied the effects of lime on soil stabilization in clayey soil in the Ankara Province road in Turkey. In this study, 5% of lime by weight led to an increase in the CBR value by around 16 to 21 times for different type of clays. Similarly, Sariosseiri and Muhunthan [3] studied the use of cement to treat soils in the Washington state. Cement treatment showed significant improvement in the engineering properties. Particularly at 10% cement rate the soil samples showed relatively high unconfined compressive strength. Treated samples; however, showed more brittle response compared to untreated soils.

Non-traditional stabilizers including polymer and chemical admixtures have also been documented. For example, Hawakins et al. [4] proposed a method using chemical stabilizers named carboxylic acid and polyolefins for dust control and soil stabilization. A heterogeneous mixture was produced by blending the aliphatic or cyclic organic compounds with carboxylic acid. It was observed that polyolefins control the dust and improves the soil stiffness and modulus by more than 100%. It was reported that this chemical acts as a plasticizer and the penetration of this chemical helps for dust control. Recently, Srinath et al. [5] studied polymer binders to stabilize the subgrade soils. The primary objective of this study was to investigate the subgrade soils engineering properties in terms of physical, chemical, mechanical and microstructural properties and the results were utilized in the pavement design and analysis to determine their impact. The results showed a significant reduction in the subgrade rutting under high loading and different weather conditions. It was concluded that reduction in subgrade rutting helps for effective deformation transfer, subgrade to have longer bonding, and to reduce the rehabilitation costs. More recently, Hemant Gc et al. [6] investigated the significance of rubber and polymer in asphalt mix towards the pavement fatigue performance in terms of tensile strength and cost-effectiveness. In this study, three different mix designs such as conventional HMA mix, Asphalt Rubber (AR) and Polymer modified mix were adopted and these mixers were evaluated utilizing 3D move analysis software. It was observed that the utilization of modified mixtures significantly increases the service life of the pavements and more economical. From the results it was concluded that the AR mix has significantly increased the fatigue life and also it was cost effective (by 24 times compared to conventional HMA). It was observed that high speed and thick pavements

show much more significant results as the asphalt is much stronger at high frequency loadings.

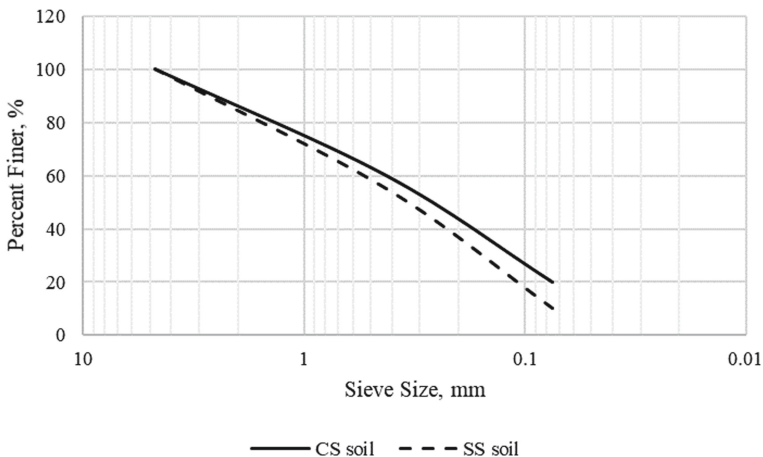
### 3 Objectives

Engineering properties of subgrade soils can be improved with the application of non-traditional stabilizing agents including polymer and chemical admixtures. The main objectives of this research are to compare the CBR strength properties of polymer and claycrete treated subgrade soils and to investigate the impact of different types of admixtures on the overall pavement performance.

### 4 Laboratory Testing Program

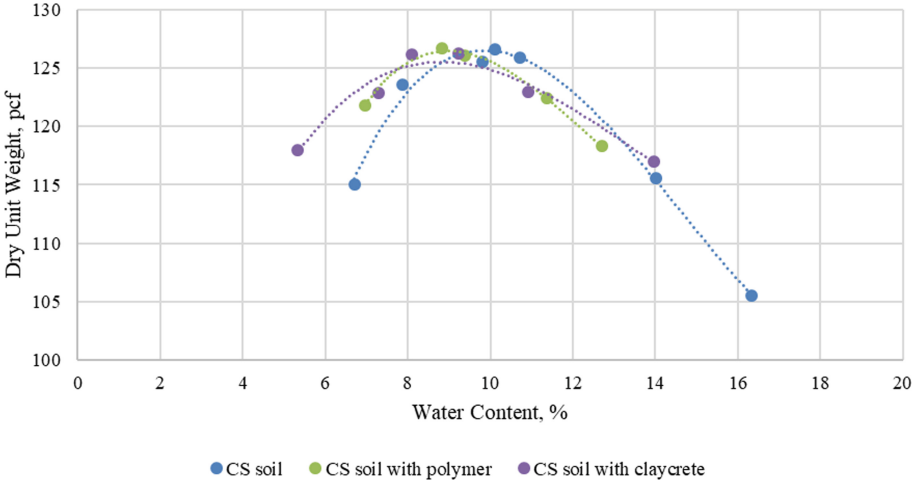
Laboratory investigations were based on two types of stabilizing agents including polymer and Claycrete. The polymer was in the form of aqueous dispersion. The pH value was around 4.5–5.5 and the density was around  $0.9982 \text{ g/cm}^3$  (68 °F or 20 °C). The specific gravity (relative density) was around 0.95–1.10, Water = 1 (liquid). Claycrete was used as a chemical stabilizer in the laboratory testing program. It is an ionic soil stabilizer which is designed especially for clay soils. The pH value was around 2.0 to 2.5. The specific gravity of claycrete was around 1.1. The flash point of the claycrete was greater than 61 °C. The polymer was provided by Terra Pave International which is located at the University of Texas at Austin.

Two commonly observed soil types were used in this study. They were labelled as Clayey Soil (CS) and Sandy Soil (SS). The gradation of the CS soil was chosen to be as 40% of retained soil in between sieve no.4 (opening size 4.75 mm) and sieve no. 40 (opening size 0.425 mm) plus 40% of retained soil between sieve no.40 and sieve no. 200 (opening size 0.075 mm) plus 20% of clay. The gradation of SS soil was chosen to be as 45% of retained soil in between sieve no. 4 and sieve no. 40 plus 45% of retained soil between sieve no. 40 and sieve no. 200 plus 10% of clay. The particle size distribution curves of CS and SS soils are given in Fig. 1.

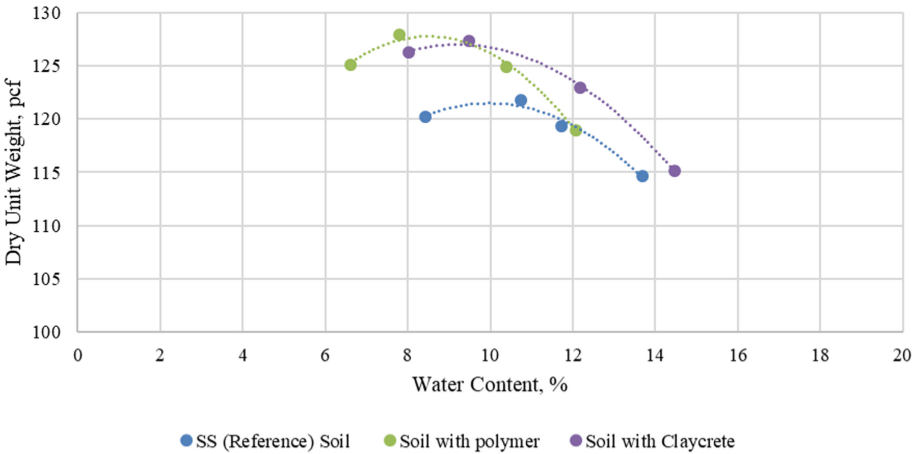


**Fig. 1.** Particle size distribution curves of CS and SS soils

Compaction curves of CS and SS soils are shown in Fig. 2 and Fig. 3. Figure 2 shows similar compaction characteristics for the treated and untreated CS soils. Therefore, a maximum dry unit weight of ~126.6 pcf and water content of ~10% was adopted for the testing program. In Fig. 3, however, the compaction curves of treated SS soils show around 5% increase in maximum dry unit weight and around 10% decrease in the optimum water content compared to the reference SS soil. An optimum moisture content of 10.5% for reference SS soil and 9.5% for treated SS soils were adopted for the testing program.



**Fig. 2.** Compaction curves of treated and untreated CS soils



**Fig. 3.** Compaction curves of treated and untreated SS soils

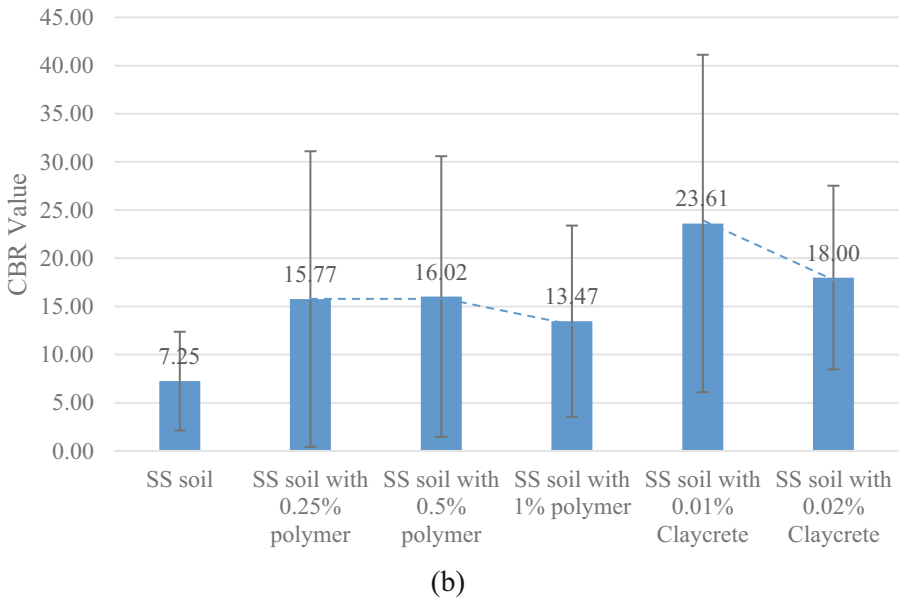
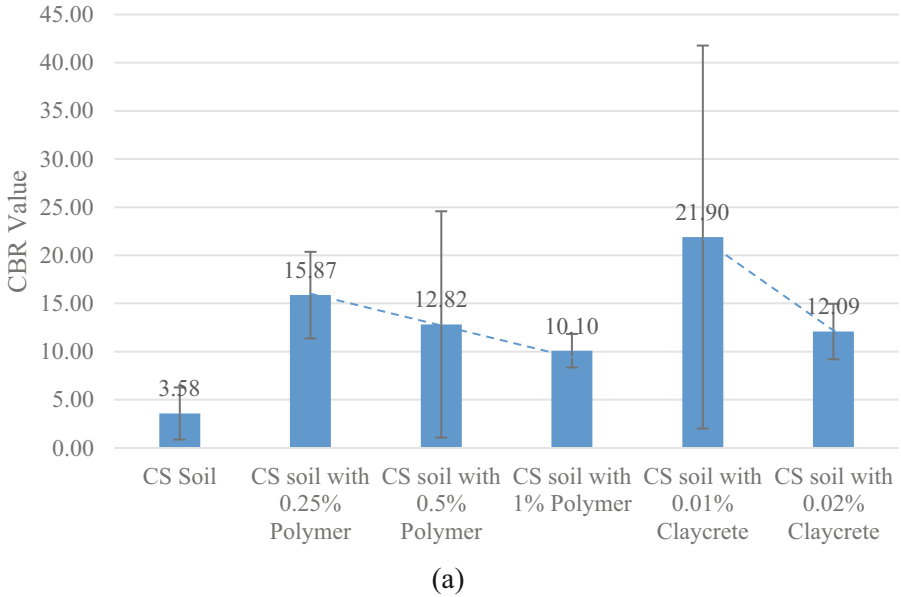
The CBR test is one of the most widely used penetration tests for determining the strength of subgrade soils ASTM D-1883 [7]. CBR results are typically used to determine

the total rutting and fatigue of pavements and the thickness of pavements. CBR values can be used to determine the resilient modulus of the subgrade soil which is a critical factor in predicting pavement rutting performance [9, 10]. In this laboratory testing program, CBR tests were performed on untreated and treated CS and SS samples. Here, polymer treated samples were prepared using 0.25%, 0.5% and 1% polymer by weight Saygili et al. [8]. Claycrete treated specimens were prepared using 0.01% and 0.02% claycrete by specimen weight (Claycrete Global Company, personal communication). Three specimens were prepared for each admixture type to minimize specimen bias. A total of 42 soil samples were prepared for the laboratory testing program. 24 h curing was adopted for this study (Fig. 4).



**Fig. 4.** Soil specimens before and after CBR test

CBR test results of CS and SS soils are shown in Fig. 5. Here, the average CBR values are presented together with 95% error bars. As shown in Fig. 5a, the results of CBR tests on reference specimens reveal that untreated CS soils have low load bearing capacity



**Fig. 5.** CBR results for (a) CS soils and (b) SS soils

with CBR values as low as around 4. It is observed that the 0.25% polymer treatment showed a significant improvement in the CBR by 4.5 times compared to untreated soils followed by 0.5% polymer treatment with 3.5 times and 1% polymer treatment with 3 times. It is observed that the 0.01% claycrete treatment increased the CBR significantly by 6 times compared to untreated soils followed by 0.02% claycrete treatment with 3.4



times. As shown in Fig. 5b, the results of CBR tests on reference specimens reveal that untreated SS soils have low load bearing capacity with CBR values as low as around 7. It is observed that the 0.5% polymer treatment showed a significant improvement in the CBR by 2.2 times compared to untreated soils followed by 0.25% polymer treatment with 2.1 times and 1% polymer treatment with 1.8 times. It is observed that the 0.01% claycrete treatment increased the CBR significantly by 3.3 times compared to untreated soils followed by 0.02% claycrete treatment with 2.5 times. However, the lower dosage rates can lead to field challenges, but the challenges can be overcome by utilizing the equipment such as reclaimer for uniform stabilization and to achieve a through mix of stabilizing agents to soil (Claycrete Global Company, n.d.). This kind of equipment are capable as stabilizer and recycler. As this paper focuses mainly on the laboratory assessment of CBR strengths of treated subsoils. The field operations are beyond the scope of this paper.

## 5 Conclusions and Recommendations

An overall comparison of the results suggests that polymer and claycrete treatment significantly increased the engineering properties of the subgrade soils. For CS soils, the optimum levels for polymer and claycrete treatment are 0.25% and 0.01%, respectively, whereas for SS soils the optimum level for polymer treatment increases to 0.5% but the optimum claycrete treatment level stays the same. This observation shows that claycrete is less sensitive to the particle size distribution of subgrade soils.

The trend lines between different treatment levels suggest that further increase in polymer and claycrete content will reduce the CBR values; however, actual testing is required to confirm the trend. The admixtures are viscous fluids. They are first mixed with water and then added to the soil for compaction. Without admixtures water acts as a “softening agent” which helps soil particles move into a more compact position. With admixtures added to water, it is possible that the binding process starts immediately and it prevents water to redistribute particles for a compact configuration. It can be speculated as the reason for a reduction in CBR strength with an increase in the admixtures treatment level. Further testing is necessary to verify this observation.

Typically, the performance of cement treated specimens exceeds the performance of specimens treated using non-traditional stabilizers; however, various research findings revealed that utilization of cement leads to additional shrinkage and reflection cracking due to cement’s brittle nature. Also, cement treated specimen may perform poorly by time as cement is prone to chemical attack.

## References

1. Adaska, W.S., Luhr, D.R.: Control of reflective cracking in cement stabilized pavements. In: 5th International RILEM Conference, Limoges, France, May 2004
2. Kayak, A., Akyarli, A.: A field application for Lime stabilization. *Environ. Geol.* **51**, 987–997 (2006). <https://doi.org/10.1007/s00254-006-0368-0>
3. Sariosseiri, F., Muhunthan, B.: Effect of Cement Treatment on Geotechnical Properties of some Washington State Soils. *Eng. Geol.* **104**(1–2), 119–125 (2009)

4. Hawkins, T.R., Beyersdorff, L.E., Vitale, R.W.: Method of chemical soil stabilization and dust control. United States Patent (2006)
5. Iyengar, S.R., Masad, E., Rodriguez, A.K., Bazzi, H.S., Little, D., Hanley, H.J.: Pavement subgrade stabilization using Polymers: Characterization and Performance. *J. Mater. Civil Eng.* **25**(4), 472–483 (2013)
6. Gc, H., Souliman, M.I., Zeiada, W., Isied, M.: Mechanistic Assessment of fatigue performance and cost analysis of pavement overlays: comparison between conventional hot mixed asphalt, Asphalt Rubber, and Polymer-Modified mixtures. *Adv. Civil Eng. Mater.* **8**(1), 611–622 (2019)
7. Standard Test Method for CBR (California Bearing Ratio) of laboratory-Compacted soils: ASTM D-1883, ASTM International Designation
8. Saygili, G., Yildirim, Y., Sahin, H.: Stabilization of high sulfate soils with non-traditional additives. *ASCE Libr.* (2018)
9. Rahman, M.M., Gassman, S.L.: Effect of resilient modulus of undisturbed subgrade soils on pavement rutting. *Int. J. Geotech. Eng.* **13**(2), 152–161 (2017)
10. Behiry, A.E.: Fatigue and Rutting lives in flexible pavements. *Ain Shams Eng. J.* **3**(4), 367–374 (2012)



# HVSR and Site Characteristics of the Seismic and Strong-Motion Stations in Gansu Province, China

Xu Rong<sup>1,2</sup>, Wang Lanmin<sup>1,2</sup>(✉), and Edward W. Woolery<sup>3</sup>(✉)

<sup>1</sup> China Earthquake Administration, Institute of Engineering Mechanics, Haerbin 150080, Heilongjiang, China

wanglm@gsdzj.gov.cn

<sup>2</sup> Earthquake Administration of Gansu Province, Lanzhou 730000, Gansu, China

<sup>3</sup> Department of Earth and Environmental Sciences, University of Kentucky, Lexington, KY 40506, USA  
ewoolery@uky.edu

**Abstract.** The horizontal-to-vertical spectral ratio (HVSR) method for seismic site characterization using microtremor and earthquake recordings has been widely employed since its introduction in 1989. We applied HVSR to analyze seismic and strong-motion earthquake S-waves in the Gansu province, China. The seismic stations were bedrock installations, whereas the strong-motion stations were installed on soils throughout the Province. Results show that most of seismic stations have no obvious predominant peak, but the strong-motion stations exhibit predominant peaks. Therefore, we corroborate HVSR as a cost-effective method to characterize ground-motion site effect caused by the near-surface soils.

**Keywords:** Horizontal-to-Vertical Spectral Ratio (HVSR) · Earthquake recordings · Microtremor · S-wave spectral analysis · Site effect

## 1 Introduction

The Horizontal-to-Vertical Spectral Ratio (HVSR) analysis has been widely used to characterize the shallow-subsurface seismic properties of engineering interest by single-station surface measurements. This approach to site effect characterization was proposed by Nakamura (1989) based on microtremor and earthquake recordings which overcome the difficulties of traditional method using a reference site or borehole data. The site effect is a common phenomenon during strong earthquakes and continue to be a significant subject for seismological research (Fleur et al., 2016; Woolery et al. 2016). HVSR gained popularity due to its simplicity in field acquisition and signal processing. Lermo and Chavez-Garcia (1993) applied the H/V method to earthquake S-wave recordings. Yamazaki and Ansary (2008) extended this approach to use of strong motion records to assess site characteristics or site classification and other applications. Dimitriu et al. (1998) and Bonilla et al. (2002) proved that the site predominant period obtained by different methods were basically consistent by comparing the H/V spectral ratio with

the traditional site characteristics research methods. Satoh et al. (2001) analyzed the differences of site characteristics among ground pulsation, P-wave, S-wave and tail-wave.

HVSR does not need ground models and can be applied to either microtremor or earthquake recordings; it only requires a single station recording. Along with the technical progress of digital strong vibration observation instruments, HVSR has been extended from ground pulsation to seismography and strong vibration recording since it was introduced in 1989. It is not only cost-effective but applicable in many kinds of field conditions, and has been the focus of numerous investigations (Roberto et al. (2007); Picotti et al. (2017); Neroni et al. (2018)). However, recent studies (Carpenter et al. (2018); Kawase et al. (2019); Wang et al. (2019); Chuanbin et al. (2020)) have shown that HVSR also has some limitations.

We applied HVSR in this study to analyze site characteristics of the seismic and strong-motion stations in Gansu province, China.

## 2 Horizontal-to-Vertical Spectral Ratio (HVSR)

Nakamura (1989) defined the HVSR as the ratio between the horizontal Fourier amplitude of motion and vertical Fourier amplitude of motion recorded on soil at free surface:

$$HVSR_S = \frac{H_S}{V_S}, \quad (1)$$

where  $H_S$  and  $V_S$  are Fourier spectrum of horizontal and vertical components of recordings on soil at surface, respectively (Fig. 1). Nakamura (1989) also defined the horizontal transfer function,  $TF_H$ , as,

$$TF_H = \frac{H_S}{H_B}, \quad (2)$$

where  $H_B$  is Fourier spectrum of horizontal component of recording at top of bedrock (Fig. 1).

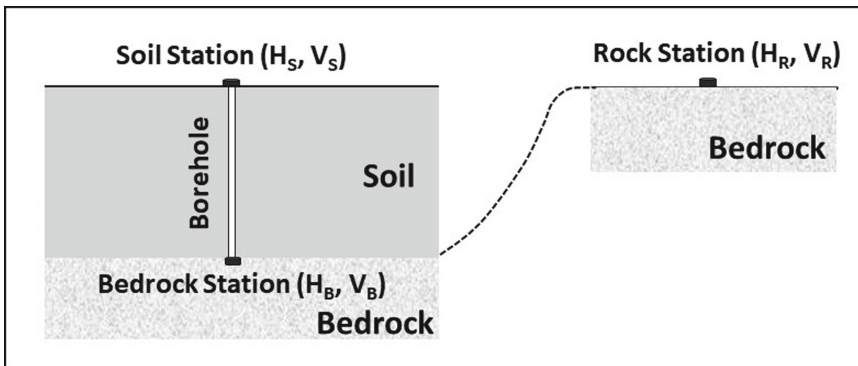


Fig. 1. Schematic diagram of soil, reference rock, and bedrock recordings.

Equation 2 can be rewritten as,

$$TF_H = \frac{H_S}{H_B} = \frac{H_S}{V_S} * \frac{V_S}{V_B} * \frac{V_B}{H_B}, \quad (3)$$

where  $V_B$  is Fourier spectrum of vertical component of recording at top of bedrock. The vertical component transfer function,  $TF_V$ , can be defined as,

$$TF_V = \frac{V_S}{V_B}, \quad (4)$$

and the HVSr at bedrock as,

$$HVSr_B = \frac{H_B}{V_B}, \quad (5)$$

Thus, Eq. 3 can be written as,

$$TF_H = HVSr_S * \frac{TF_V}{HVSr_B}, \quad (6)$$

As shown by Nakamura (1989),  $HVSr_B \approx 1.0$ , therefore, Eq. 6 becomes,

$$TF_H \approx HVSr_S * TF_V, \quad (7)$$

In traditional earthquake engineering, ground motion site effect is quantified by the site-to-reference spectral ratio (SSR) of the horizontal component of S-wave motion recorded on soil at surface and S-wave motion recorded on rock at surface (Borcherdt 1970) as.

$$SSR = \frac{H_S}{H_R}, \quad (8)$$

where  $H_R$  is the S-wave motions recorded on rock at surface (Fig. 1). And if the soil and rock sites are close enough, can be regarded as  $H_B \approx \frac{H_R}{2}$ ; then SSR is equal to,

$$SSR = \frac{TF_H}{2} = \frac{HVSr_S * TF_V}{2}, \quad (9)$$

Under the assumption of  $TF_V \approx 1.0$  (Nakamura, 1989), Eqs. 7 and 8 become,

$$TF_H \approx HVSr_S, \quad (10)$$

Thus, Nakamura (1989) proposed to use the  $HVSr_S$  to approximate the site effect with ambient noise and earthquake recordings.

The cost-effective simplicity of HVSR has led to wide use in site characterization investigations, particularly for engineering purposes. For example, Zare (1999) and Lee et al. (2001) classified the sites according to the predominant period by the strong vibration recordings in Iran and Taiwan, respectively. The advantages of this method are that it is not subject to the reference site, simple and easy to operate, and low cost. Rong et al. (2016) applied HVSR of weak S-wave motions as a tool to invert shear-wave velocity, comparing the theoretical results with this empirical method, and finding that HVSR resembles the empirical transfer function for nonlinear site response. Kassaras et al. (2017) similarly applied the HVSR method on free-field ambient noise measurements to define the site response characteristics of peak frequency and amplification.

However, HVSR also has limitations. For example, recent studies found that the assumption of  $TF_V \approx 1.0$  (Nakamura 1989) is not valid, particularly at higher resonance modes (Carpenter et al. 2018, 2020 Kawase et al. 2019; Chuanbin et al. 2020). It has also found that the ambient-noise HVSR is different from earthquake S-wave HVSR: ambient-noise HVSR results from the ellipticity of the fundamental Rayleigh wave, whereas S-wave HVSR results from the S-wave resonance (Carpenter et al. 2018, 2020; Wang et al. 2019 Carpenter et al. 2018) found that  $TF_V$  is approximately equal to 1.0 at lower resonance modes (up to the fifth resonance mode), at the fundamental mode frequency in particular. Thus, we can utilize the  $HVSR_S$  to study the fundamental frequency (or predominant site period).

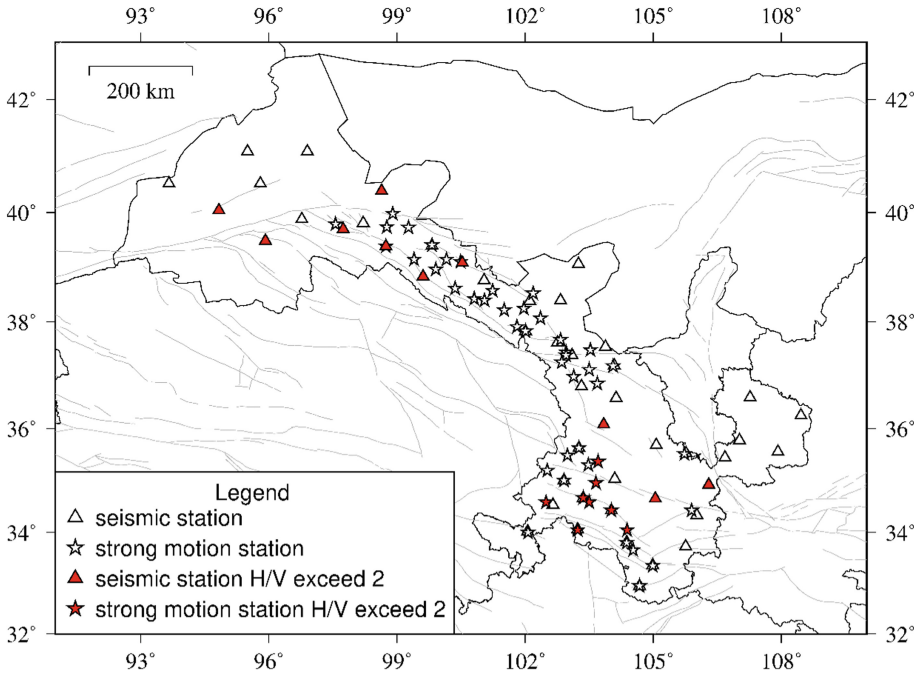
### 3 Data and Processing

Figure 2 shows the seismic and strong-motion stations in Gansu Province, China. The seismic stations are installed on rock and instrumented with three-component medium to long period velocity seismometers. All seismic data with a rate of 100 samples per second are transmitted to the Gansu Seismic Network Center in Lanzhou for analysis. As a part of China Strong Motion Network, the strong-motion stations in Gansu Province are installed on soil. Strong-motion data with a rate of 200 samples per second are transmitted to the China Strong Motion Network Center in Beijing for analysis.

For seismic data, the principles for selecting seismic records are as follows: ① Earthquake records with magnitude  $\geq M_w$  3.3 between 2017 and 2019; ② Screening out seismic waveform features are obvious and includes complete waveform of noise segment, P-band and S-band; ③ Filtering and S-wave picking the records with a complete S-wave seismic phase.

55 seismic event waveforms that satisfy these conditions were selected in seismic database. As for strong motion data, due to the small number of records and the low signal-to-noise ratio in many cases, it is more difficult to filter. However, basic principles for strong-motion filtering are the same as seismic data, but only the first criteria is changed to events recorded since 2008, and the seismograph is triggered by earthquake records with magnitude  $\geq M_w$  4.9. Ultimately, only 20 seismic records were chosen.

The data are converted to a usable format for removing mean value, linear trend, and waveform pinching. Deconvolution is applied by a script to remove the instrument response from the waveforms, and perform simple filtering utilizing suppress the low and high frequency parts of the waveforms. The Taup software is subsequently used



**Fig. 2.** Seismic and strong-motion stations in Gansu Province, China

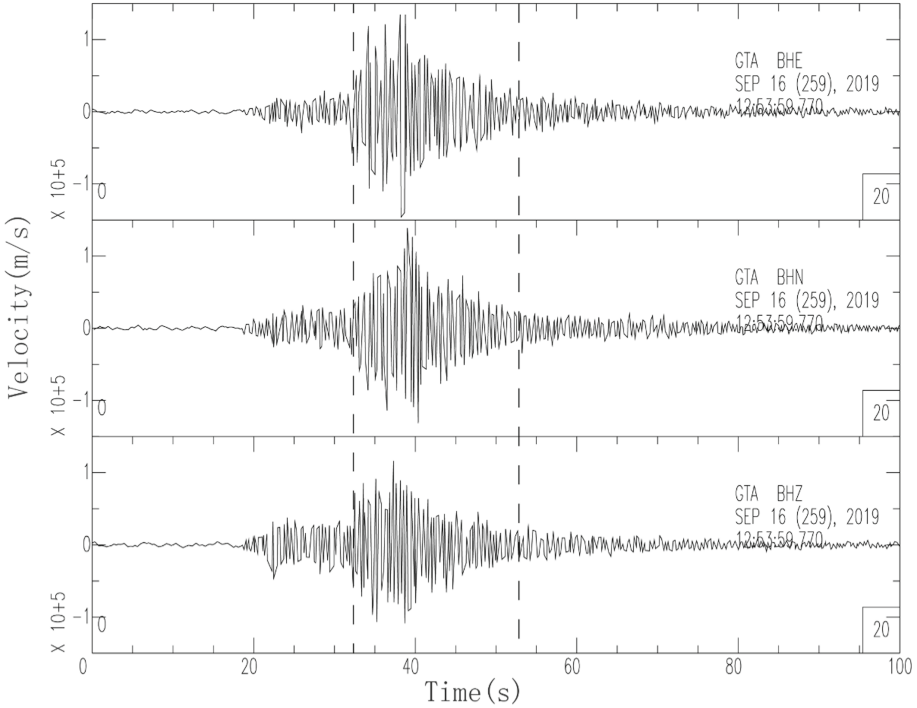
to calculate seismic travel time and determine the initial arrival time of P-wave and S-wave seismic phases, then cut out S-wave band (Fig. 3). Fourier amplitude spectrum was calculated for the windowed S-wave seismic phase. A Hanning filter was used to smooth the amplitude spectrum in order to better identify the predominant period of the site. Processing parameters shown Table 1.

**Table 1.** Parameter selection during seismic data processing

$t_{\text{pre-p}}$ (s)	$t_{\text{win}}$ (s)	Taper (%)	$f_{\text{lo}}/f_{\text{hi}}$ (Hz)	$f_{\text{smooth}}$ (Hz)
21	21	5	0.05/40	0.5

An important step for the strong-motion data is baseline correction that minimizes or eliminates baseline drift caused by background noise, instrument noise, and instrument tilt. Processing parameters are shown Table 2. For the sake of accuracy and operability, manual picking method is selected, which need visually inspect each recording and determine the S-wave window through the daily work experience. The other steps are the same as data used for seismic data processing.

More rigorous data screening requires Single-to-Noise (SNR) calculation. That is the ratio of the amplitude spectrum of signal and noise. In this paper, in order to select high-quality recordings of weak motions to avoid contaminating the spectral ratios and



**Fig. 3.** S-wave window of GaoTai (GTA) station in ZhangYe 5.0 earthquake on 2019.9.16 (in the picture: BHE, BHN, BHZ represent three components of broadband high resolution recording. B represent broadband, H represent high sensitivity, E,N,Z represent E-W,N-S,and vertical, respectively.).

**Table 2.** Parameter selection during data strong-motion processing

$t_{pre-p}$ (s)	$t_{win}$ (s)	Taper (%)	$f_{lo}/f_{hi}$ (Hz)	$f_{smooth}$ (Hz)
10	10	5	0.05/40	0.5

their averages with noise, the SNR threshold for each component is set to be greater than 2.5 (Fig. 4). The 2.5 was chosen because this is the normal threshold for seismic data processing.

$$HS = \sqrt{ST^2 + SR^2} \quad (11)$$

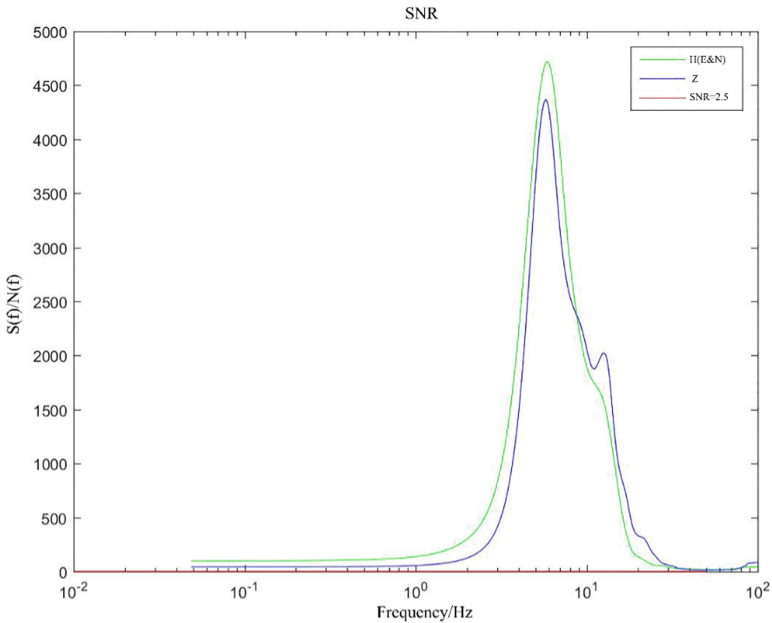
$$HN = \sqrt{NT^2 + NR^2} \quad (12)$$

$$SNR = HS/HN \quad (13)$$

$HS$  Represents the synthetic horizontal signal information,  $HN$  is the synthetic horizontal noise information.  $ST$  and  $NT$  are the radial component of the signal and



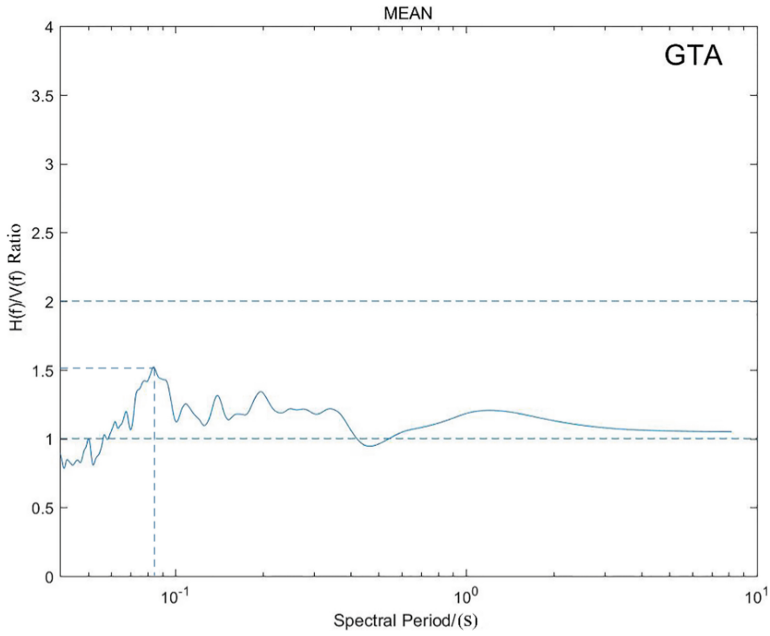
noise, respectively.  $SR$  and  $NR$  are the transverse component of the signal and noise, respectively.



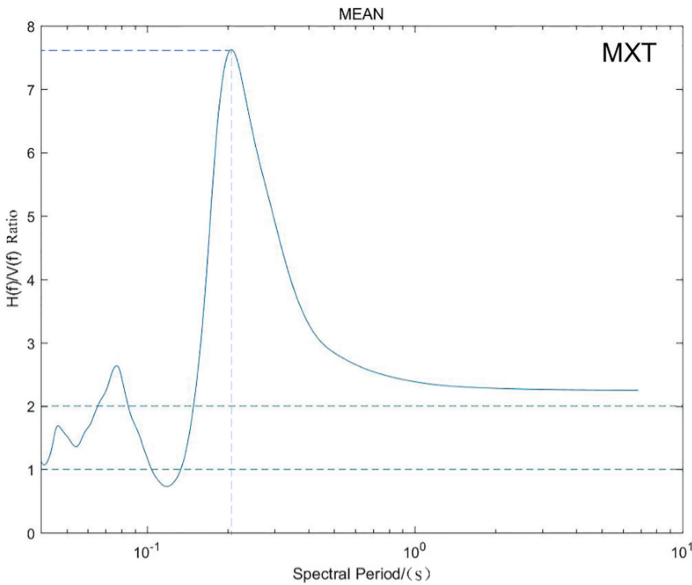
**Fig. 4.** Signal-to-Noise ratio of three component all larger than 2.5

## 4 HVSR Analysis and Results

Each seismic station had no less than 6 available seismic event records. An average of the HVSR results for the different seismic events was used to obtain the representative site HVSR amplitude spectrum ratio curve. Only 40 seismic stations obtained reasonable HVSR results. The strong motion stations having fewer records, thus we considered no less than 3 seismic event records for each. Only 8 fixed strong motion stations produced an average amplitude spectrum ratio curve with these constraints. As an example, Fig. 5 shows HVSR for the seismic station GTA where the predominant site period is not obvious. Figure 6 is the HVSR for the strong-motion station MXT, which shows a clear predominant site period at approximately 0.21s.



**Fig. 5.** HVSR at Seismic Station GaoTai (GTA).



**Fig. 6.** HVSR at Strong-motion Station Minxian (MXT).

The predominant site periods and peak ratios of the 40 seismic stations are listed in Table 3. The peak ratios at most seismic stations (30/40) are generally less than 2.0.

However, there are a few seismic stations (10/40) with higher peak ratios. The results of strong motion stations are significantly different from those of seismic measurements. The amplitudes are all larger than 2.0, some even reach 7.8, suggesting the site amplification effect is significant. The predominate periods for the strong motion stations are larger than the seismic stations, which can be explained by the site conditions (Table 4).

**Table 3.** Results of seismic stations

Station	Predominant site period	Peak ratio
GTA	0.08	1.5
AXX	0.2	2.0
BYT	0.1	1.5
CHM	0.18	1.8
CXT	0.07	1.6
DBT	0.35	1.8
DHT	0.07	2.5
GLT	0.13	2.0
HJT	0.18	1.6
HXP	0.10	2.0
HYS	0.20	2.0
HZT	0.25	1.9
JFS	0.20	2.5
JNT	0.07	1.8
JTA	0.70	1.6
JYG	0.09	1.5
LQT	0.12	1.8
LTT	0.10	1.5
LXA	0.06	1.8
LYT	0.11	1.0
LZH	0.20	2.5
MIQ	0.12	1.5
MXT	0.25	1.8
QTS	0.18	3.0
SBC	0.30	3.2
SDT	0.80	1.7
SGS	0.20	1.5
SGT	0.25	1.7
SNT	0.40	2.8
TSS	0.18	1.7
WDT	0.10	1.8
WSH	0.40	5.0
WXT	0.13	1.8
WYT	0.30	1.8
YDT	0.08	1.5
YJZ	0.25	5.8
YWX	0.18	1.3
ZHC	0.08	2.5
ZHQ	0.17	1.9
ZHY	0.15	2.5

**Table 4.** Results of strong-motion stations

Station	Predominant site period	Peak ratio
DLA	0.5	3.0
DIB	0.3	2.5
KLE	0.13	2.4
LUQ	0.18	3.2
MXT	0.25	7.8
YLG	0.13	3.8
ZM2	0.07	2.9
ZNI	0.20	3.0

## 5 Discussion

The peak ratios at most seismic stations (30/40) are generally less than 2.0. However, there are a few seismic stations (10/40) with higher peak ratios (Fig. 2). As shown in Fig. 5 relative flat and the peak ratio  $<2.0$ , while in Fig. 6 there is a single distinct dominant peak, and the peak ratio even reach to 7.8, which can be explained by site dynamic amplification effect. That is the larger peak ratio, the more obvious amplification effect in site.

For the Gansu seismic station the fundamental amplitude changes little, but the shape of HVSR curve and peak period  $T_P$  for the stations vary significantly.  $T_P$  of some station is very obvious, for example DBT, QTS, SBC, WSH and so on; these stations are on the bedrock, with thin relatively simple soil veneers. Other stations such as JTA, JNT, LQT and other HVSR curves do not have peak period at all. The reason may be that these stations are located on the unweathered bedrock and the site effect is relatively weak, so the HVSR amplitude tends to 1.0. However, there are stations HVSR curve amplitude changes a lot, such as station WSH where the peak period reached 5.0, but it is located in the loess covered area in the southeast of Gansu province. While the basic bedrock is glutenite, due to the larger surrounding soil coverage, a site amplification effect may occur. Also, there may be of various compositions of bedrock with differing velocity that may contribute to the response. The amplitude of LYT station was lower than 1.0, the platform data showed that although the platform was granite, it was built in a semi-basement, which was likely to cause the calculated velocity in the bedrock to decrease, thus explaining the phenomenon that the amplitude was lower than 1.0.

The results of strong motion stations are significantly different from those of seismic measurements. The amplitudes are all larger than 2.0, some as large as 7.8 (Fig. 2), suggesting an obvious site amplification effect.

The strong-motion stations show much more complex responses, with three main attributes: first, some stations have obvious peak predominant period, we think that the base soil layer of these stations is a relatively simple single lithology; second, the peak predominant period of some stations is very diffuse, it is likely related to a much more complex subsurface lithology; third, some stations have two peak predominant periods,

suggesting the lithology is divided into two types. The peak predominant period is clearly related to the site lithology, however.

## 6 Conclusions

We applied HVSR to analyze earthquake S-waves of the recordings from the seismic and strong-motion stations in Gansu province. The seismic stations were installed on rock, and the strong-motion stations were installed on soil overburden. Our results show that most of seismic stations (i.e., 30 of 40) have no obvious predominant peak, which is consistent with general observation of  $HVSR \approx 1.0$  for a station on rock. Our results also show that the strong-motion stations have an obvious predominant peak. Thus, our results demonstrate and corroborate that HVSR can be effectively used to characterize the ground-motion site effect.

Whereas this study only uses weak motion, not strong motion that is of engineering interest. In this paper suggests that single station S-wave HVSR can be used to obtain the fundamental site frequency that is of engineering interest, we can speculate that this method will be more useful when more and more strong motion data become available in Gansu, as well as China.

**Acknowledgment.** We thank the China Strong Motion Network Center for the data support. We thanks for the fund supported by Special Fund for Innovation Team, Gansu Earthquake Agency (2019TD-02-01); Earthquake Science and Technology Development Fund, Gansu Earthquake Agency (2020M02) and Earthquake Tracking and Directional Work Task for 2021 (2021010110).

## References

- Bonilla, L.F., Steidl, J.H., Gariel, J.C., et al.: Borehole response studies at the garner valley downhole array, Southern California. *Bull. Seismol. Soc. Am.* **92**(8), 3165–3179 (2002)
- Borcherdt, R.D.: Effects of local geology on ground motion near San Francisco Bay. *Bull. Seismol. Soc. Am.* **60**, 29–61 (1970)
- Carpenter, N.S., Wang, Z., Woolery, E.W., et al.: Estimating site response with recordings from deep boreholes and HVSR: examples from the Mississippi Embayment of the Central United States. *Bull. Seismol. Soc. Am.* **108**(3A), 1199–1209 (2018)
- Carpenter, N.S., Wang, Z., Woolery, E.W., et al.: An evaluation of linear site-response parameters in the central and eastern united states and the importance of empirical site-response estimations. *Bull. Seismol. Soc. Am.* **110**(2), 489–507 (2020)
- Dimitriu, P.P., Papaioannou, C.A., Theodulidis, N.P.: EURO-SEISTEST strong-motion array near Thessaloniki, Northern Greece: a study of site effects. *Bull. Seismol. Soc. Am.* **88**(3), 862–873 (1998)
- Kawase, H., Nagashima, F., Nakano, K., et al.: Direct evaluation of S-wave amplification factors from microtremor H/V ratios: Double empirical corrections to “Nakamura” method. *Soil Dyn. Earthq. Eng.* **126**, 105067 (2019)
- Kassaras, I., Papadimitriou, P., Kapetanidis, V., Voulgaris, N.: Seismic site characterization at the western Cephalonia Island in the aftermath of the 2014 earthquake series. *Int. J. Geo-Eng.* **8**(1), 1–22 (2017). <https://doi.org/10.1186/s40703-017-0045-z>

- Lee, C.T., Cheng, C.T., Liao, C.W., et al.: Site classification of Taiwan free-field strong-motion stations. *Bull. Seismol. Soc. Am.* **91**(5), 1283–1297 (2001)
- Lermo, J., Chavez-Garcia, F.: Site effect evaluation using spectral ratios with only one station. *Bull. Seismol. Soc. Am.* **83**, 1574–1594 (1993)
- Nakamura, Y.: A method for dynamic characteristics estimation of subsurface using microtremor on ground surface. *Q. Rep. Railway Tech. Res. Inst.* **30**(1), 25–33 (1989)
- Neroni, R., Stephens, K., Dwumfour, D.: Application of the passive seismic Horizontal-to-Vertical Spectral Ratio (HVSr) technique for embankment integrity monitoring. *ASEG Extended Abstracts* **1**, 1–6 (2018)
- Picotti S.A, Francese R.B, Giorgi M.A., et al.: Estimation of glacier thicknesses and basal properties using the horizontal-to-vertical component spectral ratio (HVSr) technique from passive seismic data. *J. Glaciol.* **63**(238), 229–248 (2017)
- Roberto, C., Petra, M., Fausto, B., et al.: Improvement of HVSr technique by wavelet analysis. *Soil Dyn. Earthq. Eng.* **28**(4), 321–327 (2007)
- Rong, M.S., Wang, Z.M., Woolery, E.W., et al.: Nonlinear site response from the strong ground-motion recordings in Western China. *Soil Dyn. Earthq. Eng.* **82**, 99–110 (2016)
- Satoh, T., Kawase, H., Matsushima, S.: Differences between site characteristics obtained from microtremors, S-waves, P-waves, and codas. *Bull. Seismol. Soc. Am.* **91**(2), 313–334 (2001)
- Wang, Z., Carpenter, N.S., Woolery, E.W.: Horizontal-to-vertical spectral ratio of S-waves and SH-wave transfer functions at the vertical seismic and strong-motion arrays in the Central United States. *J. Appl. Geophys.* **160**, 64–71 (2019)
- Woolery, E.W., Wang, Z., Carpenter, N.S., Street, R., Brengman, C.: The Central United States Seismic Observatory: site characterization, instrumentation, and recordings. *Seismol. Res. Lett.* **87**, 215–228 (2016)
- Yamazaki, F., Ansary, M.A.: Horizontal-to-vertical spectrum ratio of earthquake ground motion for site characterization. *Earthq. Eng. Struct. Dyn.* **26**(7), 671–689 (2008)
- Zare, M., Bard, P., Ghaforyashtiany, M.: Site characterizations from the Iranian strong motion network. *Cancer Res.* **71**(89), 74–94 (1999)
- Zhu, C., Marco, P., Fabrice, C.: Evaluation of a novel application of earthquake HVSr in site-specific amplification estimation. *Soil Dyn. Earthq. Eng.* **139**, 106301 (2020)



# Analysis of the Bearing Capacity of Press-in Pile with Installation Assistance into Stiff Ground

Naoki Suzuki<sup>(✉)</sup> and Yasumasa Kimura

Press-in Technologies Support Department, GIKEN Ltd., Tokyo, Japan  
suzuki.n@giken.com

**Abstract.** Press-in piling method enables displacement piles to be installed with little noise and vibration. Though installations into hard grounds require installation assistance such as water-jetting, augering, and rotary-cutting, the effect of these techniques on the bearing capacity has not been clear. This paper collects loading tests of steel pipe piles installed by the press-in piling with the assisted techniques and studies the axial performance. The test results of the load-settlement curves and unit resistances suggest that standard press-in and rotary cutting press-in pile have similar mechanisms with driven pile. Water-jetting decreases shaft resistance and varies base resistances, and the load-settlement curve resembles that of the bored pile. Finally, the estimated ultimate resistance coincides with the measured ones well, based on the proposed characteristic values. These results can supply basic information to design pile foundations with press-in piling.

## 1 Introduction

Press-in piling is one of the steel pipe pile installation methods with hydraulic force (Fig. 1). Since impact/vibratory driving are difficult to be adapted in residential areas because of the noise and vibration, inner excavation (as known as bored pile) and screw piling are becoming to be used for steel pipe pile installation in Japan (e.g. Koda 2019). Since press-in piling method enables displacement piles to be installed with little noise and vibration, and is also environmentally friendly, recently it has been used for pile foundations.

Assistant techniques of press-in piling into the dense ground include water jetting, augering, and rotary cutting (Fig. 2). Although the axial performance of assisted press-in piles has not been proven, there has been strong demand for usage especially in urban areas where noise and vibration problems are a concern and where the site conditions are restricted, such as under bridge piers. The axial performance depends on the piling methods and has been analyzed statistically (e.g. Paikowsky 2004, Nishioka et al. 2008, Nanazawa et al. 2019, Kitamura et al. 2019). Although we also reported on those of the rotary cutting press-in (Suzuki et al. 2019), there was no report summarizing the bearing performance of other assisted press-in pile.

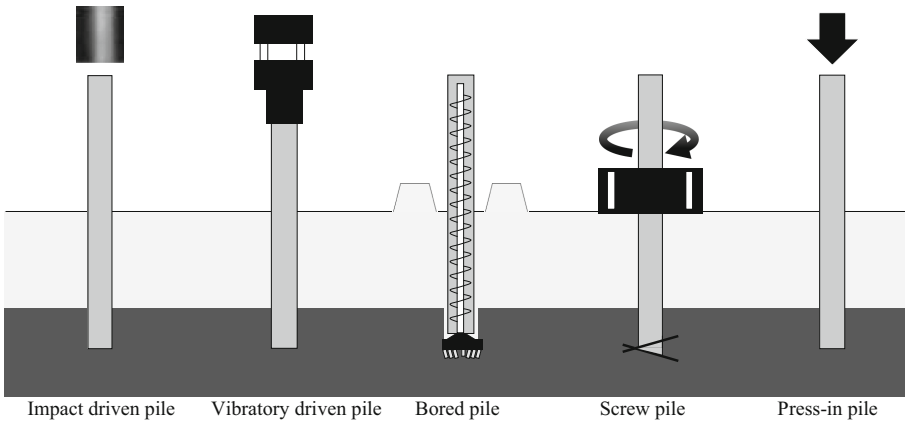


Fig. 1. Types of installation methods of steel pipe piles

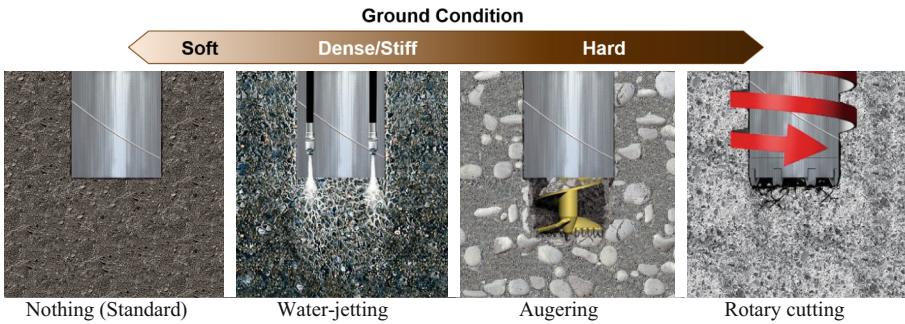


Fig. 2. Illustrative assistant techniques of press-in pipe piles (after GIKEN (2020) online)

This paper collects and analyzes loading test results to grasp the performance of the assisted press-in pile. It also investigates the relationship between the base resistance and the shaft resistance and the ground (N-value and type).

## 2 Press-in Piling and Its Assistant Techniques

This section introduces an overview of the press-in piling assistance and researches on its influence on the bearing capacity. More details, such as installation procedure, applicable N-value and pile length, are described in IPA (2016). Also, this paper calls press-in piling that does not use any assistance, standard press-in.



## 2.1 Standard Press-in

Standard press-in piling, as known as jacking or pressing, is a method of installing piles without the use of augers, water jets, or rotary-cuts as described below. Many studies on bearing capacity have been conducted (e.g. White and Deeks 2007, Zarrabi and Eslami 2016), and reported that jacked piles have higher stiffness and bearing capacity than driven piles.

Press-in piling which this paper introduces conducts installations and extractions of piles alternately with reaction force by installed piles (Fig. 3). This action, as known as “surging”, reduces shaft resistance during penetration (White and Deeks 2007). Aizawa et al. (2018) also reported that the cyclic loadings reduce the resistance of open-ended pipe pile during penetration both in saturated ground and in dry sand.



a) Self-walking system  
(as known as SILENT PILER)



b) System that a piling machine stretches its arm to sheet piles to obtain reaction force (OS1-3)

**Fig. 3.** Types of press-in piling system (GIKEN 2016)

Besides, the plug of open-ended piles depends on many factors, soil type, pile size, particle crushing, and loading speed (e.g. Yamahara 1964, Randolph et al. 1991, White et al. 2000, Suriyah et al. 2011, Paik et al. 2004), and it has not been clearly understood. Furthermore, these studies had relatively small piles, diameters of 300 mm at most. Since the plug, which is evaluated by the base resistance or inner soil movements, decreases as the pile diameter increase (Kikuchi et al. 2009), researches with larger pile diameters are necessary.

## 2.2 Water Jetting (WJ)

Water-jetting is a very efficient method of pile penetration (Tsinker 1988). Its penetration mechanism and impact on the surroundings have been investigated even in recent years (e.g. Shepley 2013, Gillow et al. 2018, Passini et al. 2018).

On the other hand, the effect of water jets on the resistance of press-in piles has not been understood yet, though various Japanese guidelines and manuals (JRA 1999, RTRI 2014, Society for Vibratory hammer 2015) have introduced reduction factors for vibratory driven pile based on full-scale loading tests (Table 1).

**Table 1.** Reduction factors of the bearing capacity for WJ in Japanese guidelines

Reference	Pile type	Reduction factor*		Installation method to compare
		Base resistance	Shaft resistance	
JRA 1999	Sheet pile/pipe pile	0	0.5	Driven pile
RTRI 2014	Sheet pile	1	0.33	Vibratory driven H-shaped pile
RTRI 2014	Sheet pile with Closed Section at Bottom	0.33–0.5**	0.33	Impact driven pile***
Society for Vibratory Hammer 2015	Pipe pile	0.33–0.56**	0.5	Vibratory driven pile

Note: This table doesn't intend a comparison between the guidelines, because the quality controls differ between the manuals

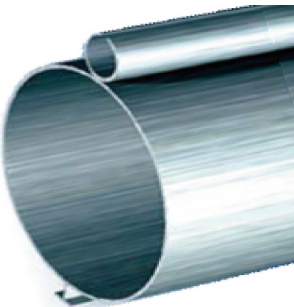
\* The factors are ratios of the resistance between piles installed by water-jetting and those by the installation method to compare.

\*\* It depends on the N-value and the embedded depth in the bearing layer.

\*\*\*Open-ended driven piles (pile diameter,  $D < 0.8$  m, embedded depth into the bearing layer is  $3D$ )

Water is injected downward from the tip of a steel pipe pile through 2–4 water hoses installed on the outer circumference of the pile. The amount of water is determined empirically by piling contractors, and the amount was about 1500–3600 L/min (as shown in Table 4a and 4b of Appendix).

WJ press-in pile in this paper had interlocks (Fig. 4a). Also, some were tested in the condition that interlocks were joined with those of next piles, and interlock resistances were observed and estimated during piling (Table 4a and 4b).



(a) Pipe pile with interlocks (for WJ press-in pile in this paper)



(b) Cutting bits and water pipe of rotary press-in pile

**Fig. 4.** Steel pipe pile (after IPA 2016)

### 2.3 Augering

An auger and a casing are installed simultaneously with the pipe pile. It drills hard grounds at the pile toe with axial press-in force and creates a hollow space. After the pile is installed and the auger is extracted, final push-in is generally conducted to get enough base resistance.

### 2.4 Rotary Cutting

The rotary cutting press-in piling penetrates a pile with cutting bits on the tip by applying axial and rotational jacking force simultaneously (Fig. 4b). The tip protrudes a maximum of 9–12 mm from the outer diameter of the steel pile, which is the same size as friction cutters of the bored pile (JRA 2017). A small amount of water (less than 150 L/min, as shown in Table 4a and 4b) is injected near the pile tip. This assistant technique expands press-in application for reinforced concrete as well as hard ground, though steel pipe piles with interlock are not applicable because of rotational procedures.

Though pile rotation during penetration greatly reduces shaft resistance as well as surging (Ishihara et al. 2015, Galindo et al. 2018), shaft resistance is expected to recover after curing periods. However, it has been also reported that the stiffness of shaft resistance does not increase with increasing N-value in dense gravel layers (Suzuki et al. 2019), and additional studies are required.

## 3 Test Cases and Analysis Methods

### 3.1 Overview

This section introduces load tests of steel pipe piles and summarizes their test conditions (Table 4a and 4b). The total number of tests is 36, which includes a static load test, statnamic load test, dynamic load test, and pull-out test (Table 2). WJ has been applied mostly at sites where the pile length is long; the embedded depth is about 25–50 m for WJ piles, while about 10–25 m for other piles. It can influence the ratio of the base resistance and the pile behavior.

**Table 2.** Number of axial loading tests of steel pipe piles

	Pull-out	Dynamic	Statnamic	Static	Subtotal
Standard	0	0	0	4	4 (0)
WJ	0	5	2	7	14 (2)
Augering	0	0	0	2	2 (0)
Rotary	1	0	10	5	16 (5)
Subtotal	1	5	12	18	36 (7)

Note: () in subtotal represents the number of the tests which measured pile tip settlement and ultimate behavior (that is the maximum settlement is more than 10% pile diameter)

### 3.2 Ground Conditions

Figure 10 in appendix shows the soil classification and N-value of the tests which was not described by the previous works shown in appendix, Table 4a and 4b.

### 3.3 Analysis Method

Firstly, load-settlement curves of static and statnamic tests were compared with the average behavior of impact driven pile and the bored pile with steel casing. Then, based on static and dynamic tests, the relationship between the ground (type and N-value) and the ultimate base and shaft resistance was presented and compared with that of the driven pile, JRA (2017). Finally, the penetration mechanisms were drawn, and ultimate resistances were checked using the proposed characteristic value.

The unloading point method (UPM, Middendorp et al. 1992) was used to obtain an equivalent static pile response from statnamic tests. In dynamic tests, signal-matching analysis with Case Pile Wave Analysis Program (CAPWAP, Rausche et al. 1972) was conducted to analyze and obtain soil resistance.

Also, the ultimate resistance was defined as the load causing the settlement of the pile head equal to 10% of the pile diameter in this paper, instead of that of the pile tip, to ensure consistency even without data of pile tip settlement.

## 4 Results

Table 5 in appendix shows the representative results of the measurements and the analysis described below.

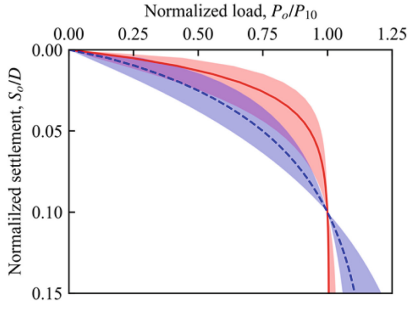
### 4.1 Load-Settlement Curve

Hyperbolic transformation curves (e.g. Chin 1972, Hirayama 1990, Fleming 1992, Dithinde et al. 2011) and Weibull distribution curves (e.g. Honjo et al. 2007) are known for fitting load-settlement curves. Though Wakita (1998) reported that the hyperbolic approximation has a better fit, Nakatani et al. (2009) reported that the Weibull distribution curve supplies the characteristic values which highly fit the yield resistance. This mathematical derivation of the yield resistance is less prone to human error than the method derived from the break point of  $\log P$ - $\log S$  (e.g. JGS 2002). Therefore, the resistance when the settlement reaches 10% of the pile diameter,  $P_{10}$ , was considered to be the smaller of both approximations for safety.

$$\frac{P_o}{P_{ou}} = 1 - e^{-\left(\frac{S_o/D}{S_{os}/D}\right)^m} \quad (1)$$

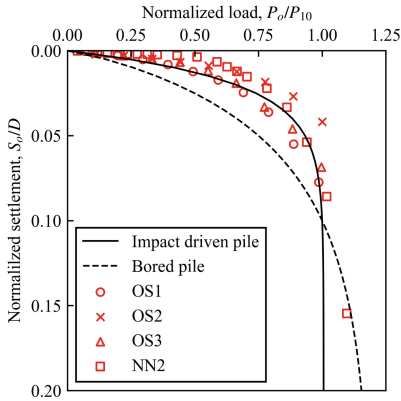
$$\frac{P_o}{P_{ou}} = \frac{S_o}{S_o + S_h} \quad (2)$$

where  $P_o$ : load at the pile head,  $P_{ou}$ : ultimate resistance,  $S_o$ : settlement at the pile head,  $S_{os}$ : the characteristic value of settlement at the pile head,  $m$ : displacement index,  $S_h$ :

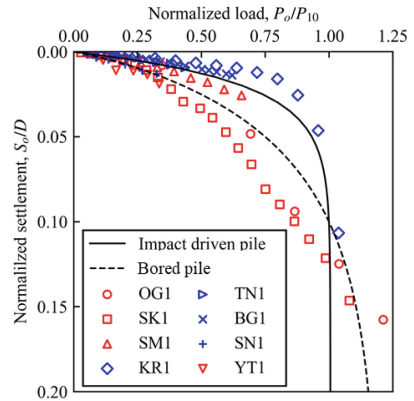


	$m$	$S_{o2}/D$
Impact driven pile	0.98	1.87%
— Averaged line		
1 $\sigma$ range: upper line	1.16	3.54%
: lower line	0.8	0.99%
Bored pile	0.87	5.11%
- - - Averaged line		
1 $\sigma$ range: upper line	1.05	8.64%
: lower line	0.69	3.02%

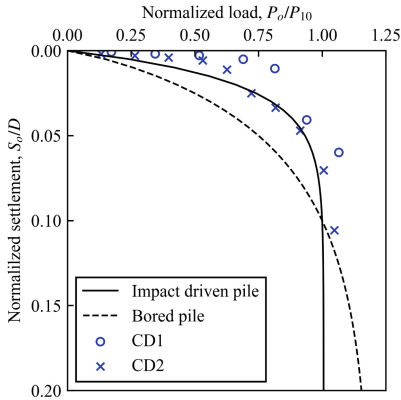
(a) Impact driven and bored pile (after Nakatani et al. 2009)



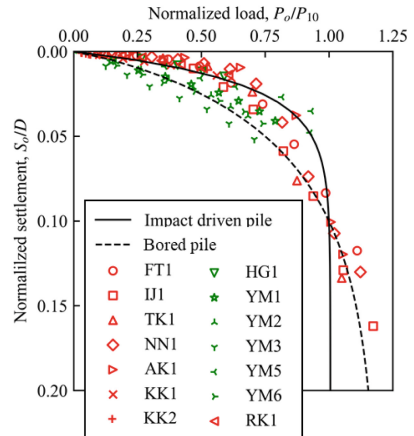
(b) Standard press-in pile



(c) WJ press-in pile (The red/blue markers represent piles without/with interlocks)



(d) Augering press-in pile (The blue markers represent piles with interlocks)



(e) Rotary press-in pile (The red/green markers represent piles embedded into soil/rock)

**Fig. 5.** Normalized load settlement curve. Impact driven and bored pile refer to Nakatani et al. (2009).

settlement when resistance reaches the half of the ultimate. Equation (1) with  $m = 1$  was the same as the proposal by Van der Veen (1953).

Figure 5 shows load-settlement curves of each assistant techniques. The load was normalized by  $P_{10}$ , and the settlement was normalized by the pile diameter,  $D$ , so the curve always went through a point in the graph (1, 0.1).

Nakatani et al. (2009) fitted each loading test to a Weibull distribution curve based on the database of loading tests, and presented the statistics of the characteristic values for each pile installation method. They reported that  $S_{os}/D$  follows a log-normal distribution and  $m$  follows a normal distribution. Figure 5a shows the average normalized load-settlement curves and one sigma range (that is, lower/upper line: both  $m$  and  $S_{os}/D$  are their means plus/minus standard deviations respectively) of the driven pile and the bored pile. Figure 5b–e also add the average lines for reference.

The load settlement curve of the standard press-in pile was in good agreement with that of the driven pile (Fig. 5b).

That of the WJ press-in pile was divided into two types: one was similar to the driven pile and the other was similar to the bored pile (Fig. 5c). The latter was joined with interlocks to the next piles during loading tests. Although Tomisawa and Katakura (1988) reported that interlocks of steel pipe sheet piles did not have a significant effect on resistance, it is natural to assume that the division was due to the interlock resistance. So, it can be inferred that the shaft resistance was lower than that of other press-in piles because shaft resistance generally gets ultimate earlier than base resistance.

Next, the curve of the augering pile resembled that of the driven pile, though the penetration procedure resembles the bored pile (Fig. 5d). This can be due to the interlocks as well as the WJ pile, and the trend curve of the augering pile itself cannot be judged here.

Finally, the curve of the rotary press-in pile embedded into soils changed shape from that of the driven pile to that of the bored pile around  $P_o/P_{10} = 0.8$  (Fig. 5e). Since the resistance was high from the initial settlement, it is expected that the effect of rotational cutting on the shaft resistance is low. Some curves of tests embedded into rocks are similar to that of the bored pile. This may because of the higher base resistance ratio due to the rocks.

## 4.2 Yield Resistance

Figure 6 shows the relationship between  $P_{10}$ , and the yield resistance,  $P_y$ , which were determined comprehensively based on the  $\log P - \log S$ ,  $S - \log t$ , and  $P - \Delta S/\Delta \log t$  curves (JGS 2002). JRA (2017) stated that  $P_y$  can be estimated to be 0.65 ( $\approx 1 - 1/e$ ) times  $P_{10}$  because it matches well with the characteristic value of the Weibull distribution,  $P_{oy}$ .  $P_y$  of the standard press-in were good agreement with the estimated line in Fig. 6. On the other hand, those of rotary cutting press-in and WJ press-in piles were about 0.7 times lower than the estimated. Though it may come from the embedded depth into the bearing layer or surging procedure, it needs further investigations. Also, it should be noted that  $P_y$  of the test results depend on the interval of the load near the yield point.

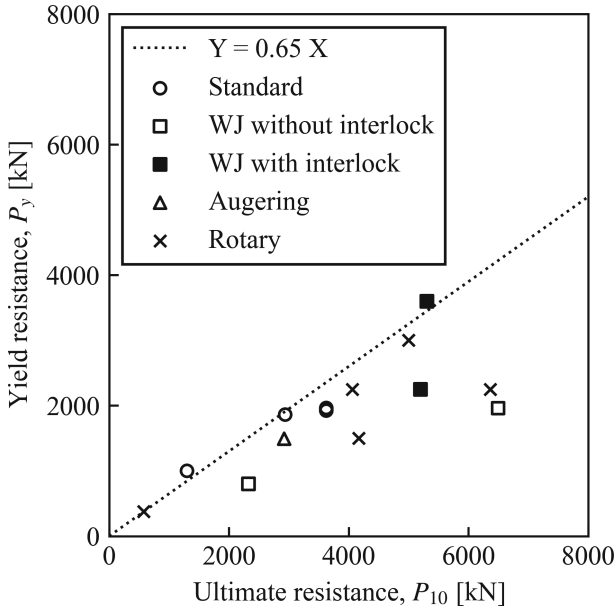


Fig. 6. Relationship between yield resistance,  $P_y$ , and ultimate resistance,  $P_{10}$

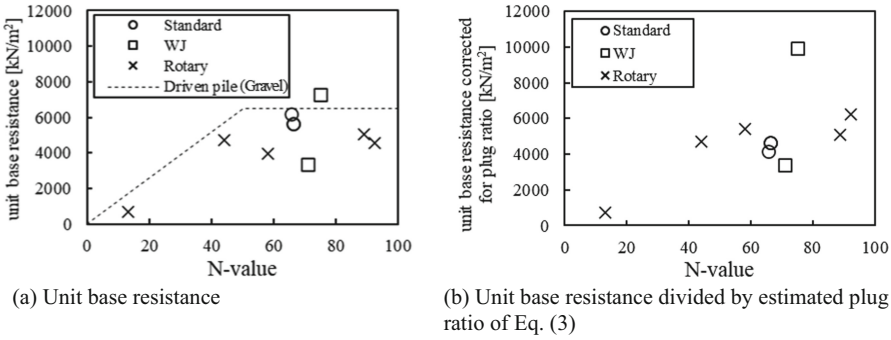
### 4.3 Base resistance

Figure 7a shows the relationship between the unit base resistance,  $q_d$ , and the average N-value of 3D downward from the pile tip.  $q_d$  was calculated from strain gages about  $1D$  above the pile tip, divided by the cross-sectional area of the pile. The evaluation formula for driven piles (JRA 2017) is also shown for comparison;  $q_d = \min(130N, 6500)$  kN/m<sup>2</sup> for gravels. Figure 7b corrected unit base resistance for plug ratio,  $\eta$ , which means the assumed ratio of the base resistance of open-end pile to that of closed-end pile. It was assumed to be in inverse proportion to the pile diameter (after Kikuchi et al. 2009);

$$\eta = (D/0.8)^{-1.4} \quad (3)$$

Also, it should be noted that this paper doesn't consider the difference of embedded depths into the bearing layer.

The base resistance of the standard press-in was about 6000 kN/m<sup>2</sup> (Fig. 7a), which was approximately the same as the value of the driven pile, 6500 kN/m<sup>2</sup>. Others of WJ and rotary press-in looked lower than that of the press-in pile. But, taking into account the plug ratio (that is size effect), base resistances of standard press-in and rotary press-in did not have any differences (Fig. 7b). That of the WJ press-in pile had a large scatter, which might come from the quality control at the end of penetration.



**Fig. 7.** Relationship between N value and ultimate unit base resistance. Driven pile refers to JRA (2017).

#### 4.4 Shaft resistance

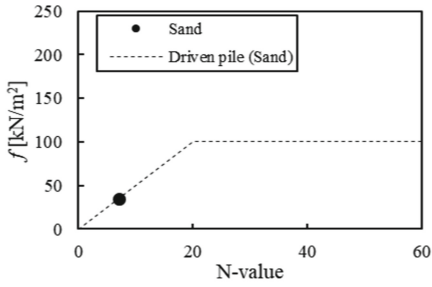
Figure 8 shows the relationship between the maximum of the unit shaft resistance,  $f$  and N values for each type of ground. The evaluation formula for driven piles (JRA 2017) is also shown for comparison;  $f = \min(5N, 100) \text{ kN/m}^2$  for cohesionless soil;  $f = \min(6N, 70) \text{ kN/m}^2$  for cohesive soil.

It cannot be said that the shaft resistance of standard press-in pile was lower than the driven pile, though only one case of sandy soil and one case of clay soil were available (Fig. 8a-1 and a-2).

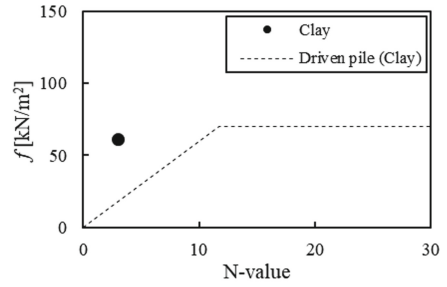
As for WJ piles, shaft resistances with interlocks were measured higher than those without interlocks (Fig. 8b-1 and b-2), the former was disregarded here. The shaft resistances in sand and silt were about 0.1–0.3 times lower than those of the driven pile, which is further lower than the previous findings of the vibratory driven piles (as shown in Table 1). This may be because the high-pressure water injection runoff the fine grains of the ground around the pile (IPA 2016). Figure 8b-3 and b-4 show the result of dynamic load tests analyzed by CAPWAP. All test piles have interlocks, and the average resistance were higher than that of the static tests.

The average shaft resistances of both cohesionless and cohesive soils of the rotary press-in pile were similar to those of driven piles (Fig. 8c-1 and c-2). Thus, particle fragmentation, which occurs especially in sandy soils during rotational cutting (IPA 2016), did not directly lead to a decrease of shaft resistance after the curing period.

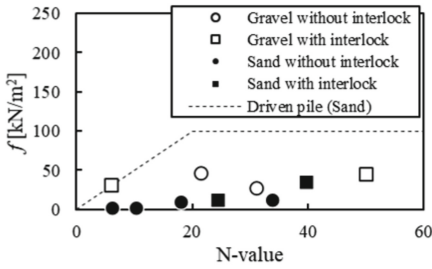




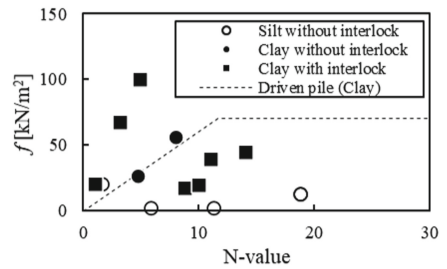
(a-1) Standard press-in pile for cohesionless soil



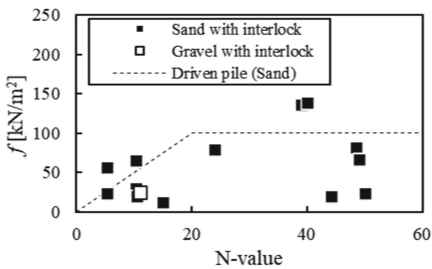
(a-2) Standard press-in pile for cohesive soil



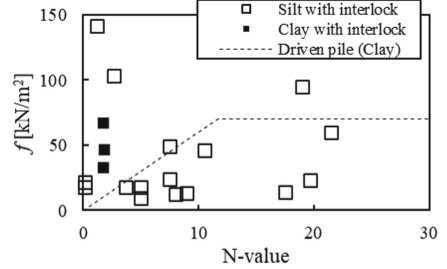
(b-1) WJ press-in pile for cohesionless soil



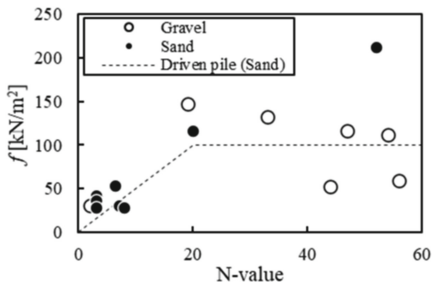
(b-2) WJ press-in pile for cohesive soil



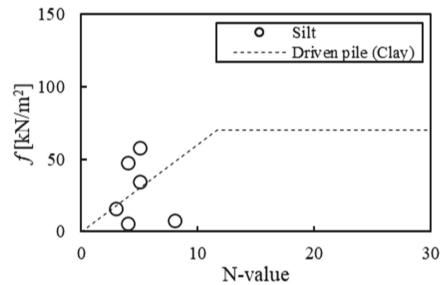
(b-3) WJ press-in pile for cohesionless soil by dynamic load test



(b-4) WJ press-in pile for cohesive soil by dynamic load test



(c-1) Rotary press-in pile for cohesionless soil



(c-2) Rotary press-in pile for cohesive soil

**Fig. 8.** Relationship between N value and maximum shaft resistance. Driven pile refers to JRA (2017).

## 5 Discussions

### 5.1 Penetration Mechanism

The above results suggest that the following mechanisms work during rotary cutting and WJ pressing, compared with standard press-in piling.

Rotary cutting has an as small impact on the surrounding ground as the driven pile. A large amount of penetration into the bearing layer is generally not required, because the piles should be penetrated without exerting a large vertical force due to the limitations of the piling machine and reaction forces. Therefore, it exhibits high rigidity before yielding, and the resistance increases gradually even after yielding.

On the other hand, WJ injection discharges fine sand and silt grains, and the shaft resistance doesn't recover even after curing periods. Therefore, the resistance tends to depend on the base resistance, and the increase in resistance to the settlement is small. Also, the base resistance varied widely because of the difference of the quality control at the end of penetration.

### 5.2 Estimation of Ultimate Resistance

Based on the results and the previous works, characteristic values for ultimate resistance were proposed in Table 3 using Eqs. 3–6.

**Table 3.** Proposed characteristic values for ultimate resistance

Piling method	Base resistance			Shaft resistance					
	Cohesionless soil		Rock	Cohesionless soil		Cohesive soil		Rock	
	$\alpha_{bs}$	$\beta_{bs}$	$\alpha_{br}$	$\alpha_{ss}$	$\beta_{ss}$	$\alpha_{sc}$	$\beta_{sc}$	$\alpha_{sr}$	$\beta_{sr}$
	–	kN/m <sup>2</sup>	–	–	kN/m <sup>2</sup>	–	kN/m <sup>2</sup>	–	kN/m <sup>2</sup>
Standard	140	5500	–	5	100	6	70	–	–
WJ	140	5500	–	1	15	2	20	–	–
Augering	–	–	0.1	2	50	4	50	–	50
Rotary	140	5500	0.6	5	50	6	50	–	100

$$Q_s = U \sum \min(\alpha_{si}N, \beta_{si})L_i \quad (4)$$

$$Q_b = \eta q_b A \quad (5)$$

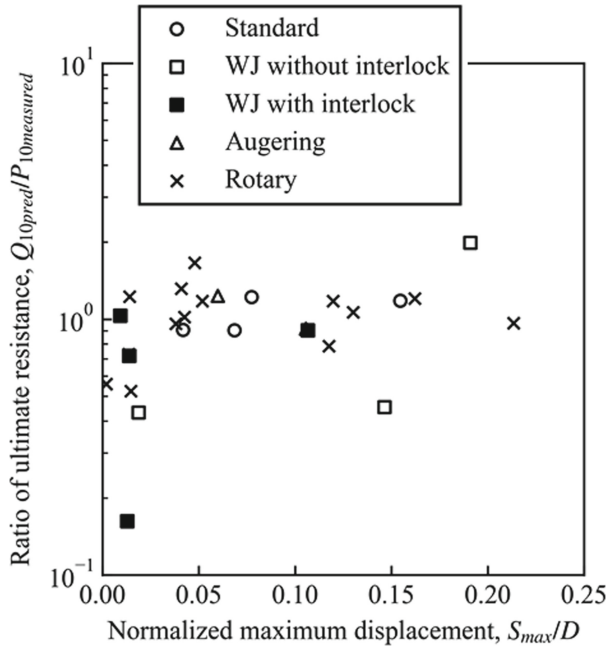
$$q_b = \begin{cases} \min(\alpha_{bs}N, \beta_{bs}) \\ \alpha_{br}(q_u, 60N) \end{cases} \quad (6)$$

where  $Q_b$  and  $Q_s$  are the base and shaft resistance; subscripts  $i$  represent cohesionless soil:  $s$ , cohesive soil:  $c$ , and rock:  $r$ , respectively;  $N$  is the converted SPT N value;  $A$  is

the base area of the pile,  $U$  is the circumference of the pile and  $L_i$  is the pile length at each soil layer. Shaft resistance at  $1D$  from the pile tip was included by base resistance, and it was excluded from shaft resistance.

The ultimate resistance of piles with interlocks was calculated by subtracting the estimated interlocking resistance,  $P_i$ , if observed during penetration (Table 4a and 4b). Otherwise, they were estimated from the maximum of those of other tests, i.e. 540 kN per interlocks. However, the ultimate resistance might be overestimated since the interlocking resistance can recover from piling to testing. Also, though characteristic values for rock depended on just a few cases and they were just for the reference, those of both augering and rotary-cutting were smaller than the previous studies, such as  $q_b = 2.5\text{--}3.0 q_u$  (e.g. AASHTO 2004, JRA 1999).

Figure 9 shows the ratio of measured ultimate resistances,  $P_{10}$  to estimated ones from N-value, the characteristic values proposed in Table 3, and Eqs. 3–6.



**Fig. 9.** Ratio of the ultimate resistance between estimated by the proposed characteristics and measured

Naturally, the larger the maximum displacement went, the lower the ratio varied. The estimated resistances were in good agreement with the measured ones, except for those of WJ press-in piles, and the proposed characteristic values in Table 3 were considered to be reasonable. The coefficients of variations (COVs) were around 0.2, which are equivalent to or lower than those of other piling methods (e.g. Nanazawa et al. 2019). It should be noted that this includes errors in the statnamic test and in the approximation of the settlement curve.

Whereas, the ratios of the WJ press-in varies widely, and the COV was about 0.8. This may be because the interlocks were joined or not, the amount of water injection differed among the test piles, and the particle size had a large effect on grain transport, which were not considered as a parameter in this study.

## 6 Summaries and Conclusions

This paper investigated loading tests to grasp the performance of the press-in pile assisted with various techniques: water-jetting, augering, and rotary cutting. The following conclusions were reached.

- The presence or absence of interlock joints could affect the load-settlement curve and shaft resistance.
- The load-settlement curves of the standard press-in pile were in good agreement with the driven pile. That of the WJ pile resembles the bored pile. Rotary press-in pile had a middle shape of those of standard press-in and WJ press-in pile.
- The ratio of the yield resistance to the ultimate one with standard press-in pile was almost the same as that of the driven pile. Whereas, those of rotary press-in and WJ press-in were about 0.7 times lower.
- The average base resistances of standard, WJ, and rotary press-in were similar if considering plug ratio or size effect, though the one of WJ varied widely.
- The shaft resistances of standard press-in and rotary press-in had little difference with that of the driven pile. That of WJ pile was about 0.1–0.3 times lower than that of the driven pile, which was further lower than the previous studies on vibratory driven piles.
- The characteristic values for the ultimate resistance were proposed, and the estimated resistance, other than WJ, coincided with the measured ones well.

The estimated resistances of the WJ press-in were highly variable. Also, we reported that the coefficient of the horizontal subgrade reaction of the WJ press-in also has a large variation (Suzuki and Kimura 2018). It is a future challenge to understand the effect of the parameters, such as the particle size and the amount of water injection, on the resistance for better construction management.

Besides, the resistance in Fig. 9 includes errors of the approximation curve. Furthermore, due to the lack of test data, we did not consider the embedded depth into the bearing layer. Further analysis including these factors will supply a better understanding.

We hope that this report will be useful as an estimation of the resistance for the assisted press-in piling. Nishioka et al. (2008) might be helpful, which proposed a method of obtaining a new bearing capacity formula for a new piling method from a few loading tests.

## 7 Appendix

**Table 4a.** Summary of axial loading tests of press-in steel pipe piles

Test Symbol	Pile		Ground at pile tip		Installation		Load test					Reference						
	Year	Dia. mm	Thickness mm	Emb. depth m	$L_b/D$	Soil type	SPT N ( $q_{tu}$ ) (MPa)	Type of press-in piling	Amount of water L/min	$P_i$ kN	$n_i$		Test type	$t_i$	$t_s$	Curing day	$Q_{max}$ kN	$d_{max}$ mm
OS1	1997	600	12/9	16.3	1.2	Gravel with silt	72	Standard	0	-	0	Static	0	1	20	2940	46	Kinoshita and Tagaya (2004) Ihara and Mizutori (2005)
OS2	1997	700	9	14.7	1.1	Gravel with silt	49	Standard	0	-	0	Static	0	0	15	3626	29	Ihara and Mizutori (2005)
OS3	1997	700	9	14.7	1.1	Gravel with silt	49	Standard	0	-	0	Static	0	0	16	3626	48	Ihara and Mizutori (2005)
NN2	2017	1000	12	8	-	Sand with silt	12	Standard	0	-	0	Static	0	0	25	1400	155	Okada and Ishihara (2020)
SK1	1999	1000	12	17.5	1.0	Gravel	75	WJ	900 × 2	-	0	Static	0	1	51	8114	146	Ihara and Mizutori (2005)
SM1	2002	800	12	14.5	3.5	Gravel	47	WJ	900 × 2	-	0	Static	0	1	20	3010	21	Kinoshita and Tagaya (2004)
KR1	2002	800	12/9	35.3	1.1	Gravel with sand	62	WJ	325 × 4	200	2	Static	2	0	37	5200	85	Omori et al. (2003) Kinoshita and Tagaya (2004)
TN1	2003	800	9	40	1.6	Sand	56	WJ	900 × 4	unk.	2	Static	2	0	unk.	2250	7	

(continued)

Table 4a. (continued)

Test Symbol	Pile		Ground at pile tip			Installation			Load test					Reference			
	Year	Dia. mm	Thickness mm	Emb. depth m	$L_p/D$	Soil type	SPT N ( $q_{tip}$ ) (MPa)	Type of press-in piling	Amount of water L/min	$P_i$ kN	$n_i$	Test type	$t_i$		Curing $t_s$	$Q_{max}$ kN	$d_{max}$ mm
OG1	2014	800	12/9	50	1.5	Sand	78	WJ	$895 \times 2 + 900 \times 2$	–	0	Static	0	16	3200	153	Dung et al. (2018)
OG2	2014	800	12/9	50	1.5	Sand	78	WJ	$895 \times 2 + 900 \times 2$	–	0	Static	0	168	8800	39	Dung et al. (2018)
BG1	2017	1000	14	44	6.0	Sandy soil	37	WJ	$900 \times 4$	unk.	2	Static	2	240	5060	14	Nuruzzaman et al. (2019)
SN1	2013	800	11/9	21.2	5.0	Sand	69	WJ	$900 \times 4$	1620	3	Static	2	unk.	7125	10	
YT1	2019	800	12/9	46.4	1.3	Sand	50	WJ	$895 \times 4$	–	0	Static	0	14	3399	15	
KY1	2014	800	15/9	36.5	3.3	Sand	50	WJ	$700 \times 4$	unk.	2	Dynamic	2	unk.	3779	1	
KY2	2014	800	19/14	25.5	–	Improved soil	(28)	WJ	$700 \times 4$	unk.	2	Dynamic	2	unk.	4089	4	
KM1	2014	800	9/14	50.7	3.1	Sand	79	WJ	$900 \times 4$	1606	3	Dynamic	2	unk.	6202	6	
KM2	2015	800	9–18	47.5	2.1	Sand	79	WJ	$900 \times 4$	790	2	Dynamic	2	unk.	6233	8	
BG2	2017	1000	14	44	6.0	Sandy soil	37	WJ	$900 \times 4$	unk.	2	Dynamic	2	30	3071	unk.	Nuruzzaman et al. (2019)
CD1	2007	914	20	12.9	8.9	Siltstone	500 (26–35)	Augering	0	unk.	2	Static	2	54	2400	55	
CD2	2007	914	20	12.3	8.9	Siltstone	500 (26–35)	Augering	0	unk.	2	Static	2	17	3100	97	

Note: unk. = unknown; First two characters in Symbol represent a test site, and tests which the same characters have were conducted in the same site.  $L_p/D$  = normalized embedded depth into bearing layer by pile diameter;  $q_u$  = uniaxial compressive strength (UCS); Amount of water is the capacity of the pump unit used if they were not measured;  $P_i$  = estimated interlock resistance during loading test from piling data during installation;  $n_i$  = number of interlocks during loading test;  $t_i$  = type of interlocks (0: no interlocks and no piles near to within 2.5  $D$ ; 1: no interlocks; 2: existence of interlocks);  $t_s$  = type of existence/absence of measurements for pile tip settlement (1: existence; 0: absence);  $Q_{max}$  = maximum resistance of loading test;  $d_{max}$  = settlement of pile head at the time  $Q_{max}$  is loaded; Test NN2 was friction piles; Since test SK1 applied the friction-reducing material to the part of the pile periphery (8.5 m), the pile head is assumed to be the point at the lower limit of the material. In test SM1, the inner soil of the steel pipe pile was excavated and filled with concrete from the pile tip to 4D after the pile was pressed in. Test OG2 was conducted after OG1 and soil improvement. Test BG1 was conducted after BG2. In test KY2, soil near pile tip was improved to 28 kPa by high-pressure jet-agitation method (JEP method)

**Table 4b.** Summary of axial loading tests of press-in steel pipe piles

Test Symbol	Year		Pile		Emb. depth		$L_p/D$	Ground at pile tip		Installation		Load test		Reference			
	Year	Year	Dia. mm	Thickness mm	Emb. depth m	Thickness mm		Soil type	SPT N ( $q_{tu}$ ) (MPa)	Type of press-in piling	Amount of water L/min	No. of bits	Test type	$t_i$	Curing day	$Q_{max}$ kN	$d_{max}$ mm
IJ1	2006		800	16	19.7	1.6	Gravel	72	Rotary	60	8	Static	1	17	5000	130	Hirata et al. (2009)
TK1	2007		800	16	17.5	0.6	Gravel	45	Rotary	18(0-6 m) 24(6-17 m)	4	Static	1	18	5250	171	Hirata et al. (2009)
FT1	2008		1000	12	15	2.2	Sand	77	Rotary	30	5	Static	1	15	6750	118	Hirata et al. (2009)
AK1	2016		800	12	4.7	-	Sand	7	Rotary	0	4	Static	0	1	605	96	Ishihara et al. (2016a)
NN1	2017		1000	12	24	1.2	Gravel with silt	59	Rotary	15	4	Static	0	1	5500	130	Okada and Ishihara (2020)
IJ2	2015		2500	25	25.5	-	-	-	Rotary	60-90	unk.	Pull-out	1	0	18287	34	Ishihara et al. (2016b)
HG1	2018		1000	10	4.7	1.4	Weathered rock	250	Rotary	150	18	Statamic	0	1	6476	15	
KK1	2009		900	10/16	11.5	0.7	Gravel with silt	236	Rotary	100	16	Statamic	1	0	1965	13	
KK2	2009		900	10	12	1.2	Gravel with silt	182	Rotary	100	16	Statamic	1	0	515	2	
YMI	2019		1000	16	12.3	2.5	Shale	1500 (47-89)	Rotary	60 x 2	16	Statamic	1	0	11417	41	Kosugi et al. (2019)

(continued)

Table 4b. (continued)

Test Symbol	Pile		Ground at pile tip			Installation			Load test				Reference			
	Year	Dia. mm	Thickness mm	Emb. depth m	$L_p/D$	Soil type	SPT N ( $q_{tip}$ ) (MPa)	Type of press-in piling	Amount of water L/min	No. of bits	Test type	$t_i$		Curing day	$Q_{max}$ kN	$d_{max}$ mm
YM2	2019	1000	16	16.3	6.5	Shale	1500 (47-89)	Rotary	60 × 2	16	Statamic	1	14	14435	38	Kosugi et al. (2019)
YM3	2019	1000	16	20.3	10.5	Shale	1500 (47-89)	Rotary	60 × 2	16	Statamic	1	14	12974	52	Kosugi et al. (2019)
YM4	2019	1500	22	12.3	1.7	Shale	1500 (47-89)	Rotary	60 × 2	24	Statamic	1	14	16636	105	Kosugi et al. (2019)
YM5	2019	1500	22	16.3	4.3	Shale	1500 (47-89)	Rotary	60 × 2	24	Statamic	1	14	14882	72	Kosugi et al. (2019)
YM6	2019	1500	22	20.3	7.0	Shale	1500 (47-89)	Rotary	60 × 2 + 30	24	Statamic	1	14	20661	64	Kosugi et al. (2019)
RK1	2020	1200	12	13	10.8	Gravel	300	Rotary	60 × 3	18	Statamic	1	14	4785	16	

Note: Test IJ1 was totally pulled out once and re-penetrated, which may decrease shaft resistance

The N value of test TK1 was estimated from the surrounding geological information as there is no borehole log under the tip of the pile

The curing period for test AK1 was only 1 day, which is extremely short compared to the standard curing period (JGS 2002). Since the bearing capacity generally increases with curing due to the set-up effect, it is considered to be an underestimate and on the safe side, and was used as-is. Test AK1 was friction piles

In test IJ2,  $Q_{max}$  includes the weight of the pipe pile and inner soils

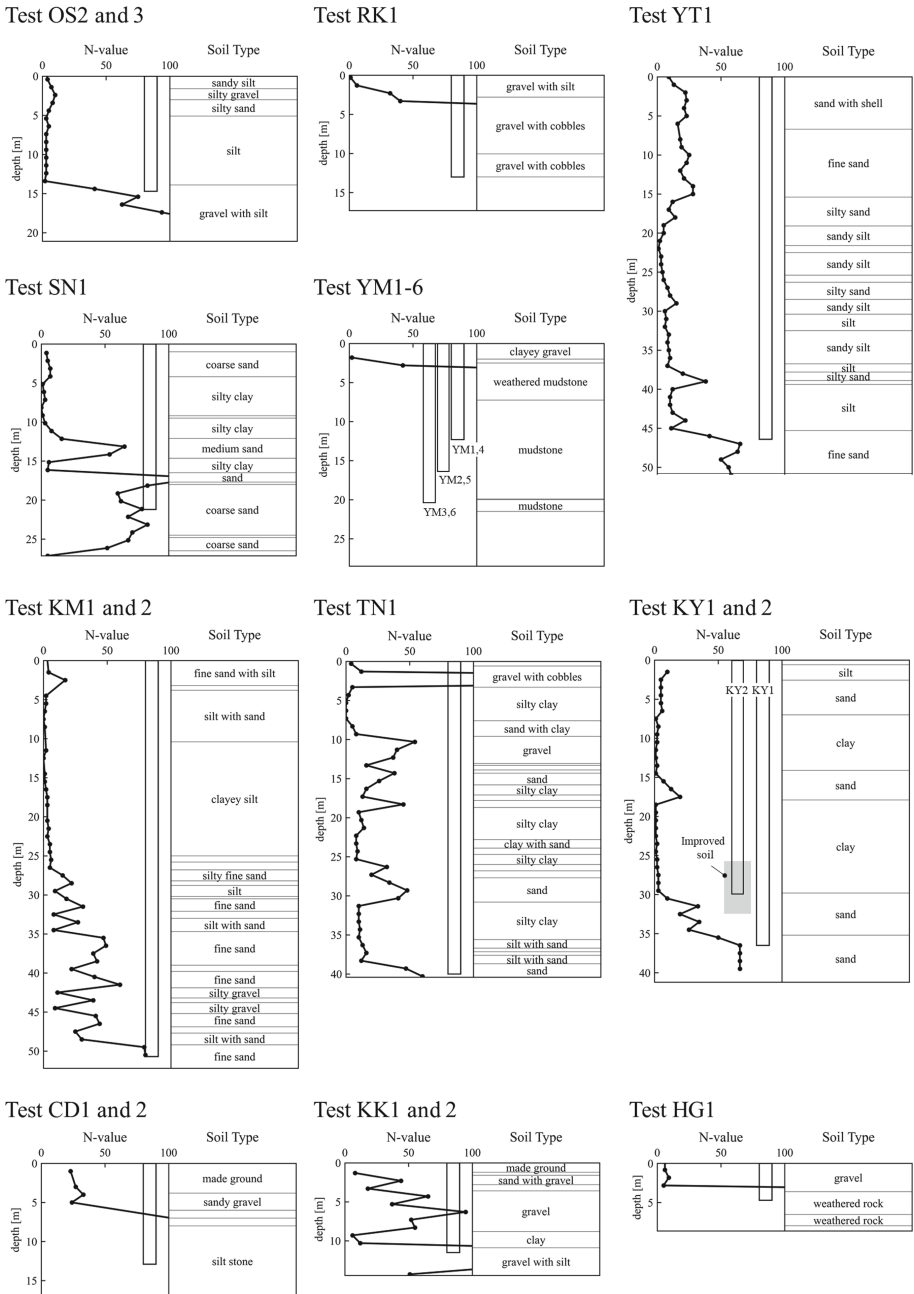
In test YM1-6, since observed bearing layer was deeper than expected, observed depth was listed on  $L_p/D$ . In test YM4, about 46 mm settlement was observed after the first drop of the weight



**Table 5.** Summary of the load tests and the analysis results of tests

Pile		Weibull distribution curve (Eq. 1)			Hyperbolic transformation curve (Eq. 2)		Estimated resistance from the curves	Ratio*
Installation	Symbol	$M$	$P_{ou}$	$S_{os}$	$P_{ou}$	$S_h$	$P_{I0}$	
		–	kN	mm	kN	mm	kN	–
Standard	OS1	0.7	3207	14.5	3462	9.7	2979	1.2
Standard	OS2	1.1	3625	8.2	4954	10.1	3624	0.9
Standard	OS3	0.7	3925	14.4	4077	8.5	3636	0.9
Standard	NN2	0.7	1337	11.8	1354	6.0	1277	1.2
WJ	SK1	–	–	–	10527	59.3	7510	0.5
WJ	KR1	1.0	5011	8.1	5815	7.1	3931	0.9
WJ	TN1	–	–	–	5942	12.4	4062	1.0
WJ	OG1	–	–	–	4395	72.3	2309	2.0
WJ	BG1	0.9	8169	14.7	11402	17.8	7069	0.7
WJ	SN1	1.0	23526	29.7	41498	51.4	20292	0.2
WJ	YT1	–	–	–	18439	65.5	10137	0.4
Augering	CD1	0.8	2158	4.5	2346	3.3	2158	1.2
Augering	CD2	0.6	3032	15.5	3044	7.7	2808	0.9
Rotary	IJ1	0.5	7068	94.2	5016	14.2	4260	1.2
Rotary	TK1	0.4	7006	91.3	4932	9.4	4285	1.0
Rotary	FT1	0.5	8376	50.6	6812	12.1	6078	0.8
Rotary	AK1	0.5	621	10.2	603	4.1	573	1.2
Rotary	NN1	0.6	5392	19.2	5314	8.5	4896	1.1
Rotary	HG1	–	–	–	12533	14.2	10974	0.5
Rotary	KK1	1.0	3509	15.3	6989	32.3	3503	1.2
Rotary	KK2	–	–	–	10867	35.0	7823	0.6
Rotary	YM1	1.2	14606	28.9	38025	92.6	14456	1.3
Rotary	YM2	1.0	22830	38.2	37090	59.7	21147	1.0
Rotary	YM3	1.2	20578	51.9	–	–	18334	1.2
Rotary	YM5	1.3	15991	28.7	25857	45.9	15986	1.7
Rotary	YM6	1.3	28489	51.5	–	–	27921	1.0
Rotary	RK1	–	–	–	8832	14.5	7882	0.7

Note: \* represents the ratio of the ultimate resistance,  $P_{I0}$  between the estimated ones based on Table 3 and the measured ones based on the load-settlement curves



**Fig. 10.** Site profiles of tests which has not been reported yet by the previous works shown in Table 4a and 4b

## References

- American Association of State Highway and Transportation Officials (AASHTO): LRFD Bridge Design Specifications, Washington, D. C. (2004)
- Nuruzzaman, A.S.M., Takashi, K., Kazunori, I.: Loading tests based on ASTM for steel pipe pile installed by Press-in piling method assisted with water-jetting. In: Proceedings of the 74th Japan Society of Civil Engineers Annual Meeting, Japan, III-12 (2019). (in Japanese)
- Aizawa, M., Matsumoto, T., Moriyasu, S., Suko, S., Kobayashi, S., Shimono, S.: Experimental study on influence of different pile installation methods on performance of pile. In: Proceedings of the First International Conference on Press-in Engineering 2018, Kochi, pp. 343–352 (2018)
- Chin, F.K.: The inverse slope as a prediction of ultimate bearing capacity of piles. In: Proceedings of the 3rd South East Asian Conference on Soil Engineering, Hong Kong, 1972, pp. 83–91 (1972)
- de Brum Passini, L., Schnaid, F., Rocha, M.M., Möller, S.V.: Mechanism of model pile installation by water jet fluidization in sand. *Ocean Eng.* **170**, 160–170 (2018)
- Dithinde, M., Phoon, K.K., De Wet, M., Retief, J.V.: Characterization of model uncertainty in the static pile design formula. *J. Geotech. Geoenviron. Eng.* **137**(1), 70–85 (2011)
- Fleming, W.G.K.: A new method for single pile settlement prediction and analysis. *Géotechnique* **42**(3), 411–425 (1992)
- GIKEN Ltd.: 50 years history of GIKEN (2016). (in Japanese)
- GIKEN Ltd.: Penetration techniques. [https://www.giken.com/en/press-in\\_method/penetration\\_tech/](https://www.giken.com/en/press-in_method/penetration_tech/). Accessed 2 Oct 2020
- Hirata, H., Suzuki, T., Matsui, T., Yasuoka, H.: Bearing capacity on rotary cutting press-in method (Gyopress Method) (Part 1). In: Proceedings of the 64th Japan Society of Civil Engineers Annual Meeting, no. III-129 (2009). (in Japanese)
- Hirayama, H.: Load-settlement analysis for bored piles using hyperbolic transfer functions. *Soils Found.* **30**(1), 55–64 (1990)
- Honjo, Y., Chung, K.L.T., Takagi, K.: Determination of vertical spring constants of a single pile based on statistical analysis of pile loading database. *J. Jpn. Soc. Civil Eng. A* **53**, 208–217 (2007)
- Ihara, S., Mizutori, T.: Bearing capacity of press-in piles. In: Proceedings of the 40th Technical Report of the Annual Meeting of the Japan Geotechnical Society, Japan, pp. 1429–1430 (2005). (in Japanese)
- International Press-in Association (IPA): Press-in Retaining Structures: A Handbook, 1st edn. IPA, Tokyo (2016)
- Ishihara, Y., Haigh, S., Bolton, M.: Estimating base resistance and N value in rotary press-in. *Soils Found.* **55**(4), 788–797 (2015)
- Ishihara, Y., Ogawa, N., Okada, K., Inomata, K., Yamane, T., Kitamura, A.: Model test and full-scale field test on vertical and horizontal resistance of hatted tubular pile. In: Third International Conference on Geotechnics for Sustainable Development, GEOTEC Hanoi 2016, pp. 131–139 (2016a)
- Ishihara, Y., Okada, K., Yokotobi, T., Kitamura, A.: Pull-out resistance of a large diameter steel tubular pile installed by rotary cutting press-in. In: Third International Conference on Geotechnics for Sustainable Development, GEOTEC Hanoi 2016 (2016b)
- Koda, M.: Change for railway pile foundations, foundations in railway structures - change of foundations for Shinkansen and improvement of productivity, no. 180, pp. 71–75 (2019). [https://www.kenkocho.co.jp/html/publication/180/180\\_pdf/180\\_18.pdf](https://www.kenkocho.co.jp/html/publication/180/180_pdf/180_18.pdf). (in Japanese)
- Japan Road Association (JRA): Design Guideline of Temporary Structures (1999). (in Japanese)
- Japan Road Association (JRA): Specifications of Highway Bridges, Part IV: Substructures (2017). (in Japanese)

- Japanese Geotechnical Society (JGS): Method for static axial compressive load test of single piles. Standards of Japanese Geotechnical Society for Vertical Load Tests of Piles (2002)
- Kikuchi, Y., Mizutani, T., Morikawa, Y.: Systematization of design verification and installation of steel pipe piles with pile loading tests. Technical Note of the Port and Airport Research Institute, no. 1202 (2009). (in Japanese)
- Kinoshita, S., Tagaya, K.: The discussion on the axial load test analysis of jacked tubular piles: especially the comparison between the single press-in method and the press-in method with water-jetting. In: Proceedings of the 2008 Japan Geotechnical Society Shikoku Branch Annual Scientific Conference, Japan (2008). (in Japanese)
- Kitamura, T., Takahashi, H., Sowa, A., Tatsumi, Y.: Loading test of pile installed vibratory hammer and discussion on the bearing performance. *Found. Eng. Equip.* **47**(8), 68–71 (2019). (in Japanese)
- Kosugi, T., Kobayashi, H., Azegami, H.: Application of rotary cutting press-in method for tubular piles into hard ground. In: Proceedings of the 54th Technical Report of the Annual Meeting of the Japan Geotechnical Society, Japan, pp. 31–32 (2019). (in Japanese)
- Dung, L.A., Fujiwara, M., Tsuchiya, M., Tejiro, S.: The countermeasure for press-in method on lengthy SPSPs and the confirmation of the bearing capacity obtained by pile loading test. In: Proceedings of the First International Conference on Press-in Engineering 2018, Kochi, pp. 65–72 (2018)
- Gillow, M., Haigh, S., Ishihara, Y., Ogawa, N., Okada, K.: Water jetting for sheet piling. In: Proceedings of the First International Conference on Press-in Engineering 2018, Kochi, pp. 335–342 (2018)
- Middendorp, P., Bermingham, P., Kaiper, B.: Statnamic load testing of foundation piles. In: Proceedings of the fourth international conference on application of stress wave theory to piles, Hague, Netherlands, pp. 581–588 (1992)
- Nakatani, S., Shirato M., Yokomaku, K.: Research on the axial deformation of a pile. Technical Note of Public Works Research Institute (PWRI), no. 4139 (2009). (in Japanese)
- Nanazawa, T., Kouno, T., Sakashita, G., Oshiro, K.: Development of partial factor design method on bearing capacity of pile foundations for Japanese Specifications for Highway Bridges. *Georisk Assess. Manage. Risk Eng. Syst. Geohazards* **13**(3), 166–175 (2019)
- Nishioka, H., Koda, M., Shinoda, M., Tateyama, M.: A calculation method of design bearing capacity of piles for several construction methods by statistical analysis of loading test data base. Railway Technical Research Institute (RTRI) report, vol. 22, no. 10, pp. 41–46 (2008). (in Japanese)
- Okada, K., Ishihara, Y.: Examples of vertical loading test of press-in pile. In: Proceedings of the 55th Technical Report of the Annual Meeting of the Japan Geotechnical Society, Japan, no. 21-9-4-01 (2020). (in Japanese)
- Omori, T., Ise, M., Kimura, Y., Takano, K.: Steel pipe sheet pile foundation work for national highway no. 30 at Kurashiki river bridges -press-in piling method assisted with water jetting and loading test. *Found. Eng. Equip.* **31**(8), 32–35 (2003). (in Japanese)
- Galindo, P.G., Davidson, C., Brown, M.J.: Installation behavior of open ended and closed ended piles with torque application. In: Proceedings of the First International Conference on Press-in Engineering 2018, Kochi, pp. 379–386 (2018)
- Paik, K., Salgado, R., Lee, J., Kim, B.: Behavior of open-and closed-ended piles driven into sands. *J. Geotech. Geoenviron. Eng.* **129**(4), 296–306 (2003)
- Paikowsky, S.G.: Load and Resistance Factor Design (LRFD) for deep foundations. National Cooperative Highway Research Program (NCHRP) Report 507. Transportation Research Board, Washington, D.C. (2004)
- Railway Technical Research Institute (RTRI): (Draft) Sheet Pile Foundation Design and Construction Manual for Railway Structures, 3rd edn. (2014). (in Japanese)

- Randolph, M.F., Leong, E.C., Houlsby, G.T.: One-dimensional analysis of soil plugs in pipe piles. *Géotechnique* **41**(4), 587–598 (1991)
- Rausche, F., Moses, F., Goble, G.: Soil resistance predictions from pile dynamics. *J. Soil Mech. Found. Div.* **98**(9) (1972)
- Shepley, P.: Water injection to assist pile jacking. Doctoral dissertation, University of Cambridge (2013)
- Society for Vibratory Hammers: Handbook on Vibro hammer Design and Construction (2015). (in Japanese)
- Suriyah, T., Kobayashi, S., Matsumoto, T.: Push-up load tests using uncrushable particles and its DEM analyses. *Geotech. Eng. J. SEAGS AGSSEA* **42**(2), 43–55 (2011)
- Suzuki, N., Kimura, Y.: Study on the horizontal bearing performance of steel tubular piles installed by the Gyropress Method and the Press-in Method assisted with water jetting. In: Proceedings of the First International Conference on Press-in Engineering 2018, Kochi, pp. 125–132 (2018)
- Suzuki, N., Kimura, Y., Sanagawa, T., Nishioka, H.: Modeling of vertical bearing capacity of rotally press-in pile used for a railway structure. In: Proceedings of the 23rd Railway Engineering Symposium, pp. 217–222 (2019). (in Japanese)
- Tomisawa, K., Katakura, K.: Report on impact test of steel pipe sheet pile foundation - bearing capacity of steel pipe sheet pile. Monthly report of Civil Engineering Research Institute, no. 422, pp. 11–23 (1988). (in Japanese)
- Tsinker, G.P.: Pile jetting. *J. Geotech. Eng.* **114**(3), 326–334 (1988)
- Van der Veen, C.: The bearing capacity of pile. In: Proceedings of the 3rd International Conference on Soil Mechanics and Foundation Engineering (ICSMFE), pp. 84–90 (1953)
- Wakita, E.: Study on standard settlement characteristic of pile. *J. Jpn. Soc. Civil Eng.* **1998**(603), 45–52 (1998). (in Japanese)
- White, D.J., Deeks, A.D.: Recent research into the behaviour of jacked foundation piles. *Adv. Deep Found.* 3–26 (2007)
- White, D.J., Sidhu, H.K., Finlay, T.C., Bolton, M.D., Nagayama, T.: Press-in piling: the influence of plugging on driveability. In: Proceedings of the 8th International Conference of the Deep Foundations Institute, New York (2000)
- Yamahara, H.: Plugging effects and bearing mechanism of steel pipe piles. *Transp. Archit. Inst. Jpn.* **96**, 28–35 (1964). (in Japanese)
- Zarrabi, M., Eslami, A.: Behavior of piles under different installation effects by physical modeling. *Int. J. Geomech.* **16**(5), 04016014 (2016)



# On Earth Dam Leak Detection Based on Using Fiber-Optic Distributed Temperature Sensor (Case Study: Canal Embankment on the Rhône River, France)

P. Abbasimaedeh<sup>1</sup>(✉), M. Tatin<sup>1</sup>, V. Lamour<sup>1</sup>, H. Vincent<sup>1</sup>, S. Bonelli<sup>2</sup>, and A. Garandet<sup>3</sup>

<sup>1</sup> Cementys, 9 rue Léon Blum, 91120 Palaiseau, France  
Pouyanabbasi@cementys.com

<sup>2</sup> INRAE, Unité de Recherche Ouvrages Hydrauliques et Hydrologie, 3275 Route de Cézanne, CS 40061, 13182 Aix-en-Provence Cedex 5, France

<sup>3</sup> Compagnie Nationale du Rhône, 2 rue André Bonin, 69316 Lyon cedex 4, France

**Abstract.** The main aim of this paper is to detect and fully evaluate the leakage potential of an embankment based on the fiber-optic distributed temperature sensing (DTS) under an R&D program in France between Cementys, INRAE and CNR (Compagnie Nationale du Rhône). The field experimental works and real data measurements have been applied for the current study. The developed measurement and monitoring system in this study which installed inside of the embankment has consisted of distributed fiber optic sensors, PT100 sensors, TDR sensors, Vibrating wire sensors, and Meteorological sensors. The solar-based energy resource has been connected to the developed measurement system and WIFI technology has been used for data transferring. The achieved result of heat measurement shows that the current study developed system is able to measure the inside embankment temperature with the perfect accuracy instantaneously. The achieved results allow us to monitor the real-time temperature difference in the main body of the embankment. Seasonal evaluation of results shows that the higher potential of leakage is occurred during winter and in the deeper parts throughout the embankment. Besides, generating an exact Equi-potential dispersion map with considerable accuracy compare with previous research and relationships has been performed. The comparison results of current study measurement and previous research on the IRFTA analytical model shows that the foundation level of the embankment has a high potential location for leakage.

**Keywords:** Embankment · Earth dam · Leakage · Distributed temperature sensing · Fiber optic · Heat transfer · Internal erosion

## 1 Introduction

Nowadays, there are different types of embankment health monitoring systems which help to increase the durability of the infrastructure such as the embankment dam within

operation time. Recent research has addressed that both physical and environmental assessments are necessary to consider the infrastructure's health monitoring and reliability (Abbasimaedeh et al. 2017). The control of infrastructure foundation's settlement, dynamic behavior, crack and damage propagation, using non-destructive tests, and corrosion and erosion measurements are suggested as the most considerable methods to health monitoring of infrastructures (Abbasimaedeh et al. 2018). The Seepage study with an emphasis on the heat measurement in hydraulic structures as a new interdisciplinary research topic for erosion potential estimating and monitoring has recently been taken into consideration for researchers (Johansson 1991; Armbruster and Merkler 1982; Armbruster et al. 1989).

There are various methods of seepage assessment such as field laboratory tests, geophysical tests, telecommunication tests, and heat transport analysis (Abbasimaedeh et al. 2020). However, the temperature data has been expressed as a feasible method, able to give real information on seepage condition. The coupled modeling are normally used to assess the seepage and thermal change in the soil media with an emphasis on the validation of temperature measurement. However, it is possible to monitor the seepage potential considering the fluid velocity, while the method is rarely used.

Several numbers of studies have been conducted on thermal and seepage transportation in the soil media from 1960 to 1980 (Stallman 1965; Birman 1968; Cartwright 1968, 1974; Sorey 1971; Domenico and Palciauskas 1973; Smith and Chapman 1983). The result of the mentioned studies indicates that heat transportation by water movement has considerable effects on the variation of temperature gradients within the earth (Bredenhoeft and Papadopulos 1965). Moreover, it is depicted that the temperature of seepage flows can play the role of natural leakage tracer which applied to the hydraulic structures (Dornstadter and Heinemann 2013). In recent decades, considerable developments have applied to the heat transportation method with the support of advanced technology in temperature measurement as well as the development of analytic approaches. In general, using temperature to estimate seepage in embankments was divided into two categories, active and passive, including analytical and numerical approaches with an emphasis on the physical parameters.

The analytical methods have highly been counseled for the localized leakage potential. The proper approach is not only able to prospect a very small leakage process but also can qualitatively specify the intensity of seepage inside the embankment (Beck et al. 2010a, b, Khan et al. 2014, 2008, Lang et al. 2008, Pyayt et al. 2013, Radzicki and Bonelli 2010b). Previous scientific assessments show that the model with physical parameters can be used to quantitatively evaluate the seepage velocity considering temperature data. The Lag-time and amplitude proposed methods by Johansson could be a considerable approach for the preliminary seepage analysis of simple geometry and saturated soil layers (Johansson 1997).

On the other hand, the numerical simulation is a strongly accurate solution in case of complicated geometry of the embankment. Numerical modeling with the proper application of boundary and initial conditions brings out the way to compute seepage velocity

in the embankment using temperature monitoring. As a model verification, the vast number of thermal-hydraulic parameters will be considered for exact computing the concurrent temperature and seepage potential in the embankment. Then the expected temperatures from numerical solutions will be compared with temperature measurements to find out the closest result from which seepage velocity (Bui et al. 1968; Bui et al. 2018, 2016; Johansson 1997; Radzicki and Bonelli 2010a, 2012, Yousefi et al. 2013; Shija and MacQuarrie 2015; Smith and Konrad 2008; Velasquez 2007).

Today, the developed thermometric methods based on the fiber optic temperature sensors are considered as the most promising method to detect the leakage area in earth dams (Artieres 2012). The distributed optical fiber allows the detection of the early signs of internal leakage and erosion all along the embankment (Johansson 1997; Perzlmaier 2007; Côté et al. 1991). This method called first time so-called “passive” method which has been developed and consists to measure the natural temperature along a horizontal optical fiber located in the saturated area (Johansson 1997, 2005). Another measurement technic is called “active” which has been developed in order to quantify locally the identified anomaly (Aufleger et al. 1998). It consists of artificially heating the soil near the optical fiber and to estimate the heat quantity carries away with the flow, which is directly correlated to the water flow rate (Artières et al. 2007; Zhou and Zhao 2018).

In this paper, the result of a filed experimental work using Cementys patented developed instruments to measure the heating transfer in the main body of the embankment using the DTS method has been recorded, analyzed, and compared with the suggested method by the previous researcher. As the case study, the measurements were performed on a real embankment located on the Rhone river in France. Cementys pieces of equipment and its high-quality QA/QC and observation methods have been used for the installation of instruments and fiber optics. The main aim of the current study is to consider the efficiency of the innovative methods and instruments of measurement to measure the internal heat transfer compare with previous approved analytical methods. The current study’s development In measurement technics will help us to monitor the real-time inside temperature everywhere of the embankment during the operation time. Furthermore, the proposed method helps to find the exact value and location of the leakage potential in the main body of the embankment. Finally, the lower cost range of the maintenance, choosing the best method to control the leakage, higher range of safety factor, and real-time health monitoring with an emphasis on erosion and leakage damages in embankment structures will be achieved using the current paper method.

## 2 Materials and Methods

### Conceptual Methods and Assumption

To measure the leakage potential and erosion steps in the main body of the embankment the heat transport evaluation with an emphasis on the collaborated real scale field experimental work has been performed with Cementys and CNR on the embankment located on the Rhône river. The heat transport in the body of the hydraulic structures is described by an energy relationship (Eq. 1) in the literature. The second and the third terms of this equation correlated the conductive and advective heat transport processes respectively, where the advective process is defined as the transport of heat with the



mass of flowing water. In this relation  $T$  is the temperature ( $^{\circ}\text{C}$ ),  $C$  is the volumetric heat capacity of the porous domain,  $C_f$  is the volumetric heat capacity of water and  $\lambda$  is the thermal conductivity of the porous domain (Radzicki and Bonelli 2012).

$$C \frac{\partial T}{\partial t} - \lambda \frac{\delta T}{\delta x^2} - v C_f \frac{\partial T}{\partial x^2} = 0 \quad (1)$$

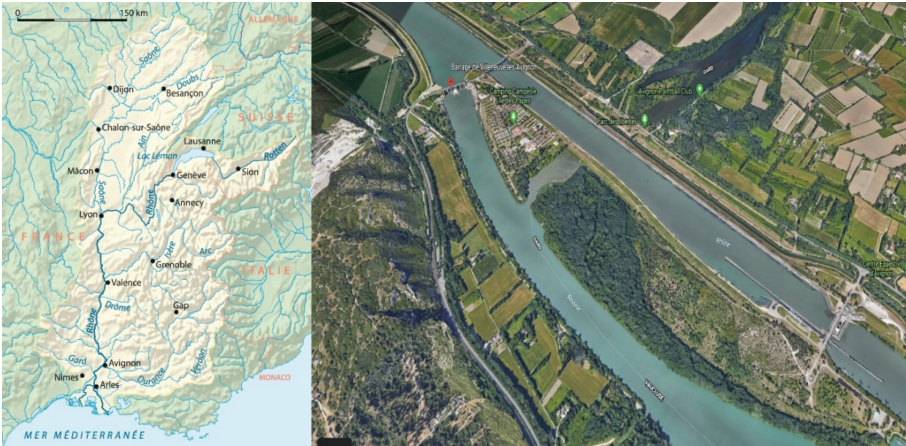
The major dependencies were described by the energy conservation equation. Considering the zero water flow velocity, there is only heat conduction, which is a relatively slow process. However, even a change in the moisture content of the soil medium is able for the significantly affect local thermal front velocities. While the fluid motion (seepage, leakage), heat is also allowed to transport along with the water mass. This process is called advection and generates a much more substantial heat flow which is faster the fluid flow. In addition, to get an exact expression of temperature loadings on boundary conditions (reservoir, air temperature), temperature sensors are often required to be set up in damming structure (Radzicki and Bonelli 2012).

Temperatures of the air and the water in the reservoir are the principal thermal loadings for the dam. In addition, It is assumed that other heat sources like geothermal and frozen processes, radiation, and wind influence are neglected. In the case of the null water velocity, there is only conductive, slow heat transport from the dam surfaces inward the dam. Hence with rising the water velocity, the temperature from the reservoir is moved quicker with the mass of water which results in the temperature field perturbation. Similarly, there are significant temperature differences in the embankment body, especially between the high and low potential of seepage. Finally, an analysis of the temperature distribution in the dam's body allows for leakage identification. Such temperature measurements can be realized with the fiber optic cable at every meter of the embankment's length. This technology called distributed temperature sensing (DTS) gives a possibility of continuous monitoring of the structure in space.

### Case Study

Within the scope of an R&D program in the collaboration with Cementys (an international science-based company to monitor, implement, examine, and optimize the maintenance of various projects, infrastructures, constructions) and CNR (Compagnie Nationale du Rhône) aiming to produce tools and monitoring methods for the leak detection inside the earth dams, a sensitive section of an embankment has been instrumented with optical fibers to complete the old configuration in the place monitoring system.

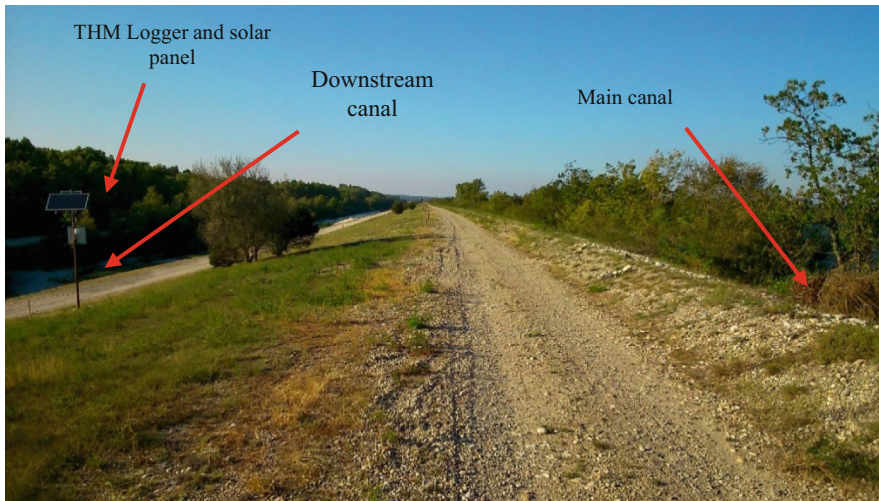
The structure instrumented is a canal embankment of a hydroelectric scheme owned by the CNR on the Rhone river in France (Fig. 1). Rhone has about 812 (km) length which expanded between Switzerland and France. In terms of flow, of all the rivers flowing in the Mediterranean, the Rhône is second after the Nile, if one does not take into account the Black Sea, where the Danube and the Don flow in particular.



**Fig. 1.** The geological map of the Rhone river (left) and the aerial photo of embankment location (right).

### Instrument Installation

An overview of the current study’s DTS system is shown in Fig. 2. The new monitoring installed the system on the embankment is consisted of a THMLoggerData Logger, and a SensoLogger optical fiber interrogator. The main energy for the measurement system has been supported by the solar-powered (Fig. 3). Furthermore, the system is continuously connected to the web-based THM Insight® software, providing a real-time display of the data in the control center.



**Fig. 2.** Canal embankment of a hydroelectric scheme owned by the CNR (Compagnie Nationale du Rhône) over the Rhone river with installed instruments for heat measurement.

The monitoring and measurement system used in the current study includes the following instruments:

- Distributed fiber optic which has been supported by the following sensors:

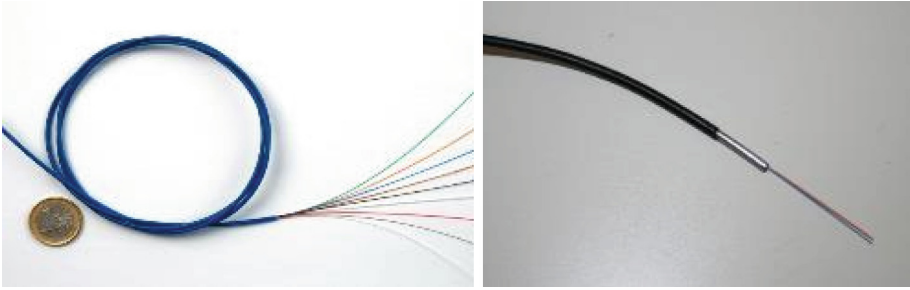
- SensoLux Detect®: Distributed temperature sensors (Raman backscatter) with Sixteen numbers of 12 m depth thermometric tubes are installed in the leakage potential area. However, two sensors with similar lengths have been installed in safe and lower leakage potential areas of the embankment. All these tubes instrumented with a SensoLux Detect optical fiber cable. The achieved data by mentioned optical fiber are able to become a database to produce the 2D dispersion map of the temperature in the leakage potential areas. Furthermore, in order to localize the leakage areas with the longitudinal profile of the temperature, another optical fiber cable has been installed in the 50 cm depth of the soil in the downstream toe.

- SensoLux TM®: Distributed strain measurement (Brillouin backscatter) at the top of the embankment to observe the settlement of the ground (Fig. 4).



**Fig. 3.** THM logger on the downside of the embankment (left) solar system and metrological sensor (right)

- PT100 sensors: temperature measurement in the thermometric tubes in order to correct and calibrate the optical fiber measurements.
- TDR sensors: water content measurement in the soil around the leakage area to control the leakage evolution.
- Vibrating wire interstitial pressure cells water level measurements in order to feed the statistical analysis.



**Fig. 4.** SensoLux TM cables (left) and SensoLux Detect (right)

- Meteorological sensors: environmental parameters measurements (atmospheric pressure, air temperature wind speed, humidity, rainfall) in order to the feed the statistical analysis (Fig. 5).



**Fig. 5.** PT100 sensors, TDR sensors, Vibrating wire sensors and Meteorological sensors (left to right)

Temperature measurements have been performed continuously without heating the soil “passive method”. During punctual campaigns (twice a year), the soil was heated around the fiber “active method” in the downstream toe. This measurement helps us to better identification of the leakage area considering the increase of the thermal contrast between areas in which only the conduction phenomenon occurs and areas in which both conduction and advection phenomena occur. Moreover, the mentioned measurement will enable us to highlight the evolution of the flow rate, without giving it a precise value. The fiber optic and THM Logger installation location on the embankment have been depicted in the Fig. 6. It is depicted that the reference tubes are located in both side of the embankment which has a lower potential of the leakage while to aim of a perfect measurement other tubes are considered on the middle part of the embankment with the higher range of leakage potential.

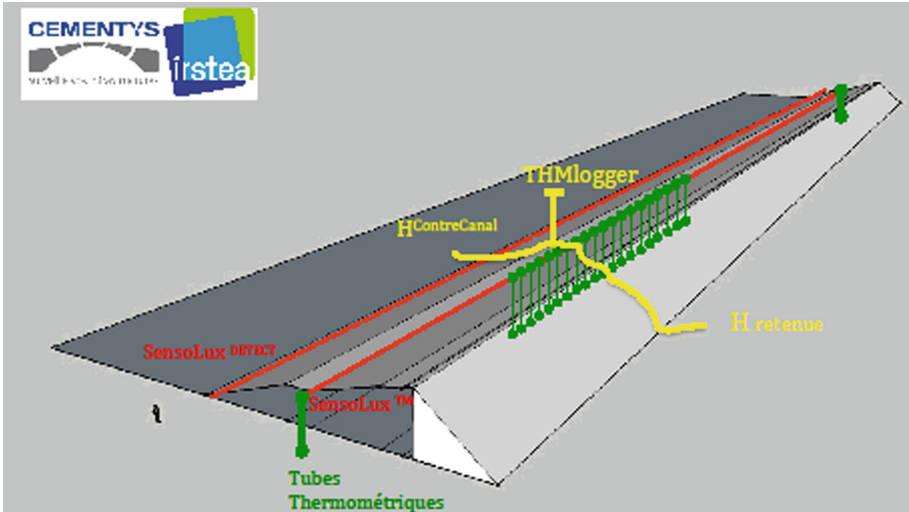


Fig. 6. Schematic of sensors implantation throughout the embankment

### 3 Results and Discussion

After installation of all optical fibers and connecting to the available old measurement instruments, the system been fully checked under a professional QA/QC program by Cementys professional, and then all the equipment and sensors were fully calibrated by some sample tests. The achieved data relating to the temperature profile in vertical pipes are illustrated in Fig. 7. The result shows that the average air temperature during winter (January) has been detected approximately 5 °C while the average soil temperature at depth in the foundation observed approximately 13 °C (left side). Within the summer (July) the average air temperature is detected around 25 °C and the mean of the soil temperature at depth in the foundation was measured around 11 °C (right side). In a deep and accurate assessment, it is observed that the weather's temperature has a significant effect on the soil temperature up to 3 m in depth (zone A). The small seepage flow has no remarkable effect on the seasonal temperature variation in the embankment and is constant to approximately 3 m depth.

The exact penetration depth is related to soil mechanical and chemical properties. The achieved result shows that the temperature profile will be changed in accordance with the effect of the rate of heat transportation and the concentrated seepage flow. In this case, the temperature profile is no longer constant in-depth. A good example is zone C which indicates the leakage area of the embankment. This is illustrated in Fig. 8 where the seepage flow in the foundation has been detected (depth greater than 10 m, Zone C). This Figure illustrates the leakage detection between first to mid of the March (every 2 h). Furthermore, the heat transported has a considerable correspondence to the water temperature of the reservoir in previous weeks before the current measurement.

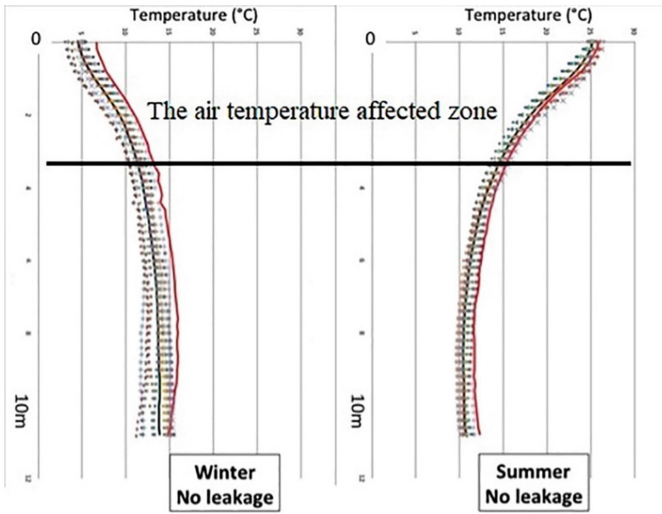


Fig. 7. Vertical temperature measurement in vertical borehole (pipes) during summer and winter

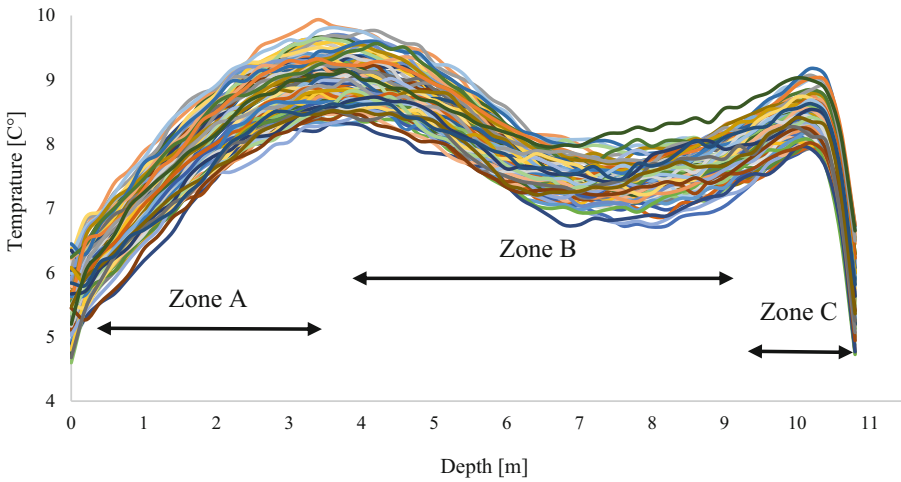
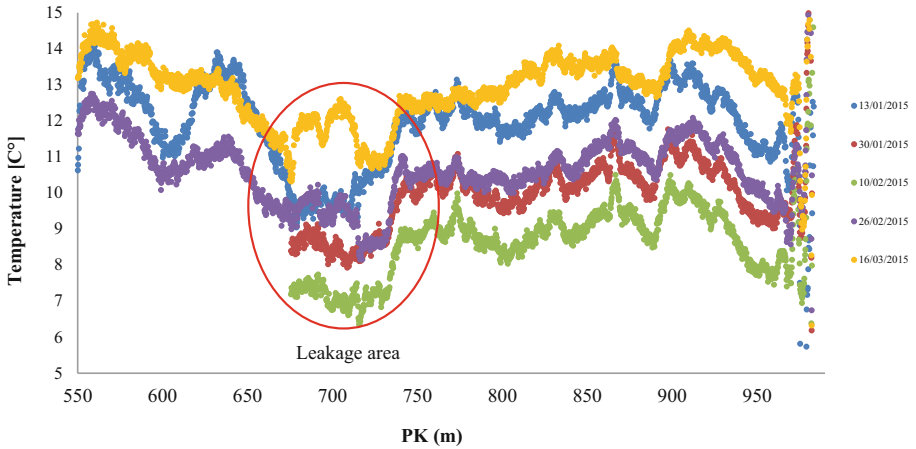


Fig. 8. Vertical temperature measurement in vertical pipes of leakage potential area

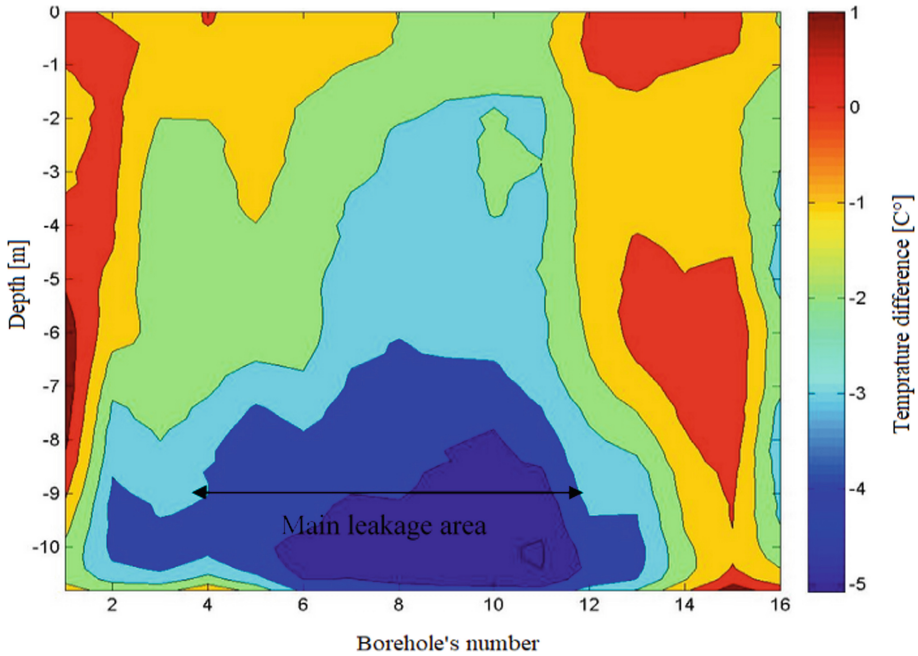
A three-month length of temperature variation record between January and February 2015 on the downstream toe of the embankment as the sample is depicted in Fig. 9. Total 2 years temperature record has been performed in this study. All the temperature values have been recorded with an emphasis on the depth, length, and exact time of detection.

The mentioned data can generate a strong database of heat transportation differences and enough useful to accurately estimate the seasonal leakage potential in the embankment. Such fiber optics' data have been used to produce the accurate dispersion real-time map of leakage and interior temperature of the embankment. Results of such measurement show that there is a leakage area in the length of 650 to 750 m of fiber optic.



**Fig. 9.** Horizontal temperature measurement throughout the embankment in the foundation level

Based on the achieved data and performing an accurate statistical analysis the innovated leakage monitoring system has been developed in the scheme of a live 2D Equi-potential (Equivalent dispersion) dispersion map of the temperature inside the embankment to estimate the leakage potential. The developed Equi-potential dispersion map represents the difference between the temperature profiles in the tubes in the leakage area and the temperature profiles of the two available reference tubes located far away from the leakage area. Hence, the obtained contrasts enable to detect the leakage area, which is colder in-depth than the available tubes. As an example, a framed photo of the Equi-potential dispersion map which has been obtained in winter is illustrated. The result shows that the water temperature is significantly colder than the soil at this depth. This 2D Equi-potential dispersion map enables to display in real-time on the web application THM Insight (Fig. 10).



**Fig. 10.** Equi-potential dispersion map of the difference between the temperature profiles in the tubes and the reference temperature profiles.

To make validation in the comparison with the results of previous methods, the IRFTA model for velocity analysis (Radzicki and Bonelli 2010, 2012) on the current study's data was performed. The mentioned method is an application to the thermal phenomena of the original IRFA model (Bonelli 2009). The model is based on the influence of air temperature and water temperature on the measured temperature in the embankment and its foundation. Furthermore, the method allows us to quantify the delay time, the thermal diffusivity of the soil, and the Peclet number, which is the ratio of the quantity of heat transported by the water and the quantity of diffusion heat. After that, the method allows us to estimate the magnitude of the water velocity, which is illustrated in Fig. 11 during leakage potential. Results show that the higher range of water velocity has been detected in the deeper part of the embankment. Furthermore, it shows the current work have an acceptable ability to accurate leakage location.



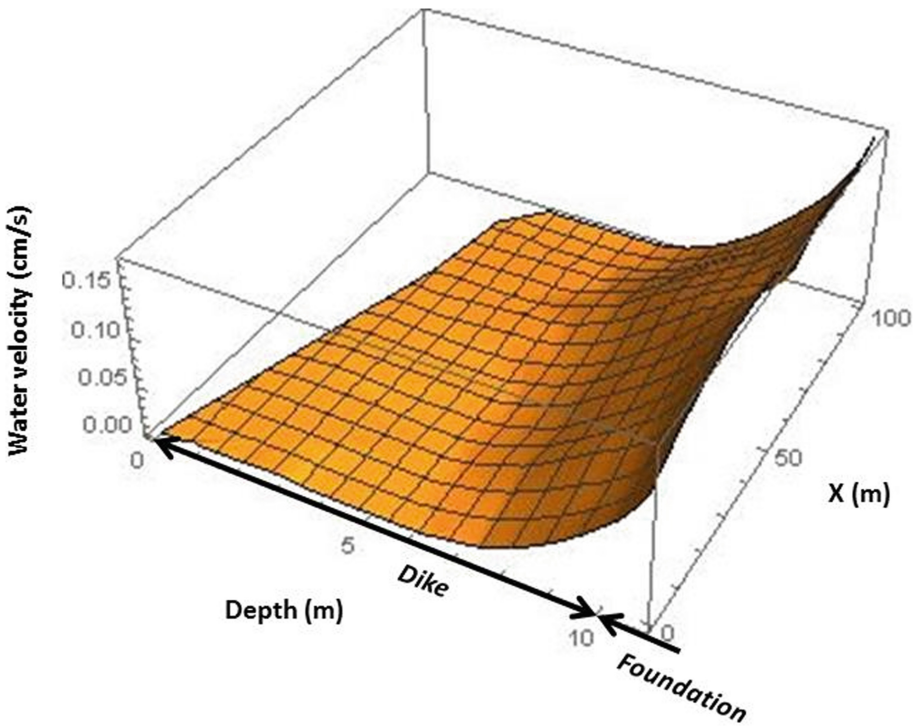


Fig. 11. The water velocity values based on the IRFTA model.

## 4 Conclusions

This paper introduced a developed practical method to measure and estimate the leakage potential using a real-time monitoring system based on the distributed temperature sensor (DTS). The health monitoring system is installed in a sensitive leakage area (internal erosion) of an embankment located on the Rhone river in France. The specificity of the proposed system is that the optical fibers were installed both vertically and horizontally in the main body of the embankment and downstream toe. The measured temperature received by the vertical measurement using fiber optics in eighteen tubes distributed along the embankment is the main database for future analysis in this system. The proposed pattern allowed us to plot a two-dimensional Equi-potential dispersion map of the dam temperature which is displayed in real-time on a web interface. Achieved results show that the current paper's developed method to measure the inside heat transportation of the embankments has enough accuracy in a comparison with previous research and analytical methods. Besides, the proposed measurement technology can estimate the exact leakage potential location as a live dispersion map in the embankment during operation time. Considering the advantages of our real-time monitoring system which addressed in the introduction part, the owner selected the economic method (diaphragm wall) to control the seepage and leakage in the embankment which considerably had the

optimum cost for its organization and was successful to fully control the leakage and eventually inside erosion.


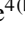
## References

- Abbasimaedeh, P., Nasrabadi, T., Wu, W., Al Dianty, M.: Evaluation of oil pollution dispersion in an unsaturated sandy soil environment. *Pollution* **3**(4), 701–711 (2017)
- Abbasimaedeh, P., Wu, W., Da Fonseca, A.V., Ghaffari Idrmousa, K., Sudan Acharya, M., Bodaghi, E.: A new approach to estimate the factor of safety for rooted slopes with an emphasis on the soil property, geometry and vegetated coverage. *Adv. Comput. Des.* **3**(3), 233–253 (2018)
- Armbruster, H., Blinde, A., Brauns, J., Doscher, H., Hotzl, H., Merkle, G.: The application of geoelectrical and thermal measurements to locate dam leakage. *Detect. Subsurf. Flow Phenom.* **27**, 31–47 (1989)
- Armbruster, H., Merkle, G.: Measurement of subsoil flow phenomena by thermic and geoelectric methods. *Bull. Int. Assoc. Eng. Geol.* **26**, 135–142 (1982)
- Artieres, A.: Systemes d'auscultation de digues basées sur des mesures de température et des déformations par fibre optique. *Auscultation des barrages et des Digués - Pratiques et perspectives*, p. 16 (2012)
- Artières, O., et al.: Active and passive defences against internal erosion. In: *Assessment of the Risk of Internal Erosion of Water Retaining Structures: Dams, Dykes and Levees*. Intermediate report of the European working group of ICOLD, pp. 235–244. TUM, Technische Universität München (2007)
- Aufleger, M., Dornstädter, J., Fabritius, A., Strobl, T.: Fiber optic temperature measurements for leakage detection – applications in the reconstruction of dams. In: 66th ICOLD annual meeting, International Commission on Large Dams (1998)
- Aufleger, M., Strobl, T., Dornstädter, J.: Fiber optic temperature measurements in dam monitoring. In: 20th International Congress on Large dams, Beijing (2000)
- Beck, Y.L., Cunat, P., Guidoux, C., Aarteies, O., Mars, J., Fry, J.J.: Thermal monitoring of embankment dams by fiber optics. In: 8th ICOLD European Club Dam Symposium, Austria, pp. 461–465 (2010a)
- Beck, Y.L., et al.: Thermal monitoring of embankment dams by fiber optics. In: 8th ICILD European Club symposium, pp. 444–448 (2010b)
- Boufadel, M.C., Venosa, A.D., Suidan, M.T., Bowers, M.T.: Steady seepage in trenches and dams: effect of capillary flow. *J. Hydraul. Eng.* **125**, 286–294 (1999)
- Bonelli, S.: Approximate solution to the diffusion equation and its application to seepage-related problems. *Appl. Math. Model.* **33**(1), 110–126 (2009)
- Bredhoeft, J.D., Papadopoulos, I.S.: Rates of vertical groundwater movement estimated from the Earth's thermal profile. *Water Resour. Res.* **1**(2), 325–328 (1965)
- Bui, Q.C., Zhou, Y., Zhao, C.: The capacity of active heat method in evaluation of seepage. *Heat Transf. Asian Res.* **47**, 150–164 (2018)
- Bui, Q.C., Zhou, Y., Zhao, C.: Seepage evaluation in embankment dam based on short-term temperature observation and heat injection. *Electron. J. Geotech. Eng.* **21**, 10493–10506 (2016)
- Cartwright, K.: Thermal prospecting for ground water. *Water Resour. Res.* **4**, 395–401 (1968)
- Cartwright, K.: Tracing shallow groundwater systems by soil temperature. *Water Resour. Res.* **10**(847), 855 (1974)
- Côté, A., Carrier, B., Leduc, J., Gervais, R.: Water leakage detection using optical fiber at the peribonka dam. In: *Seventh International Symposium on Field Measurements in Geomechanics*, Boston (2007)

- Domenico, P.A., Palciauskas, V.V.: Theoretical analysis of forced convective heat transfer in regional ground-water flow. *Geol. Soc. Am. Bull.* **84**, 3803–3814 (1973)
- Dornstadter, J., Heinemann, B.: Temperature as tracer for in-situ detection of internal erosion. In: *Proceedings ICSE-6, Paris*, pp. 1369–1375 (2013)
- Johansson, S.: Seepage monitoring in embankment dams. PhD Thesis, KTH (1997)
- Johansson, S.: Localization and quantification of water leakage in ageing embankment dams by regular temperature measurements. In: *17th International Congress on Large Dam*, pp. 991–1005 (1991)
- Khan, A.A., Vrabie, V., Beck, Y.L., Mars, I.J., D'Urso, G.: Monitoring and early detection of internal erosion: distributed sensing and processing *Structural. Health Monit.* **13**, 562–576 (2014)
- Khan, A.A., Vrabie, V., Mars, J.I., Girard, A., D'Urso, G.: A source separation technique for processing of thermometric data from fiber-optic DTS for measurements water leakage identification in dikes. *IEEE Sens. J.* **8**(7), 1118–1129 (2008)
- Lang, B., et al.: Neural clouds for monitoring of complex systems. *Opt. Mem. Neural Netw.* **17**, 183–192 (2008)
- Perzmaier, S.: Verteilte Filtergeschwindigkeitsmessung in Staudämmen. PhD Thesis, TU München (2007)
- Pyayt, A.L., Kozyonov, A.P., Mokhov, I.I., Lang, B., Krzhizhanovskaya, V.V., Slood, P.M.A.: An approach for realtime levee health monitoring using signal processing methods. *Procedia Comput. Sci.* **18**, 2357–2366 (2013)
- Radzicki, K., Bonelli, S.: Determination of seepage location and its intensity by application of IRFA model to fiber optics temperature measurements analysis. *Tech. J. Cracow Univ. Technol.* **107**(16), 55–62 (2010)
- Radzicki, K., Bonelli, S.: Thermal seepage monitoring in the earth dams with impulse response function analysis model. In: *8th ICOLD European Club Symposium*, pp. 22–23 (2010)
- Radzicki, K., Bonelli, S.: A possibility to identify piping erosion in earth hydraulic works using thermal monitoring. In: *8th ICOLD European Club Symposium*, pp. 618–623, 22–25 September 2010
- Radzicki, K., Bonelli, S.: Monitoring of the suffusion process development using thermal analysis performed with IRFTA model. In: *6th ICSE*, pp. 593–600 (2012)
- Radzicki, K., Bonelli, S.: Physical and parametric monitoring of leakages in earth dams using analysis of fiber optic distributed temperature measurements with IRFTA model. In: *24th International Congress on Large Dam, Kyoto* (2012)
- Shija, N.P., MacQuarrie, K.T.B.: Numerical simulation of active heat injection and anomalous seepage near an earth dam-concrete interface. *Int. J. Geomech.* **15**, 04014084 (2015)
- Smith, L., Chapman, D.S.: On the thermal effects of groundwater flow: 1 regional scale systems. *J. Geophys. Res.* **88**, 593–608 (1983)
- Smith, M., Konrad, J.M.: Analysis of the annual thermal response of an earth dam for the assessment of the hydraulic conductivity of its compacted till core. *Can. Geotech. J.* **45**, 185–195 (2008)
- Sorey, M.: Measurement of vertical groundwater velocity from temperature profiles in wells. *Water Resour. Res.* **7**, 963–970 (1971)
- Stallman, R.W.: Steady one-dimensional fluid flow in a semi-infinite porous medium with sinusoidal surface temperature. *J. Geophys. Res.* **70**, 2821–2827 (1965)
- Velasquez, J.P.P.: Further development of the gradient method for leakage detection and localization in earthen structures. Technical University of Munich, Munich (2007)
- Yousefi, A.N.S., Ghaemian, M., Kharaghani, S.: Seepage investigation of embankment dams using numerical modelling of temperature field. *Indian J. Sci. Technol.* **6**, 5078–5082 (2013)
- Zhou, Y., Zhao, C.: The capacity of active heat method in evaluation of seepage. *Heat Transf. Asian Res.* **47**, 150–164 (2018)



# Comparative Evaluation of Morphometric Parameters on Runoff Estimation of Savitri Watershed, India

Sudarshan Bobade<sup>1</sup>, Arun Dhawale<sup>2</sup>, Vaibhav Garg<sup>3</sup>, Anand Tapase<sup>4</sup>  , Digvijay Kadam<sup>4</sup>, and N. K. Patil<sup>4</sup>

<sup>1</sup> TSSM's BSCOER, PCET's PCCOER, Pune, India

<sup>2</sup> Department of Civil Engineering, Imperial College of Engineering and Research, Pune, Maharashtra, India

<sup>3</sup> Water Resource Department, Indian Institute of Remote Sensing (ISRO), Dehradun, India  
vaibhav@iirs.gov.in

<sup>4</sup> Rayat Shikshan Sanstha's, Karmaveer Bhaurao Patil College of Engineering, Satara, India  
{digvijay.kadam,nagendra.patil}@kbpcoes.edu.in

**Abstract.** A Morphometric assessment has emerged as an effective tool to recognize and analyze the neotectonic signatures governing a particular drainage basin. Studies on Morphometric properties involving the linear, areal and relief aspects are vital as it aids in evaluating the hydrological response and prioritization of watersheds. This would further help in understanding the simulation of the rainfall-runoff process as it forms an inherent component of the hydrological environment at the watershed scale. The present research attempts to investigate and compare the morphometric parameters of the Savitri watershed considering two datasets (toposheet and DEM) over two time periods. The Savitri is designated as a seventh-order basin with a dendritic pattern covering a total area of 1966.34 km<sup>2</sup>. Additionally, after the enumeration of the parameters, the runoff estimation is determined using the Natural Resources Conservation Service-Curve Number (NRCS-CN) method that incorporates soil types, land use, and land cover, slope, rainfall of the region along with antecedent moisture conditions. The scatter plot computed between rainfall and runoff signifies that the correlation coefficient ( $r$ ) is 1 representing a perfectly positive correlation between the two variables. Thus, the results reveal that the runoff of the region has been substantially reduced from high to moderate flow accompanied by a decrease in rainfall amount from 1990 to 2020.

**Keywords:** Morphometric analysis · NRCS-CN · Runoff Estimation

## 1 Introduction

Being an integral part of the fluvial landscape, watersheds form geohydrological units draining to a common point by a system of streams (Sakthivel et al. 2019). To understand the underlying structural components, hydrological and geomorphological features, (Mahala 2020) it is necessary to investigate and quantify the Morphometric properties of each drainage basin. Morphometric analysis refers to the quantitative or numerical measurement of landforms (Clarke 1966) in respect to linear, areal, and relief aspects of any basin that aids in assessing the hydrologic response (Abdulkareem et al. 2018) and prioritization of watersheds. With time, owing to both natural and human-induced factors, watersheds across the globe are facing rapid deterioration in terms of water quality and aquatic ecosystems (Agidew and Singh 2018) that needs to be addressed.

The quantitative assessment provides insight upon the form and processes governing a drainage basin and its related information is vital (Prabhakaran and Raj 2018) for sustainable planning and managing the existing resources available within a watershed. Initially, the Morphometric study propounded by Horton (1932, 1945) and later on many scholars such as Stahler (1952, 1964) further carried forward the works (Asfaw and Workineh 2019). Furthermore, geomorphological investigation reflects the hydrological characteristics which are vital to understand the simulation of the rainfall-runoff process and also to predict any flood peaks in the future (Abdulkareem et al. 2018). This rainfall-runoff response constitutes an extremely complex event (Pathare and Pathare. 2020) forming intrinsic components of the hydrological environment at the watershed scale.

Rainfall and runoff comprise the major sources of water for replenishing groundwater in a particular watershed. The magnitude and rate of runoff are influenced by geomorphological variables, especially the land-use dynamics, soil, precipitation data, etc. (Kumar et. al. 2017). To estimate and predict the runoff volume for a given rainfall event, the most widely used method developed by the United States Department of Agriculture (USDA) is Natural Resource Conservation Service Curve Number (NRCS-CN) model (Rao 2020, Soulis and Valiantzas 2012, Saravanan and Manjula 2015).

With the advent of geospatial tools involving Remote Sensing (RS) and Geographical Information System (GIS), computation of various morphological and hydrological parameters has become convenient and time-effective. The evaluation of various Morphometric variables and runoff estimation of the present research has been assessed and processed in a GIS environment (Agidew and Singh 2018, Pathare and Pathare 2020, Agarwal et al. 2013). The work also involves a comparative analysis of Morphometric variables extracted from the Survey of India (SoI) topographical sheet (1:50,000) for the year 1967 and AlosPalsar DEM (30 m) for 2020 to examine the changes developed over the Spatio-temporal dimension in the study area. In contrast, for the assessment of runoff, the NRCS-CN model is integrated with geospatial tools wherein the Curve Number (CN) parameter values are selected from the NRCS standard table (Soulis and Valiantzas 2012, Amutha and Porchelvan 2009). Keeping this view in the backdrop, the present study aims to perform the Morphometric parameters and runoff estimation using geospatial tools to assess the hydrological behavior sustaining in the Savitri watershed.

## 2 Study Area

Administratively, the study area as shown in Fig. 1 is situated in the Raigad District of Maharashtra State. The district is spread over 134 km in the north-south direction and an average east-west extent is 52 km. The topography of the district is dissected by basins of westward flowing rivers namely Patalganga, Amba, Kundalika, Kal, and Savitri. The study area falls within the Western Ghat region wherein the maximum elevation is 520 m and the width of the coastal belt in this region is about 50 km. The Mahad region is part

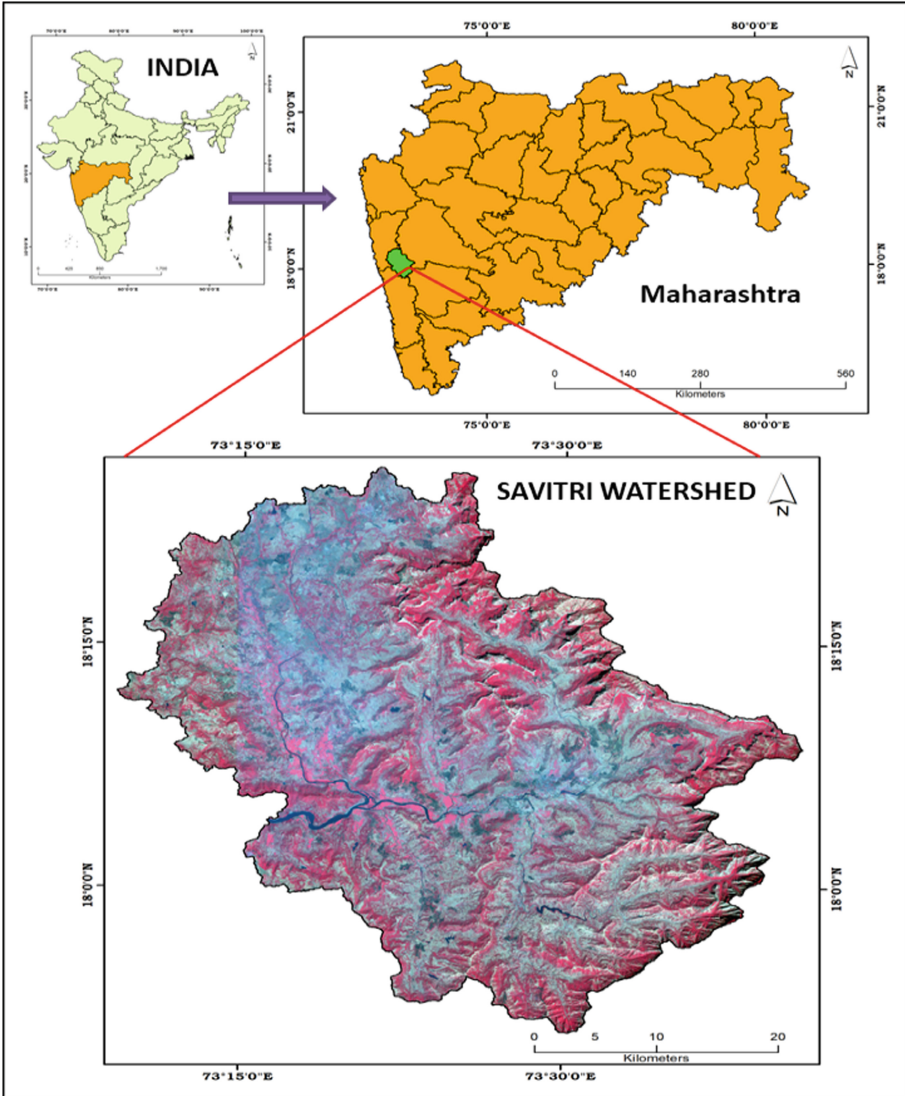


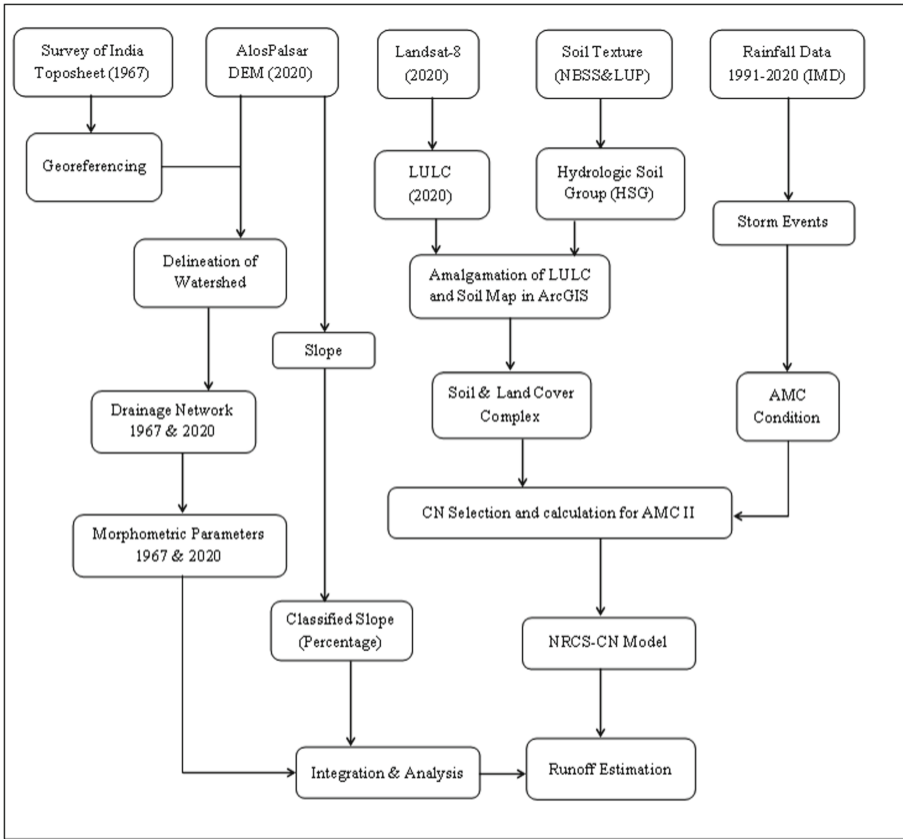
Fig. 1. Location map of Savitri watershed

of the Konkan Coastal Belt from the Raigad district of Maharashtra. This region is traversed by westerly flowing Savitri River and its tributaries. The major tributaries of Savitri are Kal River, Gandari River, Ghodnala, Kalnadi, Negeshrinadi. The study area is bounded between  $17^{\circ} 51' 5''$  North to  $18^{\circ} 25' 56''$  North Latitude and  $73^{\circ} 9' 18''$  East to  $73^{\circ} 41' 3''$  East Longitude and includes about 1966.34 sq. km. The area is covered by Survey of India topographic maps numbers of 47F/3, 47F/4, 47F/7, 47F/8, 47F/11, 47F/12, 47G/5, 47G/9 of 1:50,000 scale. In the study area, most of the drainages were controlled by structural features and originated from the plateau top and make it highly dissected in nature. Different geomorphic features like a dissected plateau, debris slope, pediment, and Padi plain complexes, and younger alluvial plain are found in the area. The study region receives an average annual rainfall of 3413 mm per year. The study region was affected by landslides due to heavy rainfall particularly during southwest monsoon (June to September); for example in 1992 (20<sup>th</sup> August), 1994 (24<sup>th</sup> August), 2005 (25<sup>th</sup> and 26<sup>th</sup> July), 2018 (5<sup>th</sup> July) caused huge damages to properties, injuries and death of people.

### 3 Morphometric Analysis

The flow chart of the adopted methodology is presented in Fig. 2. Initially, the base map of the Savitri watershed is delineated using a set of geo-referenced Survey of India (SoI) topographical maps viz. 47F/3, 47F/4, 47F/7, 47F/8, 47F/11, 47F/12, 47G/5, 47G/9 (R.F 1:50,000) and later verified with ALOS PALSAR data of resolution 30 m in GIS platform. The main objective of the present research is to prepare a comparative study of morphometric parameters extracted from two datasets separately - a) Topographical maps (1:50,000 scale) for 1967 and b) ALOS-Phased Array type L-band Synthetic Aperture Radar (PALSAR) digital elevation model (DEM) (30 m) for 2020 (Rajasekhar et al. 2018). The comparative assessment is undertaken to understand the hydrological characteristics of the basin over different time scales. Thus, the derived information of the basin properties will enhance to estimate of the rainfall-runoff relationship that would further predict the occurrences of flood peak in a basin (Harsha et al. 2020; Abdulkareem et al. 2017).

Extraction of Morphometric attributes from topographical sheets is traditional as it is manually computed but recently, it has been overcome by the use of digital datasets having more global coverage with better resolution (Fenta et al. 2017; Kandy and Javed 2017). For the present work, the parameters calculated using topographical maps are considered as the base for comparing with that derived from ALOS PALSAR DEM and is validated with Google earth imageries/country points. Within the framework for assessing Morphometric variables, three aspects such as linear, areal, and relief involving the variables such as stream order, stream number, stream length, form factor, elongation ratio, circularity ratio, drainage density, stream frequency, relative relief, absolute relief, etc. are selected for the study. The description of numerous Morphometric properties (Table 1) and their comparative assessment is represented in (Table 2). The comparative study is conducted to see the variation between the two datasets as well as to detect the changes undergoing by the basin over the period. (Dikpal et al. 2017; Soni 2017; Chandrashekar et al. 2015; Vincy et al. 2012, Malik et al. 2019; Balasubramanian et al. 2017).



**Fig. 2.** Methodology flow chart for runoff estimation

**Table 1.** Standard methods of morphometric attributes

Sr. No.	Morphometric attributes	Methods
<b>Drainage network</b>		
1	Stream order (u)	Hierarchical rank
2	Stream numbers (Nu)	$Nu = N1 + N2 + N3 + \dots Nn$
3	Stream length (Lu)	$Lu = L1 + L2 \dots Ln$
4	Bifurcation ratio	$Rb = Nu/Nu + 1$
5	Main channel length (MC)	GIS analysis
6	Sinuosity (Si)	$Si = VL/LB$
<b>Basin geometry</b>		

(continued)



**Table 1.** (continued)

Sr. No.	Morphometric attributes	Methods
7	Watershed area (A)	GIS analysis
8	Basin length (LB)	GIS analysis
9	Basin perimeter (Pr)	GIS analysis
10	Basin width (W)	$W = A/LB$ (km)
11	Circularity ratio (Rc)	$Rc = 4\pi A/P^2$
12	Elongation ratio (Re)	$Re = d/(Lb)$
13	Texture ratio (Rt)	$Rt = \sum Nu/Pr$
14	Form factor ratio (FFR)	$A/LB^2$
15	Basin shape index (Ish)	$Ish = 1.27A/LB^2$
<b>Drainage texture</b>		
16	Stream frequency (Fs)	N/A, N is the total stream number
17	Drainage density (Dd)	L/A, L is total stream length
18	Drainage intensity (Di)	$Di = Fs/Dd$
19	Length of overland flow (Lo)	1/2D
20	Infiltration number (FN)	$FN = Ds * Fs$
<b>Relief properties</b>		
21	Maximum elevation (H)	GIS analysis
22	Minimum elevation (h)	GIS analysis
23	Relief (Rf)	$Rf = H-h$
24	Relief ratio (Rr)	$Rr = (Rf/LB) * 100$
25	Ruggedness number (Rn)	$Rn = Rf.D$
26	Mean Elevation (Hm)	GIS analysis

**Table 2.** Morphometric attributes of Savitri watershed derived from toposheet and DEM

Morphometric attributes	Computed value	
	Toposheet (1967)	DEM (2020)
<b>Drainage network</b>		
Stream orders	7	7
Stream numbers	10132	6753
Stream length (km)	6490.89	5655.86
Mean Bifurcation ratio	3.83	3.8
Main channel length (km)	73.69	68.13

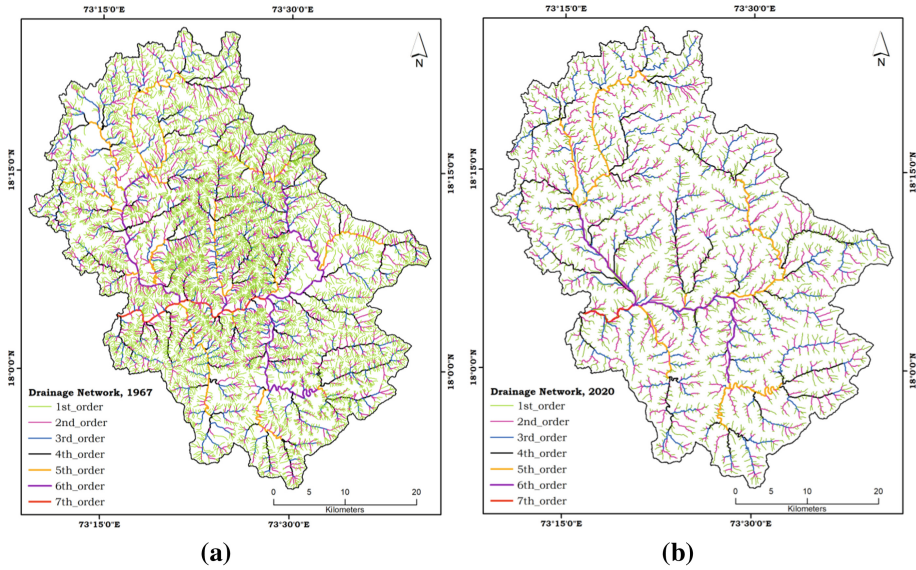
(continued)

**Table 2.** (continued)

Morphometric attributes	Computed value	
	Toposheet (1967)	DEM (2020)
Sinuosity	1.45	1.39
<b>Basin geometry</b>		
Watershed area (Sq. Km)	1966.34	1966.34
Basin length (km)	40.9	40.06
Basin perimeter (km)	361	361
Basin width (km)	48.07	49.08
Circularity ratio	0.2	0.2
Elongation ratio	0.8	0.8
Texture ratio	28.06	13.16
Form factor ratio	0.47	0.47
Basin shape index	1.52	1.55
Stream frequency (sq.km)	5.15	3.43
Drainage density (sq.km)	3.3	2.87
Drainage intensity	1.56	1.19
Length of overland flow (km)	1.65	0.8
Infiltration number	17	9.87
<b>Relief characteristics</b>		
Maximum elevation (m)	1100	1401
Minimum elevation (m)	20	2
Relief	1080	1399
Relief ratio		
Ruggedness number	3.56	4.01
Mean elevation	332	701

#### 4 Comparative Assessment of Morphometric Parameters Extracted from Different Datasets

The Morphometric parameters undertaken for the present study are presented in Table 1. Based on the selected indicators, a comparative analysis is prepared using manual and digital extraction procedures for the years 1967 and 2020 in the GIS platform shown in Fig. 3. This comparison analysis would help in synthesizing the changes in hydrological behavior of a particular river basin affecting the runoff flow in the different periods. It is noteworthy that the map scale and DEM resolution are vital in the extraction of various quantitative factors.



**Fig. 3.** (a) Drainage network, 1967 and (b) Drainage network, 2020

Stream order ( $u$ ) happens to be the foremost step in any quantitative study (Rai. et al. 2019) wherein Strahler's stream ordering is widely followed based on the hierarchical ranking of streams. The stream ordering of the Savitri watershed is classified as a seventh-order basin with a dendritic drainage pattern. While extracting from topographical maps, the total number of streams ( $N_u$ ) calculated was 10132 having a stream length ( $L_u$ ) of 6490.89 km and the stream orders extracted from DEM are 4753 with a total length of 3151.08 km respectively. The stream length is an important variable as it provides information about run-off characteristics. Moreover, the bifurcation ratio ( $R_b$ ) indicates the degree of integration prevailing among the stream orders within a basin (Rai. et al. 2014). The mean bifurcation ratio of the watershed derived from both the sources are similar i.e. 3.8 that describes lesser influence by the underlying structure on drainage network. The main channel is considered as a stream segment that is joined to constitute the next hierarchical order (Kaliraj et al. 2014) and the calculated channel length ( $L$ ) found varies from 73.69 km to 68.13 km from 1967 to 2020. Moreover, the sinuosity of the basin ranges from 1.45 (toposheet) to 1.39 (DEM) indicating the straight-sinuuous channel of the Savitri river.

The basin geometry refers to the varied shape of a watershed that controls the rate at which water is provided to the main channel (Fenta et al. 2017). The total area of the Savitri watershed extracted from both topographical maps and DEM is 1966.34 km<sup>2</sup> and the basin perimeter i.e., the outer boundary of the watershed found is 361 km. However, the circularity ratio of the basin is 0.2 representing a lesser circular shape while the elongation ratio is 0.8 which indicates that the region is covered by high relief with gentle to steep ground slopes (Schumn 1956). Another striking parameter is the form factor which specifies that the lesser the form factor value, the more the basin will be elongated and vice-versa. The calculated form factor of the present watershed is 0.47

indicating elongation shapes that define the flatter peak of low flow for a longer time. Drainage density (Dd) refers to the closeness of spacing between channels and it is calculated as the total length of stream segments to the basin area (Meshram and Sharma 2015). The computed value of Dd extracted from toposheet is 3.3 km/km<sup>2</sup> and DEM is 2.87 km/km<sup>2</sup> which specifies that the region had fewer infiltration rates and more runoff but in later years the Dd value decreased that indicates more infiltration rate and moderate runoff. In contrast, the stream frequency (f) derived is 5.15 streams/km<sup>2</sup> (toposheet) and 3.43 streams/km<sup>2</sup> exhibiting a positive correlation to drainage density.

The relief aspects represent three-dimensional characteristics primarily depending upon the maximum and minimum height of the basin (Venkatesh and Anshumali 2019) mainly affecting the runoff and sediment transport. The basin relief as derived from the topographical map (20 m contour interval) was 1080 m while the relief from DEM is 1399 m. The resultant values are responsible for the presence of some steep slopes and high relief governing the watershed.

Relief ratio forms an effective measure to gradient aspects of the watershed. The Rr value of 26.40 km (toposheet) and 34.92 (DEM) denotes the presence of hilly terrain with low permeability (Prakash et al. 2017). Ruggedness number implies the structural complexity of the terrain and the computed Rn value for the present watershed varies from 3.56 (toposheet) to 4.01 (DEM) indicating that the region is highly erosion-prone operating along the slopes.

## 5 Runoff Estimation Using NRCS-CN

Now, the enumerated Morphometric variables were matched with both the datasets for the Savitri basin to evaluate its effect on runoff potential. The basin properties have exerted a strong influence on hydrologic variables and therefore the estimation and prediction of runoff amount are further determined with the help of the Natural Resources Conservation Service-Curve Number (NRCS-CN) method described in this chapter.

After the enumeration of the selected quantitative attributes necessary to understand the hydrological characteristics, it is significant to estimate the runoff flow governing in a certain watershed (Savita et al. 2017). To achieve this, NRCS-CN is applied along with the parameters viz. rainfall, land use and land cover, slope, and soil texture maps that will provide a combined hydrologic effect (Abdulkareem et al. 2017). For the preparation of the rainfall map, the average annual rainfall data is collected from 1991–2020 for 30 years from the Indian Meteorological Department (IMD). The land use and landcover map is generated from LANDSAT 8 imagery of 2020 using a supervised classification approach. In contrast, the soil texture map is prepared based on the National Bureau of Soil Survey and Land Use Planning (NBSS&LUP), and the resultant map is converted into hydrologic soil groups viz. A, B, C, and D depending on their soil infiltration capacity (Adham et al. 2014; Satheeshkumar et al. 2017). The produced LULC map is overlaid upon the hydrologic soil group and on this basis; a Curve Number (CN) is allotted for preparation of soil cover complex map. Further, this process is accompanied by integrating the obtained soil cover complex map and Antecedent Moisture Condition (AMC), allotting actual curve number (CN) values thereby calculating maximum retention (S) and initial abstraction (*I<sub>a</sub>*) that finally leads to runoff estimation (Satheeshkumar et al. 2017, Rawat and Singh 2017; Ajmal et al. 2014).

## 6 NRCS-CN Model

The United States Department of Agriculture (USDA) and Soil Conservation Services (SCS) have developed the most popular and common method to determine runoff within a watershed in the 1950s. The model was formerly known as the SCS-CN model and later renamed Natural Resources Conservation Service (NRCS) (Pancholi et al. 2015). This method is also known as Curve Number (CN) that was evolved primarily for small agricultural watersheds (Rawat and Singh 2017). This technique incorporates several influencing factors for runoff generation viz. rainfall, soil, land cover, slope, and antecedent moisture conditions (AMCs) in a single CN parameter (Kumar et al. 2017). Thus, the CN method is based on the assumption of proportionality between retention and runoff (Bansode and Patil 2014) that is derived by the following expression

$$Q = \frac{(P - Ia)^2}{P - Ia + S} \quad (1)$$

Where,  $Q$  = runoff (mm),

$P$  = rainfall depth (mm),

$S$  = potential maximum retention after runoff begins (mm),

$Ia$  = initial abstraction (mm).

Initial abstraction ( $Ia$ ) is determined based on antecedent moisture conditions. It involves surface storage, interception, evaporation, and infiltration before the runoff in the watershed (Kumar et al. 2017).  $Ia$  has been taken as  $0.3S$  for Indian condition (Ahmad et al. 2015) and hence, the empirical relationship can be represented as,

$$Ia = 0.3S \quad (2)$$

Substituting Eq. (2) in Eq. (1); we get,

$$Q = \frac{(P - 0.3S)^2}{P + 0.7S} \quad (3)$$

Moreover, parameter  $S$  indicates the potential infiltration after runoff begins derived by the following equation.

$$S = \left( \frac{25400}{CN} \right) - 254 \quad (4)$$

Where,  $CN$  stands for curve number, the values of which can be obtained from the SCS Handbook of Hydrology (NEH-4), (USDA 1972) depending on land cover, HSG, and AMC. It is noteworthy that the NRCS-CN method is revised for runoff assessment in big watersheds by weighing curve numbers concerning basin land cover area. The equation for calculating the weighted curve number is as

$$CN_w = \sum CN_i \times \frac{A_i}{A} \quad (5)$$

Where,  $CN_w$  is the weighted curve number;

$CN_i$  is the curve number from 1 to any number  $N$ ;

$A_i$  is the area with curve number  $CN_i$ ; and

$A$  is the total area of the watershed.

## 7 Antecedent Moisture Condition (AMC)

Antecedent Moisture Condition refers to the availability of moisture content in the soil before a storm event. It is determined by total rainfall in 5 day period preceding a day of analysis (Askar 2013; Vinithra and Yeshodha 2013). Few properties of the basin viz. LULC and soil types of the basin, AMC, and recharge capacity of the basin are significant for computing the curve number method (Jasrotia et al. 2002). The Natural Resource Conservation Service (NRCS) had developed three antecedent soil moisture conditions namely AMC-I, AMC-II, and AMC-III representing dry, normal, and wet conditions, respectively (Askar 2013; Amutha and Porchelvan 2009; Pandey and Stuti 2017) for dormant and growing seasons as shown in Table 3. In the current research, average condition i.e. AMC II is chosen to obtain the CN value for this purpose.

**Table 3.** AMC classes for computation of CN values (Ref.: Amutha and Porchelvan 2009)

AMC group	Soil characteristics	Five-day antecedent rainfall in mm	
		Dormant season	Growing season
I	Soils are dry but not to the wilting point; satisfactory cultivation has taken place	Less than 13	Less than 36
II	Average Condition	13–28	36–53
III	Heavy rainfalls or light rainfall and low temperatures have occurred within the last 5 days; staled soil	Over 28	Over 53

## 8 Hydrologic Soil Group (HSG)

Soil types are fundamental in the generation of runoff as varied soil types exhibit different infiltration rates. The infiltration rates of soils vary depending upon the nature of subsurface permeability. For the estimation of runoff, curve number (CN) values for individual soil types are necessary.

As per National Engineering Handbook (NEH) developed by the USDA, soils are categorized into four groups viz., A, B, C, and D according to the soil's infiltration rate, texture, depth, drainage condition, and water transmission (Rawat and Singh 2017) (Table 4). The present watershed is mainly dominated by the C soil group indicating clay loam and shallow sandy loam soil with slow infiltration capacity.

**Table 4.** Soil Conservation Service classification (USDA 1974)

Hydrologic soil groups (HSGs)	Soil textures	Water transmission	Runoff potential	Final infiltration
A	Deep, well-drained to excessively drained sand or gravel	Rapid rate	Low	>7.5
B	Moderately deep to deep, moderately well-drained to well-drained soils of moderately fine to moderately coarse texture	Moderate rate	Moderate	3.8–7.5
C	Clay loams, shallow sandy loam, soils with moderately fine to fine textures	Slow rate	Moderate	1.3–3.8
D	Clay soils that swell significantly when wet, heavy plastic, and soils with a permanent high water table	Very slow rate	High	<1.3

## 9 Area Weighted Curve Number

The distinct layers of HSGs, LULC, and AMC are overlaid and a new polygon attribute table (PAT) is achieved using ArcGIS. The result obtained from the new PAT is used to determine the total area-weighted curve number (WCN) of the watershed. The computed weighted curve number (WCN) of the watershed is 81.14 as presented in Table 5.

**Table 5.** Weighted curve number for Savitri watershed

LULC	HSG	CN	Area (km <sup>2</sup> )		% Area	% Area*CN	Weighted curve number (WCN)
Barren land	C	83	2.08	7.89	0.11	8.77	<b>81.14</b>
	D	87	5.82		0.30	25.75	

(continued)

**Table 5.** (continued)

LULC	HSG	CN	Area (km <sup>2</sup> )		% Area	% Area*CN	Weighted curve number (WCN)
Built-up (urban and rural)	C	90	0.12	7.05	0.01	0.55	
	D	95	6.93		0.35	33.50	
Crop land	A	67	1.88	750.54	0.10	6.42	
	B	78	0.09		0.00	0.37	
	C	85	243.10		12.37	1051.67	
	D	89	505.47		25.73	2289.63	
Deciduous broad leaf forest	A	42	0.15	197.82	0.01	0.33	
	C	79	83.76		4.26	336.77	
	D	85	113.91		5.80	492.78	
Evergreen broad leaf forest	C	71	124.14	142.80	6.32	448.59	
	D	77	18.66		0.95	73.13	
Fallow land	C	88	33.16	56.70	1.69	148.50	
	D	90	23.54		1.20	107.83	
Mangrove forest	C	98	0.12	0.12	0.01	0.60	
Mixed forest	A	38	8.91	262.70	0.45	17.22	
	C	75	137.76		7.01	525.86	
	D	81	116.03		5.91	478.33	
Permanent wetland	D	78	7.85	7.85	0.40	31.16	
Plantation	B	53	0.60	80.26	0.03	1.63	
	C	67	57.30		2.92	195.41	
	D	72	22.35		1.14	81.90	
Shrub land	A	36	2.86	416.10	0.15	5.24	
	C	73	267.82		13.63	995.06	
	D	79	145.42		7.40	584.69	
Water bodies	A	97	0.75	34.98	0.04	3.72	
	C	97	21.11		1.07	104.23	
	D	97	13.11		0.67	64.75	

## 10 Runoff Estimation Through NRCS Model

To run the NRCS-CN model in the Savitri watershed, a set of variables such as rainfall, soil types, LULC, slope, and AMC have been taken into account to estimate runoff flow within the basin. The land use and land cover (LULC) map (Fig. 4) of the study area have been prepared using satellite imagery for the year 2020 in the GIS platform. Based on LULC classification, the Savitri watershed has been classified into twelve classes viz. barren land, fallow land, cropland, deciduous broadleaf forest, evergreen broadleaf forest, mangrove forest, mixed forest, built-up (urban and rural), permanent wetland,



plantation, shrubland, and water bodies. On one hand, the dominant class is cropland covering an area of 750.54 km<sup>2</sup> followed by shrubland and forest while mangrove forest occupies a negligible area of 0.12 km<sup>2</sup>.

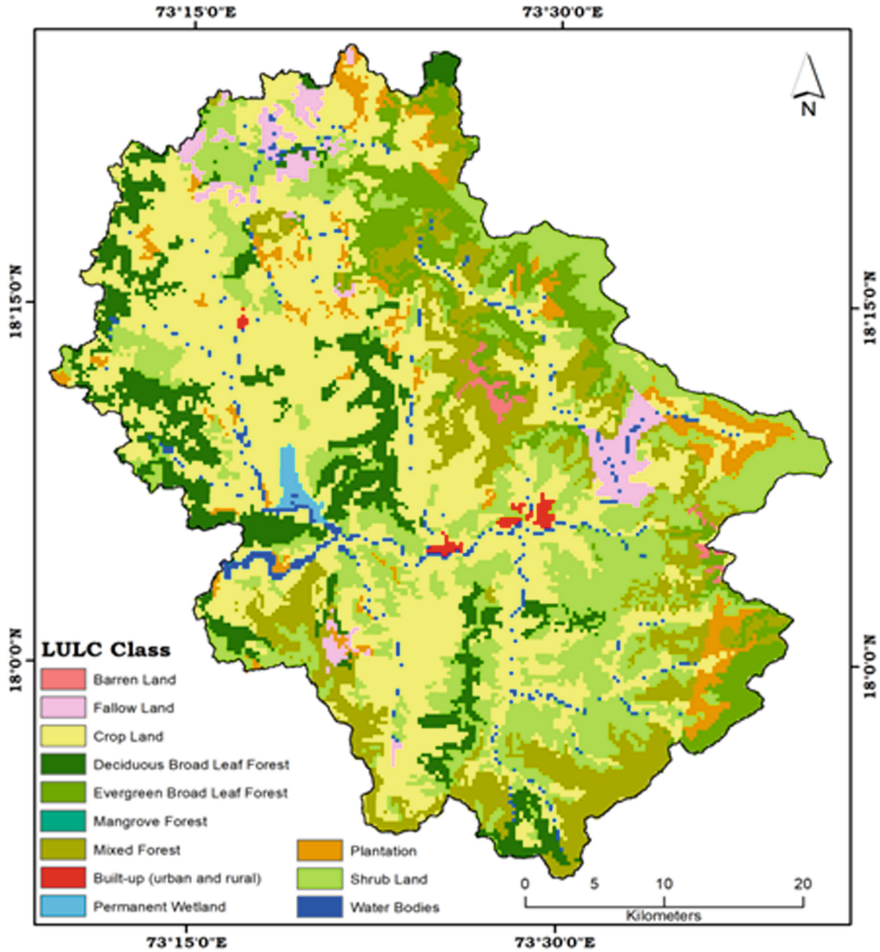


Fig. 4. LULC map

The average annual rainfall of the region for 30 years is taken under consideration wherein rainfall ranges from 30.51 mm to 257.95 mm from 1991 to 2020. However, another parameter i.e. slope of a region plays a pivotal role in determining the runoff characteristics as the steep slope will fasten the runoff rate with the least water holding capacity and the gentle slope will slow the rate with maximum water retention capacity. The slope map (Fig. 5) of the Savitri watershed represents four classes viz. nearly level, gentle, moderate, and steep. About 1639.47 km<sup>2</sup> (83.44%) falls under the nearly level and gentle category while 325.34 (16.55%) km<sup>2</sup> comes under moderate to the steep

category that indicates that the area has more water retention capacity causing lesser runoff amount.

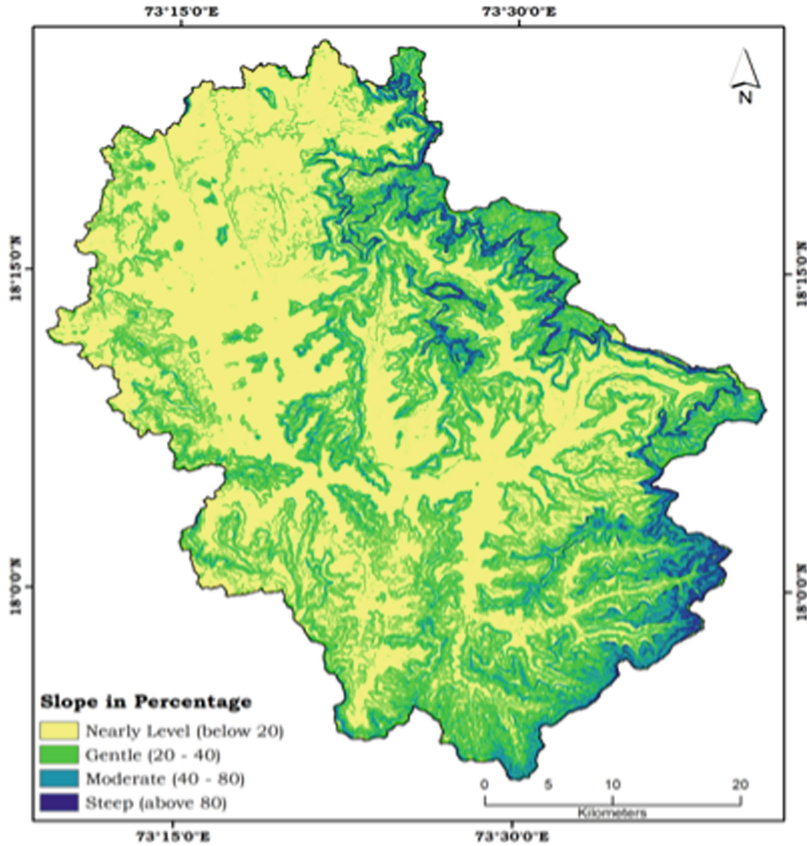


Fig. 5. Slope map

The soil texture map (Fig. 6: (a)) speculates that most of the region is covered by loamy soil ( $1294.71 \text{ km}^2$ ) followed by clayey ( $598.45 \text{ km}^2$ ) and sandy soil ( $60.77 \text{ km}^2$ ). Moreover, the Hydrological Soil Group (HSG) map (Fig. 6:(b)) depicts that the maximum area of the Savitri watershed falls under Group C composing of clayey loam with moderate water transmission rate. Thus, these parameters coupled with distinct CN values (Fig. 6: (c)) and AMC conditions are requisite for the application of the NRCS model in the watershed to determine the runoff amount from 1991–2020.

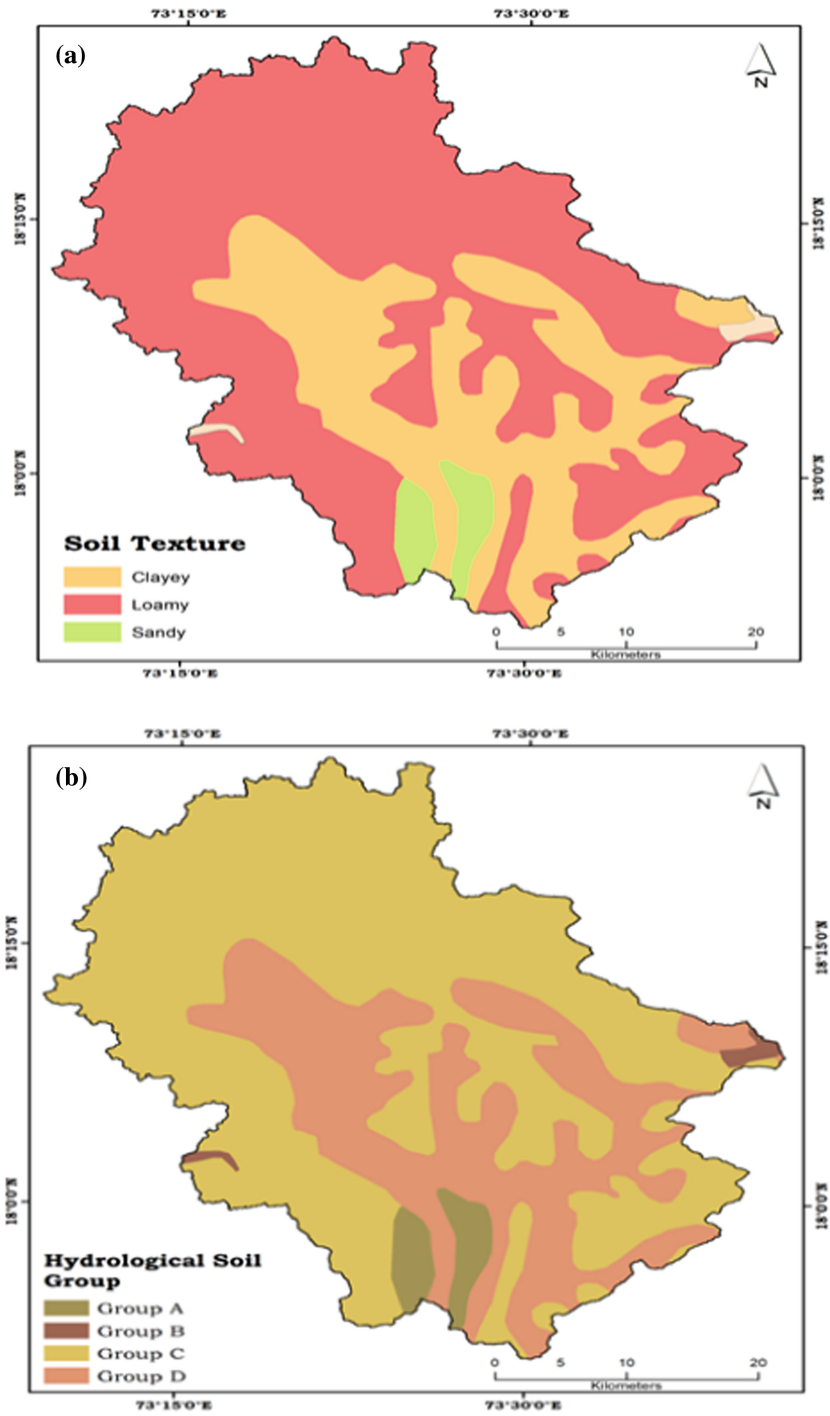


Fig. 6. (a) Soil texture map, (b) Hydrological soil group map, (c) CN-II Map

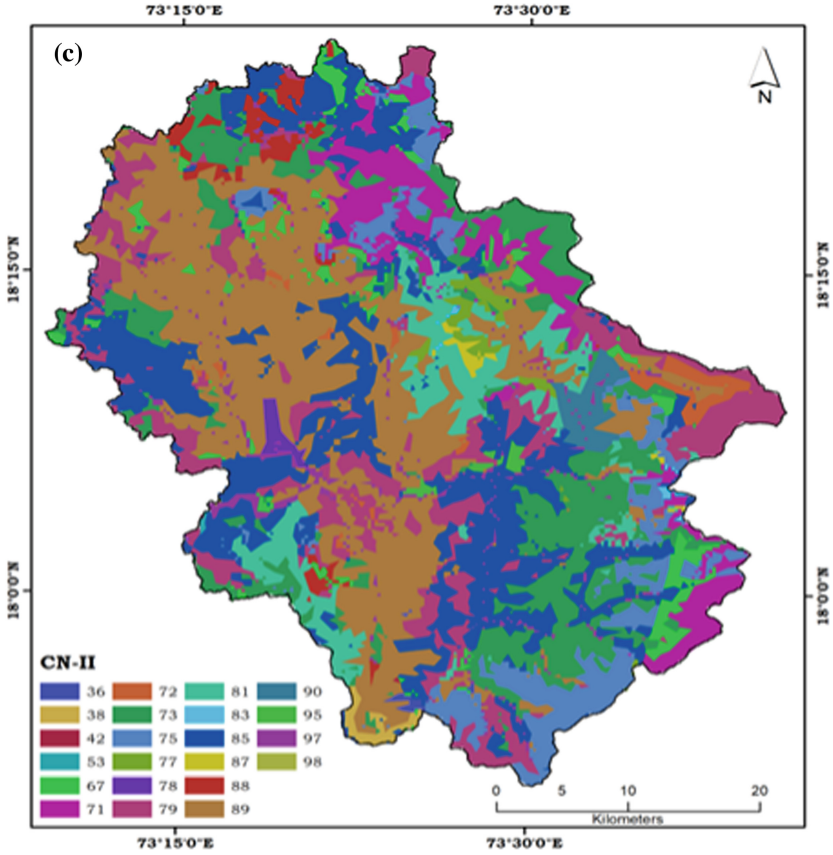


Fig. 6. (continued)

## 11 Rainfall-Runoff Estimation

To assess the flood condition of a certain area, it's vital to understand and predict the rainfall-runoff relationship (Kumar et. al. 2017) governing in a basin so that planning and management of water resources could be analyzed systematically. The average annual rainfall and runoff of the basin during 1991 and 2020 are calculated as 303.51 mm and 236.87 mm while in 2020 are 257.95 mm and 192.85 mm respectively (Fig. 7). The runoff volume (product of runoff and a total area of the watershed) is another significant indicator (Adham et.al. 2014) wherein it extends from 465396.43 m<sup>3</sup> in 1991 to 378903.53 m<sup>3</sup> in 2020 (Table 6). Similarly, the average runoff and runoff volume for 30 years are computed as 233.65 mm and 459075.58 m<sup>3</sup>. Also, the scatter plot (Fig. 8) depicts the relationship between rainfall and runoff wherein the correlation coefficient (r) value is 1 that signifies a perfectly positive correlation between the variables.

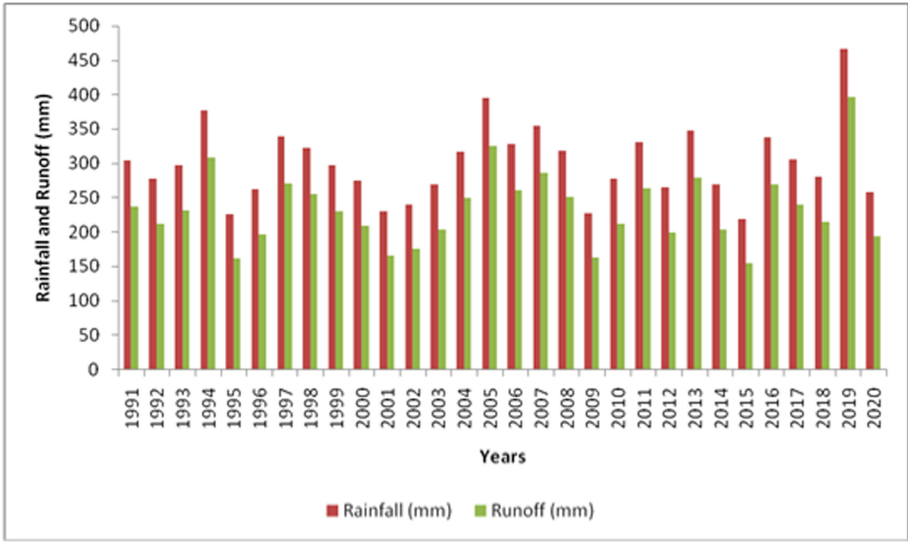


Fig. 7. Annual rainfall and runoff of Savitri Watershed

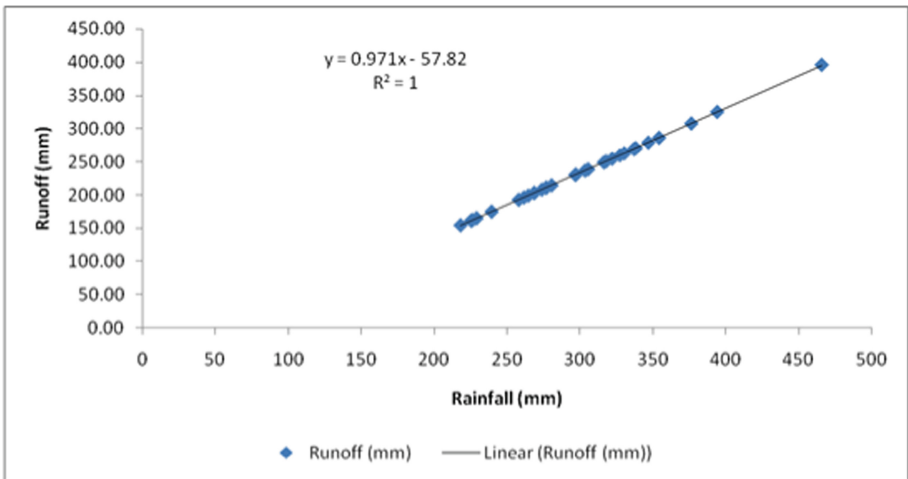


Fig. 8. Co-relationship between annual average SCS-CN runoff (mm) and annual rainfall (mm)

Table 6. Computation of runoff and volume (1991–2020)

Years	Rainfall (mm)	Runoff (mm)	Volume (m <sup>3</sup> ) = Runoff × Area
1991	303.51	236.87	465396.43
1992	276.87	211.07	414716.89

(continued)

**Table 6.** (continued)

Years	Rainfall (mm)	Runoff (mm)	Volume (m <sup>3</sup> ) = Runoff × Area
1993	297.32	230.86	453597.34
1994	376.49	308.08	605318.55
1995	225.23	161.56	317424.25
1996	261.56	196.32	385723.72
1997	338.35	270.78	532027.64
1998	322.12	254.96	500944.43
1999	296.79	230.35	452587.69
2000	273.82	208.13	408932.55
2001	229.02	165.16	324510.66
2002	239.33	175.00	343837.16
2003	268.59	203.09	399023.37
2004	316.43	249.42	490064.42
2005	394.26	325.51	639564.36
2006	327.41	260.11	511067.89
2007	354.29	286.35	562619.79
2008	318.08	251.03	493218.45
2009	226.26	162.54	319349.11
2010	276.81	211.02	414603.06
2011	330.39	263.02	516774.11
2012	264.59	199.23	391453.11
2013	346.96	279.19	548544.61
2014	268.65	203.14	399136.98
2015	218.01	154.70	303953.68
2016	337.04	269.50	529516.21
2017	305.64	238.94	469459.53
2018	280.53	214.61	421663.31
2019	466.02	396.14	778334.58
2020	257.95	192.85	378903.53
<b>Average</b>	<b>299.94</b>	<b>233.65</b>	<b>459075.58</b>

## 12 Conclusions

The present research explains the significance of quantitative assessment to understand the geohydrological processes operating in the basin. Investigation of Morphometric properties plays an important role in evaluating the response of a basin to climate change, drainage, and flood risk vividly. Thus, there exists a relationship between the quantitative attributes and flood potential necessary for flood forecasting in a basin. The comparison of Morphometric indices for Savitri watershed based on traditional and digital datasets for two time periods have evolved contrasting results. Within the framework of Morphometric variables, the values of stream number, stream length, main channel length, drainage density, frequency, intensity, length of overland flow, infiltration number, etc. have decreased substantially over time attributed to physical and human-induced factors. The comparisons have been incorporated to examine the variability in the rainfall-runoff relationship that can be accessed from the basin properties. Due to the unavailability of rainfall data before the 1990s, a total of 30 years have been taken into account from 1991–2020. The maximum average annual rainfall and runoff was observed in 2019 as 466.02 mm and 396.14 mm. The NRCS model is employed in the Savitri watershed indicating that previously the region experienced high rainfall and runoff while now the region encounters moderate runoff conditions due to a decrease in rainfall and other parameters. Furthermore, the curve numbers were derived for different hydrologic soil groups and it was found that the study area mostly falls under group C soil category which infers lower infiltration rate and moderate runoff flow. Therefore, this study might be a base for planning and managing water resources required for hydrological modeling to harness the potentialities sustainably within a watershed.

## References

- Abdulkareem, J.H., Pradhan, B., Sulaiman, W.N.A., Jamil, N.R.: Quantification of runoff as influenced by morphometric characteristics in a rural complex catchment. *Earth Syst. Environ.* **2**(1), 145–162 (2018). <https://doi.org/10.1007/s41748-018-0043-0>
- Adham, M.I., Shirazi, S.M., Othman, F., Rahman, S., Yusop, Z., Ismail, Z.: Runoff potentiality of a watershed through SCS and functional data analysis technique. *Sci. World J.* (2014). <https://doi.org/10.1155/2014/379763>
- Agarwal, R., Garg, P.K., Garg, R.D.: Remote sensing and GIS based approach for identification of artificial recharge sites. *Water Resour. Manag.* **27**(7), 2671–2689 (2013). <https://doi.org/10.1007/s11269-013-0310-7>
- Agidew, A.-M., Singh, K.N.: Factors affecting farmers' participation in watershed management programs in the Northeastern highlands of Ethiopia: a case study in the Teleyayen sub-watershed. *Ecol. Process.* **7**(1), 1–15 (2018). <https://doi.org/10.1186/s13717-018-0128-6>
- Ahmad, I., Verma, V., and Verma, M.K.: Application of curve number method for estimation of runoff potential in GIS environment. In: 2nd International Conference on Geological and Civil Engineering, vol. 80, no. 4, pp. 16–20 (2015). <https://doi.org/10.7763/IPCBEE.2015.V80.4>
- Ajmal, M., Moon, G.W., Ahn, J.H., Kim, T.W.: Investigation of SCS-CN and its inspired modified models for runoff estimation in South Korean watersheds. *J. Hydro-Environ. Res.* **9**(4), 592–603 (2015). <https://doi.org/10.1016/j.jher.2014.11.003>
- Amutha, R., Porchelvan, P.: Estimation of surface runoff in Malattar sub-watershed using SCS-CN method. *J. Indian Soc. Rem. Sens.* **37**(2), 291 (2009). <https://doi.org/10.1007/s12524-009-0017-7>

- Askar, M.K.: Rainfall-runoff model using the SCS-CN method and geographic information systems: a case study of Gomal river watershed. *WIT Trans. Ecol. Environ.* **178**, 159–170 (2013). <https://doi.org/10.2495/WS130141>
- Balasubramanian, A., Duraisamy, K., Thirumalaisamy, S., Krishnaraj, S., Yatheendradasan, R.K.: Prioritization of subwatersheds based on quantitative morphometric analysis in lower Bhavani basin, Tamil Nadu, India using DEM and GIS techniques. *Arab. J. Geosci.* **10**(24), 1–18 (2017). <https://doi.org/10.1007/s12517-017-3312-6>
- Bansode, A., Patil, K.A.: Estimation of runoff by using SCS curve number method and arc GIS. *Int. J. Sci. Eng. Res.* **5**(7), 1283–1287 (2014)
- Chandrashekar, H., Lokesh, K.V., Sameena, M., Ranganna, G.: GIS-based morphometric analysis of two reservoir catchments of Arkavati River, Ramanagaram District, Karnataka. *Aquat. Procedia* **4**, 1345–1353 (2015). <https://doi.org/10.1016/j.aqpro.2015.02.175>
- Clarke, J.I.: Morphometry from maps, pp. 235–274. *Essays in Geomorphology*. Heinmann, London (1966)
- Dikpal, R.L., Renuka Prasad, T.J., Satish, K.: Evaluation of morphometric parameters derived from Cartosat-1 DEM using remote sensing and GIS techniques for Budigere Amanikere watershed, Dakshina Pinakini Basin, Karnataka, India. *Appl. Water Sci.* **7**(8), 4399–4414 (2017). <https://doi.org/10.1007/s13201-017-0585-6>
- Fenta, A.A., Yasuda, H., Shimizu, K., Haregeweyn, N., Woldearegay, K.: Quantitative analysis and implications of drainage morphometry of the Agula watershed in the semi-arid northern Ethiopia. *Appl. Water Sci.* **7**(7), 3825–3840 (2017). <https://doi.org/10.1007/s13201-017-0534-4>
- Harsha, J., Ravikumar, A.S., Shivakumar, B.L.: Evaluation of morphometric parameters and hypsometric curve of Arkavathy river basin using RS and GIS techniques. *Appl. Water Sci.* **10**(3), 1–15 (2020). <https://doi.org/10.1007/s13201-020-1164-9>
- Jasrotia, A.S., Dhiman, S.D., Aggarwal, S.P.: Rainfall-runoff and soil erosion modeling using remote sensing and GIS technique—a case study of tons watershed. *J. Indian Soc. Rem. Sens.* **30**(3), 167–180 (2002). <https://doi.org/10.1007/BF02990649>
- Khanday, M.Y., Javed, A.: Hydrological investigations in the semi-arid Makhawan watershed, using morphometry. *Appl. Water Sci.* **7**(7), 3919–3936 (2017). <https://doi.org/10.1007/s13201-017-0545-1>
- Mahala, A.: The significance of morphometric analysis to understand the hydrological and morphological characteristics in two different morpho-climatic settings. *Appl. Water Sci.* **10**(1), 1–16 (2019). <https://doi.org/10.1007/s13201-019-1118-2>
- Meshram, S.G., Sharma, S.K.: Prioritization of watershed through morphometric parameters: a PCA-based approach. *Appl. Water Sci.* **7**(3), 1505–1519 (2015). <https://doi.org/10.1007/s13201-015-0332-9>
- Pandey, A.C., and Stuti.: Geospatial technique for runoff estimation based on SCS-CN method in upper South Koel River Basin of Jharkhand (India). *Int. J. Hydrol.* **1**(7), 213–220 (2017). DOI: <https://doi.org/10.15406/ijh.2017.01.00037>
- Pathare, J.A., Pathare, A.R.: Prioritization of micro-watershed based on morphometric analysis and runoff studies in upper Darna basin, Maharashtra, India. *Model. Earth Syst. Environ.* **6**(2), 1123–1130 (2020). <https://doi.org/10.1007/s40808-020-00745-6>
- Prabhakaran, A., Jawahar Raj, N.: Drainage morphometric analysis for assessing form and processes of the watersheds of Pachamalai hills and its adjoinings, Central Tamil Nadu, India. *Appl. Water Sci.* **8**(1), 1–19 (2018). <https://doi.org/10.1007/s13201-018-0646-5>
- Prakash, K., Mohanty, T., Pati, J.K., Singh, S., Chaubey, K.: Morphotectonics of the Jamini River basin, Bundelkhand Craton, Central India; using remote sensing and GIS technique. *Appl. Water Sci.* **7**(7), 3767–3782 (2016). <https://doi.org/10.1007/s13201-016-0524-y>
- Rai, P.K., Mohan, K., Mishra, S., Ahmad, A., Mishra, V.N.: A GIS-based approach in drainage morphometric analysis of Kanhar River Basin, India. *Appl. Water Sci.* **7**(1), 217–232 (2014). <https://doi.org/10.1007/s13201-014-0238-y>



- Rai, P.K., Singh, P., Mishra, V.N., Singh, A., Sajan, B., Shahi, A.P.: Geospatial Approach for Quantitative Drainage Morphometric Analysis of Varuna River Basin. *India J. Landscape Ecol.* **12**(2), 1–25 (2019). <https://doi.org/10.2478/jlecol-2019-0007>
- Rajasekhar, M., Raju, G.S., Raju, R.S., Ramachandra, M., Kumar, B.P.: Data on comparative studies of lineaments extraction from ASTER DEM, SRTM, and Cartosat for Jilledubanderu River basin, Anantapur district, AP, India by using remote sensing and GIS. *Data Brief* **20**, 1676–1682 (2018). <https://doi.org/10.1016/j.dib.2018.09.023>
- Nageswara Rao, K.: Analysis of surface runoff potential in ungauged basin using basin parameters and SCS-CN method. *Appl. Water Sci.* **10**(1), 1–16 (2020). <https://doi.org/10.1007/s13201-019-1129-z>
- Rawat, K.S., Singh, S.K.: Estimation of Surface Runoff from Semi-arid Ungauged Agricultural Watershed Using SCS-CN Method and Earth Observation Data Sets. *Water Conserv. Sci. Eng.* **1**(4), 233–247 (2017). <https://doi.org/10.1007/s41101-017-0016-4>
- Sakthivel, R., Jawahar Raj, N., Sivasankar, V., Akhila, P., Omine, K.: Geo-spatial technique-based approach on drainage morphometric analysis at Kalrayan Hills, Tamil Nadu, India. *Appl. Water Sci.* **9**(1), 1–18 (2019). <https://doi.org/10.1007/s13201-019-0899-7>
- Saravanan, S., Manjula, R.: Geomorphology based semi-distributed approach for modeling rainfall-runoff modeling using GIS. *Aquat. Procedia* **4**, 908–916 (2015). <https://doi.org/10.1016/j.aqpro.2015.02.114>
- Satheeshkumar, S., Venkateswaran, S., Kannan, R.: Rainfall–runoff estimation using SCS–CN and GIS approach in the Pappiredipatti watershed of the Vaniyar sub basin, South India. *Model. Earth Syst. Environ.* **3**(1), 1–8 (2017). <https://doi.org/10.1007/s40808-017-0301-4>
- Savita, R., Satishkumar, U., Mittal, h., Singh, P., and Yadav, K.: Analysis of hydrological inferences through morphometric analysis: a remote sensing-GIS based study of Kankanala reservoir subwatershed (2017)
- Schumm, S.A.: Evolution of drainage system and slopes in badlands at Perth Amboy, NEW Jersey. *Geol. Soc. Am. Bull.* **67**, 597–646 (1956). [https://doi.org/10.1130/0016-7606\(1956\)67\[597:EODSAS\]2.0.CO;2](https://doi.org/10.1130/0016-7606(1956)67[597:EODSAS]2.0.CO;2)
- Soni, S.: Assessment of morphometric characteristics of Chakrar watershed in Madhya Pradesh India using geospatial technique. *Appl. Water Sci.* **7**(5), 2089–2102 (2016). <https://doi.org/10.1007/s13201-016-0395-2>
- Soulis, K.X., and Valiantzas, J.D.: SCS-CN parameter determination using rainfall-runoff data in heterogeneous watersheds-the two-CN system approach. *Hydrol. Earth Syst. Sci.* **16**(3), 1001 (2012). <https://doi.org/10.5194/hess-16-1001-2012>
- USDA-SCS. National Engineering Handbook. Hydrology Section 4. Chapters 4–10. United States Department for Agriculture, Washington, D.C. (1972)
- Vincy, M.V., Rajan, B., Pradeepkumar, A.P.: Geographic information system–based morphometric characterization of sub-watersheds of Meenachil river basin, Kottayam district, Kerala. *India Geocarto Int.* **27**(8), 661–684 (2012). <https://doi.org/10.1080/10106049.2012.657694>
- Vinithra, R., Yeshodha, L.: Rainfall–runoff modelling using SCS–CN method: a case study of Krishnagiri District, Tamilnadu. *Int. J. Sci. Res.* **6**, 35–39 (2013)



# Numerical Modeling of Excavation in Shanghai Soft Clays Using the New Small Strain Shanghai Constitutive Model

Afnan Younis Tanoli<sup>(✉)</sup> and Guan-lin Ye

Department of Civil Engineering, State Key Laboratory of Ocean Engineering and Shanghai Key Laboratory for Digital Maintenance of Buildings and Infrastructure, Shanghai Jiao Tong University, Shanghai 200240, China  
{Afnan.tanoli, ygl}@sjtu.edu.cn

**Abstract.** Numerical simulations are employed to predict deep excavations' performance and the magnitude of the associated wall and ground displacements. Accurate prediction of these displacements is essential to prevent any distress or damage to the adjoining structures. A novel numerical approach is proposed in this paper to predict the wall and ground displacements related to deep excavations in Shanghai soft clays by using a new elastoplastic small strain constitutive model. The small strain Shanghai model incorporates the effects of small shear strain, elucidates both the clays' structure and mechanical properties, and describes the dilatancy characteristics and strain-softening in a three-dimensional state. A deep excavation case study in Shanghai soft clay is simulated on Plaxis 2D. The material parameters and the monitored values of displacements are obtained from the site. A user defined soil model of small strain Shanghai model is made in the form of Dynamic Link Library (.dll) file to be used in this analysis. A comparison of the monitored values of displacements is made with ground and wall displacements' simulated values. The effects of the excavation activity on the adjoining historical buildings are evaluated. The simulated results agree well with the monitored results. The comparison lays out a novel numerical approach for predicting the performance of deep excavation in Shanghai soft clays and the associated displacements by using a new constitutive model.

**Keywords:** Constitutive model · Deep excavation · Finite element analysis · Small strain · Soft clays

## 1 Introduction

To match the massive urban development over the past couple of years, various infrastructures in the form of high rise buildings and subway transportation have emerged, requiring deep excavation for underground space utilization, basements, and vehicle parking. These excavations are usually carried out in the proximity of existing infrastructure, the stability of which should be ensured [1]. Accurate prediction of the behavior of deep excavations and their associated displacements during the design phase is vital in

protecting the surrounding infrastructure. Many factors govern deep excavations' performance: soil conditions, diaphragm wall properties, support system, geometry, boundary conditions, dewatering, and the construction sequence [2]. These factors make the process of predicting the performance of deep excavation and magnitude of the associated displacements very complicated.

The most important factor associated with the design and construction of excavation supports is the local experience of the performance of similar excavations [3]. Numerous semi-empirical relations have been developed to assess the displacements linked with the excavations [2, 4–18]. These correlations helped researchers and engineers in understanding the behavior of excavations and in conducting finite element analysis (FEA). However, the number of excavations carried out in soft clays using these semi-empirical relations is limited as per a database of case studies of excavations developed by Ali and Khan [19].

Zhang, et al. [20] define Shanghai clays as soft clays exhibiting high sensitivity, high water content, high compressibility, and low bearing capacity. The soft clays exhibit special characteristics and pose numerous problematic issues while dealing with them. The application of the semi-empirical relations mentioned above to soft clays like Shanghai clay needs careful and thorough study, owing to their unique and problematic characteristics. Various researchers tried to investigate the behavior of deep excavations based on instrumentation methods in such soft clays [9, 13, 14, 21–27]. Also, 2D and 3D finite element analyses have been utilized in the prediction of the excavation behavior in Shanghai clays [28–31]. The constitutive models used in these analyses are Mohr-Coulomb, Cam-clay, or Modified Cam-clay model. The Cam-clay, Modified Cam-clay, and Mohr-Coulomb models do not incorporate the small strain effect, which is important to predict the maximum ground settlement [32]. Therefore, the use of these models in assessing the behavior of excavation in Shanghai clays requires additional care.

Various new elastoplastic and visco-plastic constitutive models have been proposed to describe the properties of Shanghai clays based on Cam-clay model [33, 34]. These models, however, do not incorporate the effects of small shear strain. Small strain Shanghai model is a new elastoplastic model that is based on the Cam-clay model and includes the impacts of small shear strain along with describing dilatancy characteristics and strain softening of overconsolidated clays [35–37]. Small strain Shanghai model is used in the FEA to predict the behavior of deep excavation activity in Shanghai clays because of its ability to incorporate small shear strains along with describing the strain-softening and dilatancy characteristics of soft clays.

This study focuses on proposing a new numerical approach to predict the behavior of excavation and the magnitude of associated displacements in Shanghai soft clays by using a new constitutive model. The project selected for this study is a high rise building in the Luwan District of Shanghai, PR China. Two important urban traffic roads, residential and historical buildings, and a church lie in this project's proximity. The monitored data of wall and ground displacements obtained from the instrumentation method is compared with the FEA results obtained from Plaxis 2D using a user defined soil model file of small strain Shanghai model. The impacts of displacements linked with the excavation activity on the surrounding historical buildings are investigated.

## 2 Overview of the Project

The location of the excavation site is at the intersection of Fuxing Middle Road and Chongqing South Road in the Luwan District of Shanghai, China. The building has a two-story basement and piled raft foundation. The area to be excavated is approximately 11000 m<sup>2</sup> and is in the shape of a long strip, with an excavation depth of about 10.70 m. The location of the project is shown in Fig. 1.

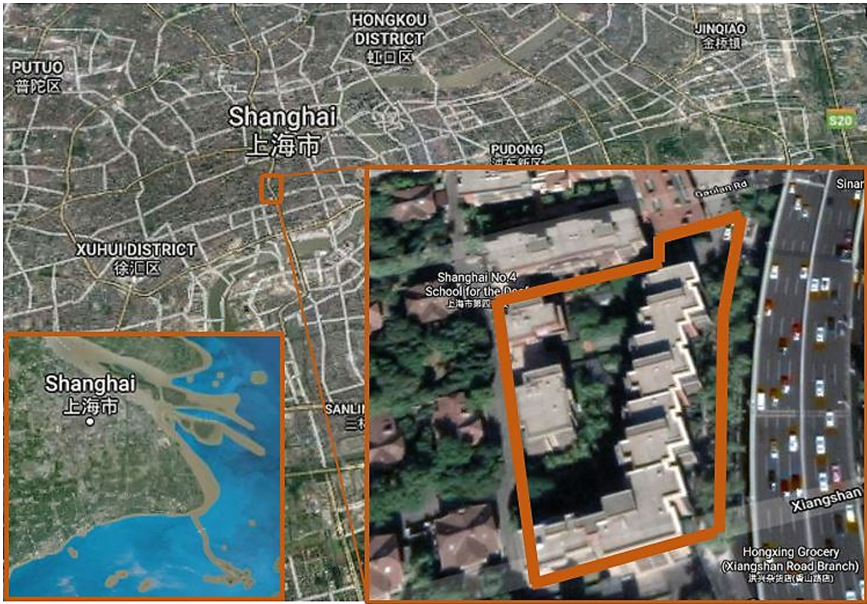
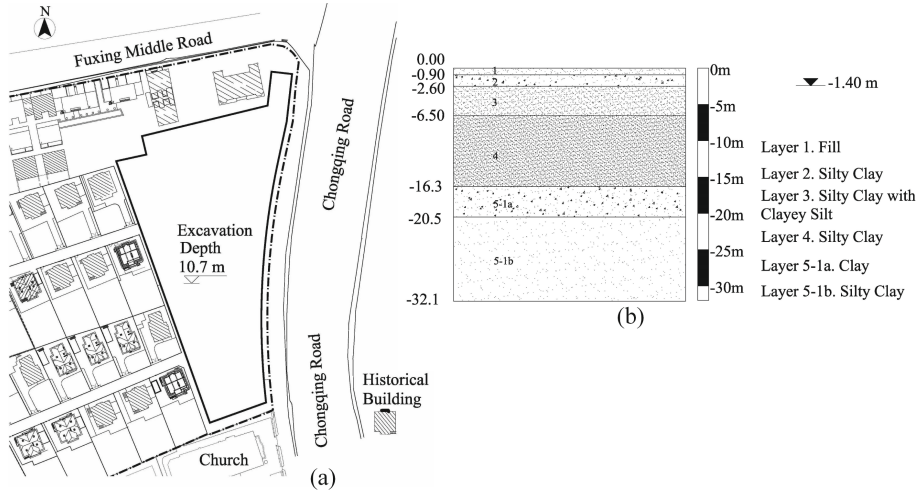


Fig. 1. Location of the project site

The project site is surrounded by a high urbanized traffic road, various municipal lines, a catholic church, and some historical buildings. The distance between the historical buildings and the foundation pit is between 3.7 to 5.6 m. The general plan of the project is shown in Fig. 2 (a). In summary, the environmental protection requirements around the foundation pit of this project are high. The historic buildings adjacent to the foundation pit are susceptible to settlement, the safety and stability of which is the key objective of this project. The surrounding sensitive environment also puts forward higher requirements for the design and deformation control of deep foundation pit projects.

As per the geological survey report, the topmost layer consists of yellow-grey soil fill. The second layer is of grey-yellow to brown, silty clay that is medium compressible, plastic, and iron oxide. The third layer consists of highly compressible silty clay and clayey silt. The upper part contains mica debris and cohesive silt. The fourth layer contains highly compressible silty clay with thin silt layer, occasional organic matter, and debris. The fifth layer has been divided into two sub-layers: 5-1a and 5-1b. The 5-1a layer contains soft plastic and highly compressible grey clay. The layer 5-1b contains plastic, medium compressible grey silty clay. The subsurface profile is shown in Fig. 2 (b).



**Fig. 2.** General site details: (a) General plan of the project; (b) Subsurface soil profile

## 2.1 Excavation Support System

To effectively control the foundation pit's deformation and reduce the impact on the adjacent historical buildings, an 800 mm thick reinforced concrete diaphragm wall is adopted for this project's enclosure. The depth of underground diaphragm wall is set at 13.5 m below the excavation base to enhance the stability against heaving and reduce the influence of the displacements on the adjacent buildings during the excavation activity.

The horizontal support system consists of two reinforced concrete parallel braced support systems: first support at a distance of 2.1 m and the second at 7.6 m from the top. Grouting is employed on the western side of the project to reinforce and ensure the diaphragm wall's stability during the construction and reduce horizontal displacement of the wall.

## 3 Soil Constitutive Model

Small strain Shanghai constitutive model is an elastoplastic model based on the original Shanghai model [35–37]. The small strain shanghai model describes the dilatancy and strain softening characteristics of OC clays under a 3D stress state [37] and incorporates small shear strain effects. The original Shanghai model is a modified version of Zhang's Model [33, 34, 38]. The Shanghai model is based on anisotropy [39], sub-loading surface [40] and super-loading surface [38, 39, 41, 42]. The model developed by Ye and Ye [34], incorporates dynamic loading and mechanical behavior of clays with varying drainage conditions. The Shanghai model is described below:

The yield surface is defined as:

$$f = \ln \frac{\hat{p}}{\hat{p}_o} + \ln \frac{M^2 - \xi^2 + \eta^{*2}}{M^2 - \xi^2} + \ln R^* - \ln R - \frac{\varepsilon_v^p}{C_p} = 0 \quad (1)$$

Where  $M$  defines the critical state stress ratio,  $\eta = q/p$  is the shear stress,  $\xi_o$  is anisotropy,  $R^*$  represents structure, and  $R$  represents over-consolidation,  $\varepsilon_v^p$  represent the volumetric strain, and  $C_p = (\lambda - \kappa)/(1 + e_0)$ . The yield surface is shown in Fig. 3.

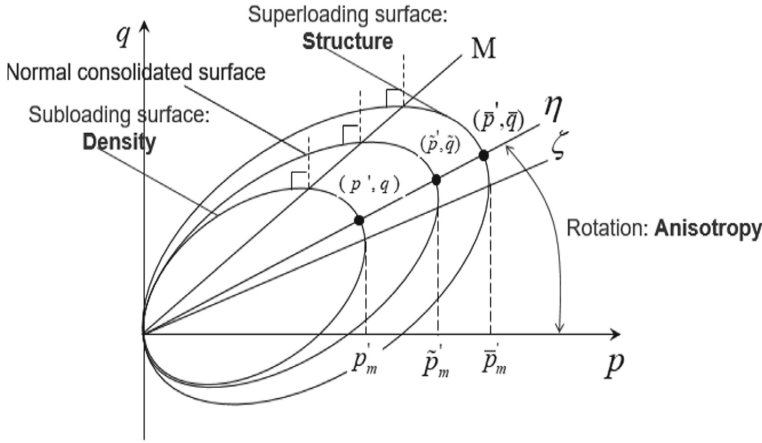


Fig. 3. Yield surface in p-q plane

New degree of structure evolution  $R^*$  for clay is:

$$\bar{R}^* = \frac{aM}{C_p} (1 - R^*) \sqrt{(1 - A) |d\varepsilon_v^p|^2 + A |d\varepsilon_s^p|^2} \tag{2}$$

$a$  controls the rate of structure collapse.

Evolution of the over-consolidation is:

$$\dot{R} = JU |D^p| + \frac{R}{MD} \frac{\eta}{M} \frac{\partial f}{\partial \beta} \cdot \beta \tag{3}$$

Where  $U$  is:

$$U = -\frac{mM}{C_p} \ln R \tag{4}$$

$m$  controls losing rate of over-consolidation.

The evolution of anisotropy is given as:

$$\dot{\beta} = \frac{J}{D} b_r (b_1 M - \zeta) \sqrt{\frac{2}{3}} |D_s^p| \frac{\dot{\eta}}{|\dot{\eta}|} \tag{5}$$

Where  $b_r$  controls developing rate of anisotropy.

The small strain Shanghai model incorporates small shear strain in the shear stiffness.

Cam-clay model defines shear stiffness as:

$$G = \frac{(1 - 2\nu)(1 + e_0)}{2(1 + \nu)} \frac{1}{k} p' \tag{6}$$

Where  $\nu$  represents Poisson ratio,  $k$  represents swelling index,  $e_0$  represents void ratio at reference pressure of 100 kPa, and  $p'$  represents mean effective stress.

The small strain Shanghai model defines shear stiffness by incorporating the equation of Dos Santos and Gomes Correia [43] as:

$$G = \frac{\left(\frac{7}{3} + 0.001/\gamma_{0.7}\right)^2}{\left(\frac{7}{3} + d/\gamma_{0.7}\right)^2} \frac{(1 - 2\nu)}{2(1 + \nu)} \frac{(1 + e_0)}{k} p' \tag{7}$$

The  $\gamma_{0.7}$  represents shear strain, the shear modulus  $G$  at which is decayed to 70% of the initial.

Out of the total ten parameters of small strain Shanghai model, five are the same as in Cam-clay model ( $M, N, \lambda, \kappa, \nu$ ), 3 are the controlling parameters ( $m, a$  and  $b_r$ ), three parameters are the initial state values ( $\xi_o, R,$  and  $R^*_o$ ), and the remaining two parameters are defined as:

- A: controls the shear strain ratio.
- $\gamma_{0.7}$ : controls small strain stiffness.

### 4 FEA Model and Mesh

A 2D FE model with medium mesh density is used to simulate the section AA' of the deep excavation case study on Plaxis 2D. Section AA' is shown in Fig. 4. Section AA' is chosen for the numerical simulation owing to the maximum settlement monitored along

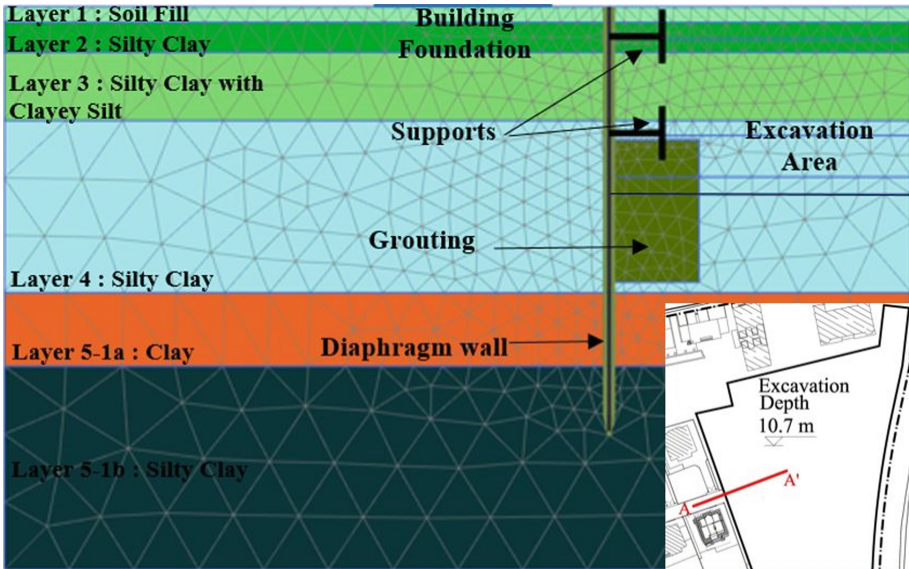


Fig. 4. Numerical model of section AA' and mesh details

this section at the site. The lateral extent of the soil mass boundary is set at three times the width of the excavation (3B) as per Fig. 5, and the bottom edge from the maximum excavation depth is set at 22 m to avoid boundary effects. The vertical boundaries of the model ( $X_{min}$  and  $X_{max}$ ) are constrained from horizontal deformation, the bottom boundary ( $Y_{min}$ ) is restrained from both horizontal and vertical deformation, and the top boundary ( $Y_{max}$ ) is set as free. The FE model and mesh details are provided in Fig. 4.

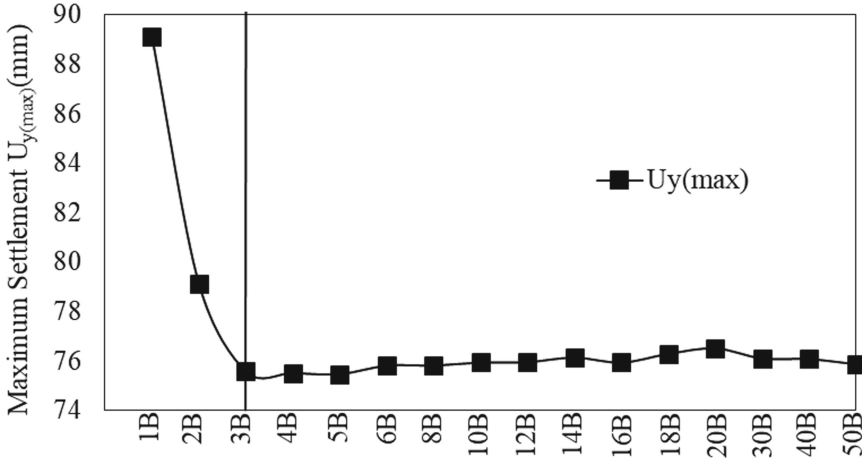


Fig. 5. Obtained maximum settlement with increasing model extents

### 5 Material Parameters

Small strain Shanghai model is used as the constitutive model in this FEA whose out of ten parameters, eight parameters are the same as used in the original Shanghai model proposed by Ye, et al. [33], Ye and Ye [34], Zhang, et al. [38]. The five parameters out of these eight parameters are the Cam-clay parameters ( $M_f$ ,  $\lambda$ ,  $\kappa$ ,  $e_0$  and  $\nu$ ), and the remaining three parameters ( $m$ ,  $a$ , and  $b_r$ ) are the controlling parameters that can be obtained from oedometer and triaxial tests. The three parameters are the initial state variables.

Stress induced anisotropy holds very less importance when dealing with clays, so initial anisotropy ( $\xi_o$ ) and parameter controlling the developing rate of stress induced anisotropy ( $b_r$ ) are assumed as zero. The other two initial values of  $R = 1/OCR$  and  $R^*_o = 1/Sensitivity$  are vital as they represent over consolidation and soil structure, respectively. Values of  $m$  and  $a$  are obtained by curve fitting of element test results. Initial states are obtained by simulating triaxial tests using  $m$  and  $a$ . Then, these initial states, along with  $m$  and  $a$ , are used to carry out a triaxial compression simulation to derive other parameters. A user defined material library file of small strain Shanghai model is developed to be used in this analysis on Plaxis 2D. The material properties used in the FEA are provided in Table 1.



**Table 1.** Material parameters used in the numerical analysis

Parameters	Symbols	Layer 1	Layer 2	Layer 3	Layer 4	Layer 5-1a	Layer 5-1b
Modulus	$E$ (MPa)	20	20	20	20	20	50
Unit weight	$\gamma$ (kN/m <sup>3</sup> )	18	18.8	17.8	16.7	17.4	19.3
Cohesion	$c$ (kPa)	0.0	–	–	–	–	–
Friction Angle	$\phi^\circ$	22	–	–	–	–	–
Void ratio	$e_0$	–	0.85	0.86	0.86	0.815	0.815
Poisson ratio	$\nu$	–	0.4	0.4	0.4	0.4	0.4
Slope of CSL	$M_f$	–	1.4	1.4	1.2	1.4	1.4
Compression index	$\lambda$	–	0.087	0.094	0.155	0.135	0.135
Swelling Index	$\kappa$	–	0.02	0.02	0.02	0.02	0.02
Controlling over-consolidation	$M_R$	–	1.0	0.2	0.2	2.0	2.0
Controlling structure	$a$	–	0.2	1	5.0	1.5	1.5
Controlling Anisotropy	$b_r$	–	0.0	0.0	0.0	0.0	0.0
Sand or Clay type	$I_{clay}$	–	2.0	2.0	2.0	2.0	2.0
Control. Shear Strain Ratio	$A$	–	0.5	0.5	0.1	0.5	0.5
Small Strain stiffness	$\gamma_{0.7}$ (%)	–	0.016	0.035	0.04	0.035	0.035
Initial OCR	$OCR$	–	5.5	1.0	1.2	1.3	1.3
Initial Structure	$R^*_0$	–	1.0	0.8	0.2	1.0	1.0
Initial anisotropy	$\xi_0$	–	0.0	0.0	0.0	0.0	0.0
Permeability	$K$ (cm/s)	2.0e–3	2.5e–6	3.0e–5	3.7e–7	2.0e–7	3.0e–6

## 6 Analysis and Results

The topmost layer of soil fill is modelled using the Mohr-Coulomb (MC) model, and the remaining soil layers (layer 2 to layer 5-1b) are modelled using small strain Shanghai model. The parameters of each model and material properties are provided in Table 1. The groundwater is set at 1.4 m from the top as per the actual site conditions.

The diaphragm wall is modelled as “plate” element present in the Plaxis library, while the grouting and footing concrete at the base of the excavation is modelled using the linear elastic material model. The foundation of the building is modelled as a “plate” element. The horizontal supports and the beams are modelled as “fixed-end anchor” elements.

The numerical simulation consists of six stages. The initial phase consists of determining the effective stresses and pore water pressures. The first stage consists of the construction of diaphragm wall and grouting. The second and third stages include the excavation of first and second soil sections and the installation of first and second horizontal support, respectively. Fourth stages include excavating the remaining soil section below the second support and placing footing concrete at the base. Fifth and sixth stages consist of replacing the second and first support with beams, respectively. The details of these stages are provided in Table 2. The simulated results are compared with the monitored values of displacement at the site.

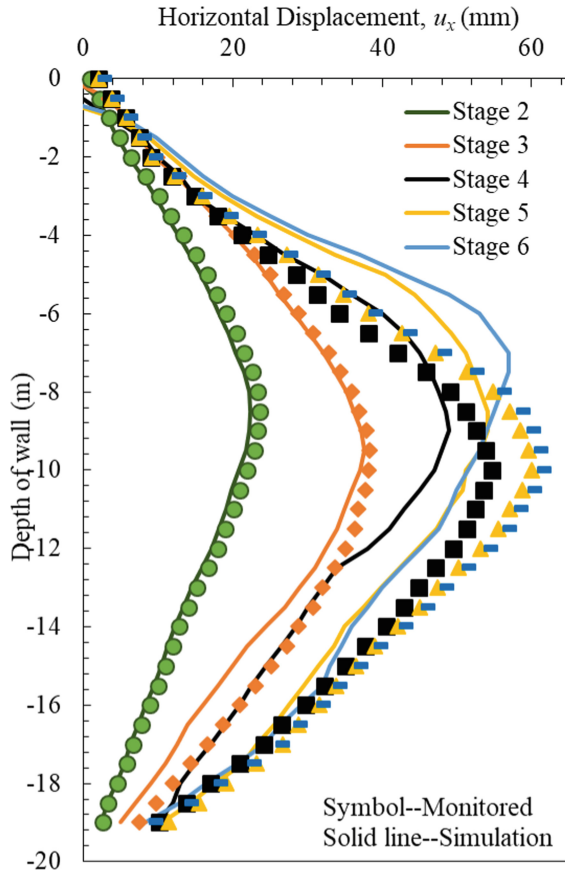
**Table 2.** Details of excavation stages

Stage	Days	Construction activity
Stage 1	57	The foundation load is placed, diaphragm wall and grouting are modelled
Stage 2	36	The first section of soil is excavated, and the first support is installed
Stage 3	19	The second soil section is excavated, and the second support is installed
Stage 4	32	The soil section below the second support is excavated, and floor concrete is poured
Stage 5	55	The second support is replaced with structural beam
Stage 6	63	The first support is replaced with structural beam

**6.1 Horizontal Displacement Along Diaphragm Wall**

The FEA results are compared with the maximum horizontal displacements measured at the site. The maximum horizontal wall displacement monitored at the site is 60.87 mm, while the maximum simulated wall displacement is 56.8 mm. The relative error is 6.10%. The comparison between the simulated and monitored values of wall displacement is presented in Fig. 6.

The simulated value of maximum wall displacement is 22.37 mm for stage 2, which is less than the monitored value of 23.55 mm. For excavation stage 3, the simulated value is 37.6 mm, while the monitored value is 38.36 mm. The maximum simulated horizontal displacements after excavation stages 4, 5, and 6 are 49.0 mm, 55.4mm, and 56.8 mm, respectively, while the monitored values are 54.68 mm, 60.02mm, and 60.87 mm, respectively. The maximum wall displacement locations obtained from the analysis lie above the monitored location for excavation of all the stages. The comparison between the simulated and monitored results is shown in Table 3 and Table 4. The maximum horizontal displacement ratio along the diaphragm wall obtained from the analysis to the maximum excavation depth is 0.54%.



**Fig. 6.** Comparison of simulated and monitored horizontal displacement along the diaphragm wall after each excavation stage

**Table 3.** Comparison between monitored and simulated values of wall displacements

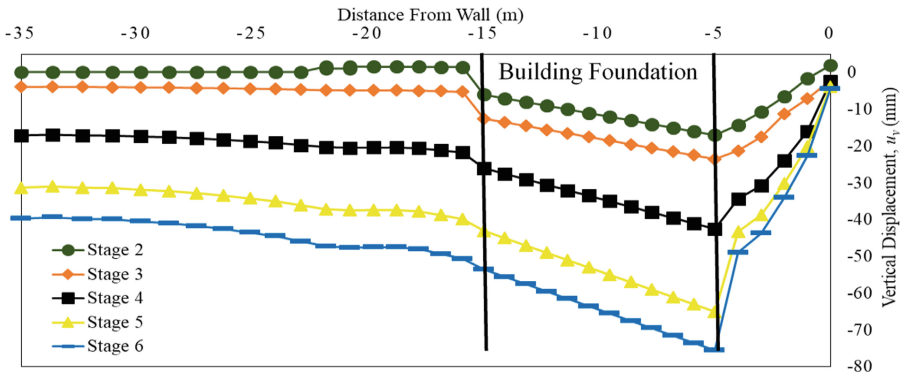
Stage	Monitored Maximum displacement (mm)	From FEA Maximum displacement (mm)
2	23.55	22.37
3	38.36	37.6
4	54.68	49.0
5	60.02	55.4
6	60.87	57.0

**Table 4.** Comparison between monitored and simulated distance of maximum displacement from the top of the wall

Stage	Monitored	From FEA
	Location of maximum displacement (m)	Location of maximum displacement (m)
2	8.5	8.5
3	9.5	9.0
4	10.0	9.0
5	10.0	8.3
6	10.0	7.5

### 6.2 Settlement in the Surrounding

Figure 7 shows the vertical displacement (settlement) curves obtained after every excavation stage, starting from the edge of the diaphragm wall to the horizontal extent ( $X_{min}$ ) of the model.  $X = 0$  represents the location of the diaphragm wall. The vertical displacement curves form a concave pattern with the maximum settlement occurring at the edge of the building near the excavation boundary. The sudden increase in the settlement under the edge of the building foundation is evident from Fig. 7. The settlement reduces linearly below the foundation, and a sudden decrease is noted after the foundation, after which the settlement gradually reduces.



**Fig. 7.** Vertical displacement profiles along the ground surface after each excavation stage

### 6.3 Effects on the Foundation of the Surrounding Historical Buildings

The vertical displacement values measured along the three points located on the foundation of an adjoining historical building are used for comparison between the simulated and monitored results. Three points are selected, which are F31, F32, and F33. F33 is

located on the edge of the foundation closer to the excavation boundary at a distance of 3.7 m. The point F32 lies in the center of the foundation and the point F31 lies at the far end of the foundation from the excavation boundary. Figure 8 shows the comparison between the simulated and monitored values of vertical displacement measured at these points along with the location of these points.

The maximum vertical displacement is measured at point F33 since it lies at the closer end to the boundary of excavation, where the displacement is maximum. The simulated vertical displacement values are comparable with the monitored values. It is observed from Fig. 8 that the simulated vertical displacement curve trend follows the same pattern as the trend of monitored vertical displacement values. From Fig. 7 and Fig. 8, it can be observed that the vertical displacement increases with the increase in excavation depth.

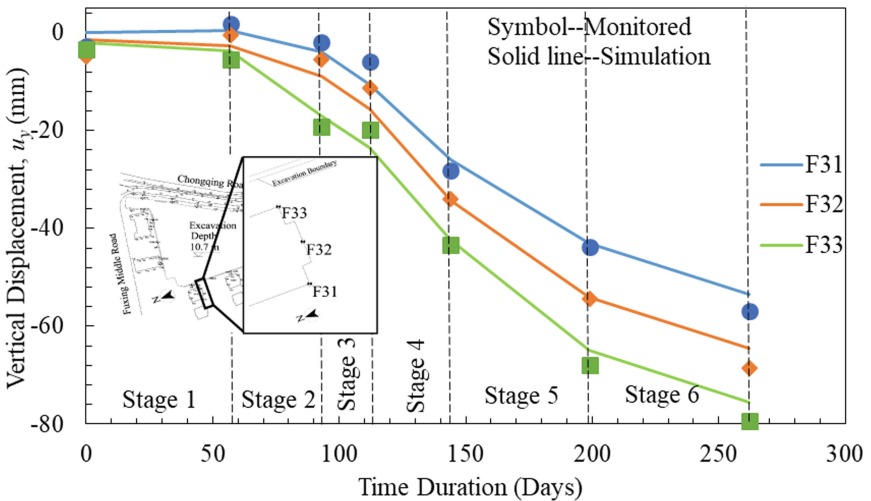


Fig. 8. Comparison of monitored and simulated vertical displacements along the building foundation

## 7 Conclusions

A FEA is carried out using the small strain Shanghai model and following the construction sequence adopted at the site of a deep excavation project in Shanghai. The horizontal displacements along the diaphragm wall, vertical surface displacements, and the effects of the excavation on the foundation of surrounding historical buildings are analysed and compared with the monitored values measured at the site using the instrumentation method. Both the horizontal wall displacements and vertical surface displacements increase with the increase in excavation depth. The comparison between the simulated and monitored results of displacements show that:

1. The maximum horizontal wall displacement observed at the site is 60.87 mm, while the maximum simulated wall displacement is 57.5 mm with a relative error is 5.50%.
2. The maximum wall deflection ratio obtained from the analysis to the maximum excavation depth is 0.54%, while the monitored ratio is 0.59%.
3. The maximum surface settlement obtained from the analysis is 75.1 mm, while the monitored value is 79.4, with a relative error of 5.4%.
4. The simulated location of the maximum and minimum settlement agrees well with the monitored location.
5. The comparison concludes that incorporating small shear strain in clays is very important in predicting deep excavation behavior in soft clays like Shanghai clay.

The study does not involve the effects of traffic surcharge and reinforced beam provided at the top of the wall on the wall's horizontal displacement, which is a future research prospect.

**Acknowledgement.** The financial support of the National Nature Science Foundation of China (Grant No. 42072317 and 41727802) is gratefully acknowledged.

## References

1. Mitew-Czajewska, M.: A study of displacements of structures in the vicinity of deep excavation. *Arch. Civ. Mech. Eng.* **19**(2), 547–556 (2018). <https://doi.org/10.1016/j.acme.2018.11.010>
2. Masuda, T.: Behavior of deep excavation with diaphragm wall. Massachusetts Institute of Technology (1993)
3. Wang, J., Xu, Z., Wang, W.: Wall and ground movements due to deep excavations in Shanghai soft soils. *J. Geotech. Geoenviron. Eng.* **136**(7), 985–994 (2010)
4. Burland, J.: Movements around excavations in London Clay. In: Proceedings of the 7th European Conference on Soil Mechanics and Foundation Engineering, vol. 1, pp. 13–19 (1979)
5. Carder, D.: Ground movements caused by different embedded retaining wall construction techniques, Trl Report, no. 172 (1995)
6. Clough, G.W.: Construction induced movements of in situ walls. In: Design and Performance of Earth Retaining Structures, pp. 439–470 (1990)
7. Fernie, R., Sucking, T.: Simplified approach for estimating lateral wall movement of embedded walls in UK ground. In: Geotechnical Aspects of Underground Construction in Soft Ground, pp. 131–136 (1996)
8. Goldberg, D.T., Jaworski, W.E., Gordon, M.D.: Lateral Support Systems and Underpinning. Volume 3: Construction Methods (1976)
9. Hsieh, P.-G., Ou, C.-Y.: Shape of ground surface settlement profiles caused by excavation. *Can. Geotech. J.* **35**(6), 1004–1017 (1998)
10. Leung, E.H., Ng, C.W.: Wall and ground movements associated with deep excavations supported by cast in situ wall in mixed ground conditions. *J. Geotech. Geoenviron. Eng.* **133**(2), 129–143 (2007)
11. Long, M.: Database for retaining wall and ground movements due to deep excavations. *J. Geotech. Geoenviron. Eng.* **127**(3), 203–224 (2001)

12. Mana, A.I., Clough, G.W.: Prediction of movements for braced cuts in clay. *J. Geotech. Geoenviron. Eng.* **107** (1981). No. ASCE 16312 Proceeding
13. Moormann, C.: Analysis of wall and ground movements due to deep excavations in soft soil based on a new worldwide database. *Soils Found.* **44**(1), 87–98 (2004)
14. Ou, C.-Y., Hsieh, P.-G., Chiou, D.-C.: Characteristics of ground surface settlement during excavation. *Can. Geotech. J.* **30**(5), 758–767 (1993)
15. Peck, R.B.: Deep excavations and tunneling in soft ground. In: 1969 Proceedings of the 7th ICSMFE, pp. 225–290 (1969)
16. Wong, I.H., Poh, T.Y., Chuah, H.L.: Performance of excavations for depressed expressway in Singapore. *J. Geotech. Geoenviron. Eng.* **123**(7), 617–625 (1997)
17. Wong, L., Patron, B.: Settlements induced by deep excavations in Taipei. In: Proceedings of the 11th Southeast Asian geotechnical conference, Singapore, pp. 787–791 (1993)
18. Yoo, C.: Behavior of braced and anchored walls in soils overlying rock. *J. Geotech. Geoenviron. Eng.* **127**(3), 225–233 (2001)
19. Ali, J., Khan, A.Q.: Behaviour of anchored pile wall excavations in clays. *Proc. Inst. Civ. Eng. Geotech. Eng.* **170**(6), 493–502 (2017)
20. Zhang, D., Zhou, Y., Phoon, K.-K., Huang, H.: Multivariate probability distribution of Shanghai clay properties. *Eng. Geol.* **273**, 105675 (2020)
21. Liu, B., Zhang, D.-W., Yang, C., Zhang, Q.-B.: Long-term performance of metro tunnels induced by adjacent large deep excavation and protective measures in Nanjing silty clay. *Tunn. Undergr. Space Technol.* **95**, 103147 (2020)
22. Liu, G.B., Jiang, R.J., Ng, C.W., Hong, Y.: Deformation characteristics of a 38 m deep excavation in soft clay. *Can. Geotech. J.* **48**(12), 1817–1828 (2011)
23. Ng, C.W.: Observed performance of multipropped excavation in stiff clay. *J. Geotech. Geoenviron. Eng.* **124**(9), 889–905 (1998)
24. Ng, C.W.W., Hong, Y., Liu, G., Liu, T.: Ground deformations and soil–structure interaction of a multi-propped excavation in Shanghai soft clays. *Géotechnique* **62**(10), 907–921 (2012)
25. Tan, Y., Li, M.: Measured performance of a 26 m deep top-down excavation in downtown Shanghai. *Can. Geotech. J.* **48**(5), 704–719 (2011)
26. Tan, Y., Wei, B.: Observed behaviors of a long and deep excavation constructed by cut-and-cover technique in Shanghai soft clay. *J. Geotech. Geoenviron. Eng.* **138**(1), 69–88 (2012)
27. Wang, Z.W., Ng, C.W., Liu, G.B.: Characteristics of wall deflections and ground surface settlements in Shanghai. *Can. Geotech. J.* **42**(5), 1243–1254 (2005)
28. Hou, Y., Wang, J., Zhang, L.: Finite-element modeling of a complex deep excavation in Shanghai. *Acta Geotech.* **4**(1), 7–16 (2009)
29. Hu, Z., Yue, Z., Zhou, J., Tham, L.: Design and construction of a deep excavation in soft soils adjacent to the Shanghai Metro tunnels. *Can. Geotech. J.* **40**(5), 933–948 (2003)
30. Huang, X., Schweiger, H.F., Huang, H.: Influence of deep excavations on nearby existing tunnels. *Int. J. Geomech.* **13**(2), 170–180 (2013)
31. Zheng, G., Wei, S.-W.: Numerical analyses of influence of overlying pit excavation on existing tunnels. *J. Cent. South Univ. Technol.* **15**(2), 69–75 (2008)
32. Ali, J.: Excavation support practices in Pakistan, NUST (2016)
33. Ye, B., Ni, X., Huang, Y., Zhang, F.: Unified modeling of soil behaviors before/after flow liquefaction. *Comput. Geotech.* **102**, 125–135 (2018)
34. Ye, G.-L., Ye, B.: Investigation of the overconsolidation and structural behavior of Shanghai clays by element testing and constitutive modeling. *Undergr. Space* **1**(1), 62–77 (2016)
35. Zhang, S., Liao, C., Zhang, Q., Zhen, L.: Elastoplastic model for soils considering structure and overconsolidation. *J. Shanghai Jiaotong Univ. (Sci.)* **24**(2), 196–203 (2019)
36. Zhang, S., Ye, G., Liao, C., Wang, J.: Elasto-plastic model of structured marine clay under general loading conditions. *Appl. Ocean Res.* **76**, 211–220 (2018)

37. Zhang, S., Ye, G., Wang, J.: Elastoplastic model for overconsolidated clays with focus on volume change under general loading conditions. *Int. J. Geomech.* **18**(3), 04018005 (2018)
38. Zhang, F., Ye, B., Ye, G.: Unified description of sand behavior. *Front. Archit. Civ. Eng. China* **5**(2), 121–150 (2011)
39. Zhang, F., Ye, B., Noda, T., Nakano, M., Nakai, K.: Explanation of cyclic mobility of soils: approach by stress-induced anisotropy. *Soils Found.* **47**(4), 635–648 (2007)
40. Hashiguchi, K.: Elastoplastic constitutive laws of granular materials. In: *Constitutive Equations of Soils (Proceedings of the 9th ICFSME, Spec. Session 9)*, pp. 73–82 (1977)
41. Asaoka, A., Nakano, M., Noda, T.: Super loading yield surface concept for the saturated structured soils. In: Cividini, A. (ed.) *Application of Numerical Methods to Geotechnical Problems*. ICMS, vol. 397, pp. 233–242. Springer, Vienna (1998). [https://doi.org/10.1007/978-3-7091-2512-0\\_22](https://doi.org/10.1007/978-3-7091-2512-0_22)
42. Ye, B., Muramatsu, D., Ye, G., Zhang, F.: Numerical assessment of vibration damping effect of soilbags. *Geosynth. Int.* **18**(4), 159–168 (2011)
43. Dos Santos, J. Gomes Correia, A.: Reference threshold strain of soil. Its application to obtain an unique strain-dependent shear modulus curve for soil. In: *International Conference on Soil Mechanics and Geotechnical Engineering*, pp. 267–270 (2001)





# Computational Studies of Passive Vortex Generators for Flow Control on High-Speed Train

Aqib Aziz<sup>1</sup>(✉), Yang Zhang<sup>2</sup>, and Chen Gang<sup>2</sup>

<sup>1</sup> Aerospace Engineering, State Key Laboratory for Strength and Vibration of Mechanical Structures, Xi'an Jiaotong University, Xi'an 710049, China  
aqibaziz11@stu.xjtu.edu.cn

<sup>2</sup> State Key Laboratory for Strength and Vibration of Mechanical Structures, Xi'an Jiaotong University, Xi'an 710049, China

**Abstract.** Flow separation is one of the major causes of increase in aerodynamic drag. Vortex generators (VGs) are commonly used on cars and aircrafts to energize the boundary layer of the vehicle by mixing the high momentum flow from top to low momentum flow near the surface. This phenomena keeps the flow attached and delay flow separation, equivalently, the capability of flow to endure the adverse pressure gradient is enhanced. Vortex generators themselves add drag also in the form of viscous drag, but the overall effect of installing VGs is beneficial. Proper design of vortex generators plays a vital role in order to get maximum beneficial results. In present work, a very long high-speed train (204 m) is given herein to demonstrate flow control effect of vortex generators (VGs). Numerical studies are given via varying the configurations, size and orientations of VGs. The model selected for analysis is very similar to Chinese Railway High speed trains (CRH trains) having viscous drag as predominant drag and comparatively less contribution of pressure drag. Triangular, rectangular and trapezoidal shapes of VGs in co-rotating and counter rotating configurations are analyzed in present research. After the investigation of parameters of VGs on train model under analysis, it is found that the best shape and arrangement of VGs is triangular co-rotating VGs present at zero degree angle to each other. Triangular co-rotating VGs successfully reduced pressure drag of train model as much as 16.11% and increased viscous drag of train model by 0.055%. Change in total drag of the present train model is 1.03% drag reduction by installing 4 pairs of triangular co-rotating VGs. This reduction of total aerodynamic drag by 1.03% is very crucial, as it corresponds to millions of Kilowatt-hours (KWh) of electrical energy saving every year in high speed trains.

**Keywords:** Aerodynamic drag · Flow separation · Boundary layer · Vortex generators · Passenger-km

## 1 Introduction

Importance of high speed trains is increasing with time and electricity consumption is one of the major concerns for their progress. Increase in size and speed of the train

requires work on drag reduction. For example, Chinese Railway High speed train (CRH train) classes covered 1,452.9 billion passenger-kilometers in 2019 and the electricity consumption of 3.8 Kilowatt-hours (KWh) per 100 passenger-kilometers was needed. Although for long high speed trains, viscous drag is predominant drag, but still work is needed to be done to reduce pressure drag to a minimum level due to the enormous energy requirement.

Function of VGs is to reduce overall drag of the train by significantly reducing pressure drag. Vortex generators function by producing stream wise vortices just before the separation point, which supply high momentum of upstream flow to the downstream flow with low momentum [1]. The Shape and size of vortex generators must be optimized in order to obtain best result. Previous work on vortex generators identify the importance of optimized size and shape [2]. Reduction of drag by passive flow control, using vortex generators is not new. Lots of work has already been done on vortex generators of various sizes and shapes. Previous work review in this field can be found from the contributions of Lin et al. [3] and Rao and Kariya [4].

Some important guidelines have been established by Pearcey [5] for conventional vortex generators. Although the effect of vortices induced by VGs lasts up to 100 times of height of VGs (100 h), low profile VGs have most effective range of 5 h–30 h upstream of separation point of baseline model. VGs work to shift the separation point at the rear end of train to further downstream which will reduce the size of the vortices formed at separation point. This will result in reduction of aerodynamic drag. Proper design of the vortex generators is very important in order to get maximum beneficial effect. The shape, size, configuration, spacing and number of vortex generators depend on type of flow on the vehicle and the problem under analysis. VG parameters vary for different flows on different bodies.

VGs are used to change the dynamics of boundary layer flow. Work is done on study of these changes in boundary layer dynamics due to the vortices introduced by using VGs. Shabaka et al. [6] and Mehta and Bradshaw [7] studied the dynamics of vortices. Studies of turbulent boundary layer have been conducted mostly by direct numerical simulations [8, 9] and experimental work is also done. Pinelli [10] and Orlandi and Jimenez [9] also used direct numerical simulations to tell about the role of stream wise vortices in flow near the surface of boundary layer. Lin et al. [3] used experimental study to confirm that these stream wise vortices causes increase in skin friction and also transfer momentum towards the wall.

The purpose of current research is to design the best possible arrangement and shape of the vortex generators (VGs) for the train model under analysis. The force coefficients being considered for analysis are viscous drag coefficient, pressure drag coefficient and total drag coefficient of high speed train, with and without VGs. VGs reduce pressure drag and increase viscous drag, giving an overall beneficial effect of reducing total drag coefficient of present train model under analysis.

## 2 Background

In past, vortex generators have been used in order to enhance heat transfer, in addition to reducing total drag of the vehicles. New methods are developed to enhance heat transfer

in which fin surface flow is replaced by main flow longitudinal vortices, by installing VGs on surface of the body [11]. Torii and Yanagihara [12] studied the influence of using triangular VGs on laminar boundary layer. Yanagihara and Torii [13] also studied changes in laminar boundary layer for different shapes (rectangular and triangular) of VGs and concluded that triangular VGs with high angle of attack and large frontal area give the best performance in enhancing heat transfer. Use of VGs is not limited to just vehicles. VGs are also used in wind turbines. VGs are used on large horizontal axis wind turbines, which show non-linear and unsteady behavior, in order to reduce periodic loads so that fatigue life and power output of the wind turbines can be improved [14].

VGs have also been installed on transonic profiles to delay flow separation. Ashill et al. [15] showed through experimental and conceptual study that sub-boundary layer vortex generators (SBVG) successfully delayed shock induced flow separation. In airplanes, VGs have been found to be of great success. They are used to increase lift in airplanes. Gao et al. [16] did work on 30% thick DU97-W-300 airfoil, and found that the maximum value of lift coefficient was significantly increased. This happened because of the attachment of flow caused by VGs. More work is being done on passive flow control devices as compared to active flow control devices. It is because of the fact that active flow control devices need a source of energy and cannot work without that source unlike VGs and other passive flow control devices. Active flow control devices also need complex algorithms for getting maximum beneficial results [17]. Investigations show that VGs have been a success in decreasing aeroacoustics noise also [18]. Based on the history of VGs usage, the current research is carried out in order to reduce the aerodynamic drag of high speed train so that fuel consumption can be improved and energy can be saved.

### 3 Model Description

The present model of high speed train is similar to some of the longest high speed trains present. It has a length of 204 m, and a height of 3 m. CFD analysis shows that this train model consists of 93.1% viscous drag and 6.9% pressure drag and these two drags add to make total drag of the train model. Pressure drag coefficient for present model is 0.011 and viscous drag coefficient is 0.149, which makes a total drag coefficient of 0.16. The boundary layer thickness of the train under analysis is 0.7 m at VGs location. Vortex generators are installed on train model 11 m from the tail end. Figure 1 shows the train model used for analysis.

Research by Rao and Kariya [4] suggested that submerged vortex generators having height of less than 62.5% of boundary layer thickness can perform better than the vortex generators with height equal to boundary layer thickness because with larger heights, viscous drag added by vortex generators is more. Addition of viscous drag due to vortex generators has been an issue due to which the size of the vortex generator has decreased from boundary layer thickness height to just a portion of it. Compromise has to be made between decrease in pressure drag and increase in viscous drag due to vortex generators. Present analysis is based on vortex generator height of 10% to 60% of boundary layer thickness of train model. Location of installation of vortex generators is also an important

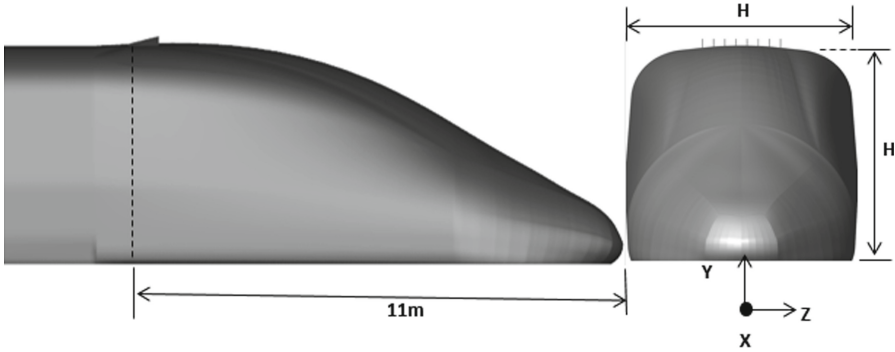


Fig. 1. Train model under analysis

factor to be considered. Different configurations of VGs were analyzed but only co-rotating VGs were able to reduce drag significantly. The three shapes of co-rotating vortex generators used for present research are given in the Fig. 2.

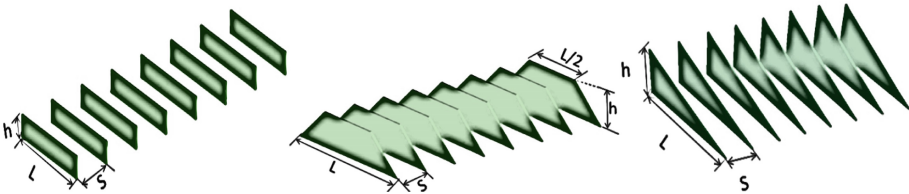
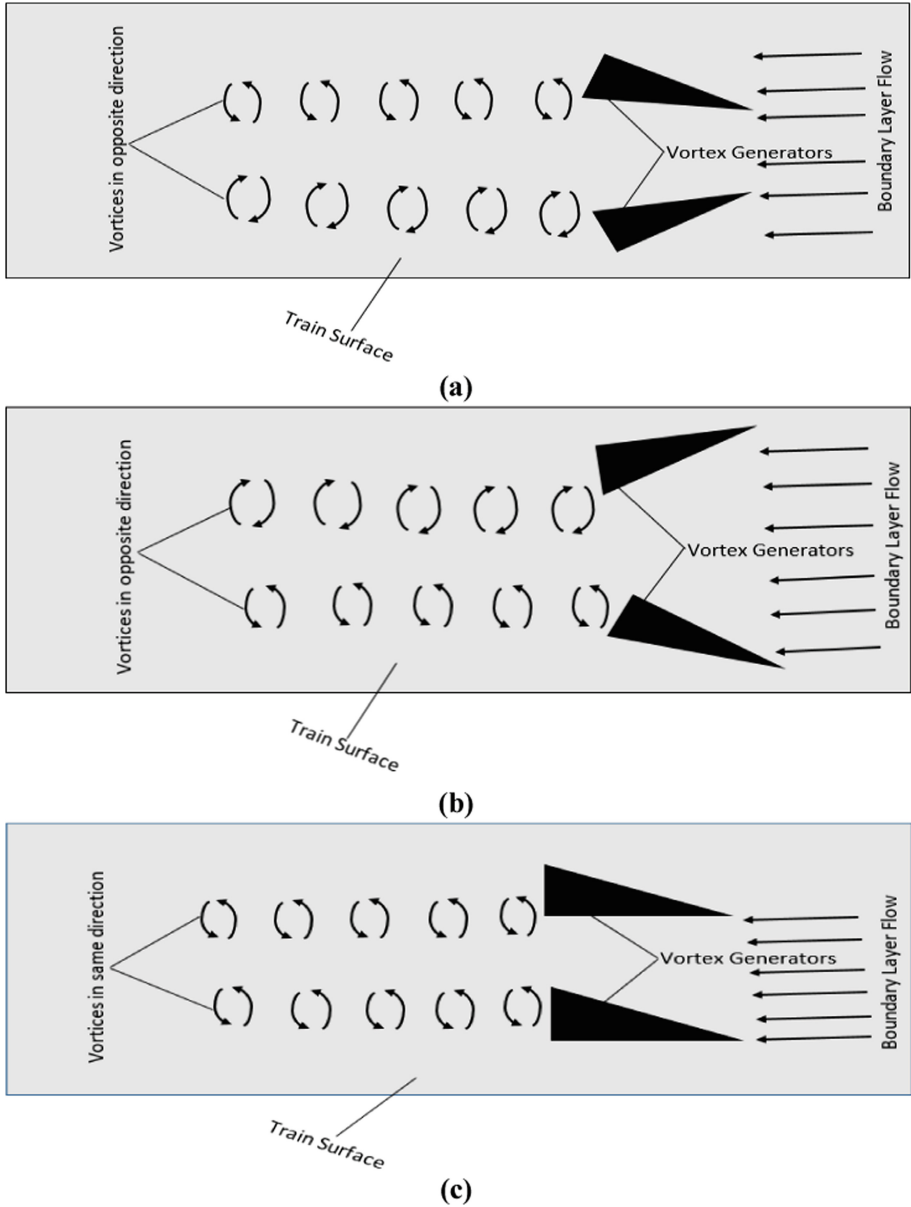


Fig. 2. VG configurations used for analysis

Submerged type of vortex generators are the focus of present research. These vortex generators are always present inside the boundary layer, having height equal to or less than the boundary layer thickness ( $\delta$ ). The size of vortex generators change with change in boundary layer thickness. It is expected from this type of vortex generators to produce less parasitic drag as compared to conventional vane type VGs which energize the flow by drawing energy from external flow. Lots of work has been done on such submerged vortex generators and different shapes and sizes of such vortex generators have been proposed.

VGs work by simply introducing changes in the boundary layer at the position where they are installed. They create vortices inside the boundary layer and transfer the momentum from high momentum flow at top to the low momentum flow at bottom. This momentum transfer in the flow energizes the boundary layer due to which the flow remains attached to the surface for a longer time and separation point is moved further downstream. In other words, this mixing of high momentum and low momentum flow balances the pressure gradient, which causes reduction in the opposing forces and flow gets attached to the surface [19]. This causes recovery in static pressure and also reduces total pressure loss. Counter-rotating VGs are those which are present at an angle to the flow and produce vortices in opposite directions whereas co-rotating VGs produce

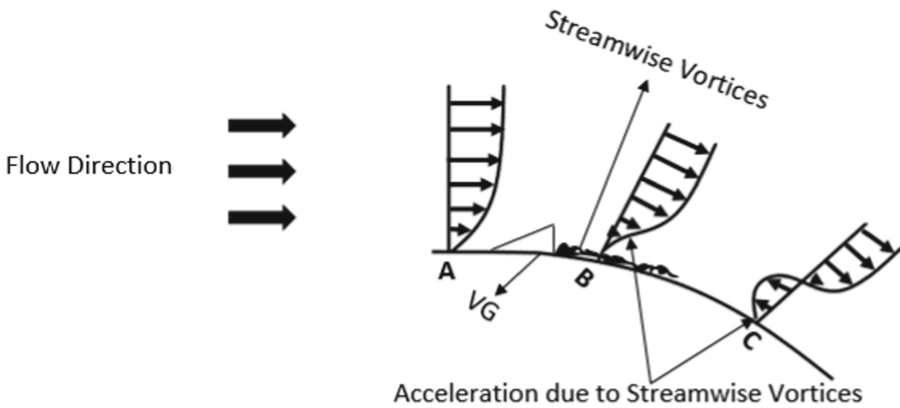
vortices in one direction. Purpose of both of these configurations is to energize the boundary layer and reduce aerodynamic drag. Production of vortices by counter-rotating and co-rotating VGs is demonstrated in Fig. 3.



**Fig. 3.** Vortex generations in VGs (a) Divergent VGs (b) Convergent VGs (c) Co-rotating VGs

Flow separation occurs when flow has low energy and energizing the flow by using VGs cause it to get attached to the surface for a longer time due to which the separation point of flow is shifted downstream. Vortex generators cause a rapid increase in pressure which reduces drag.

Working of VGs can be observed from Fig. 4. Flow is in one direction before approaching VGs but after that, the VGs produce turbulence in the flow causing the velocity of particles near surface to swirl and change direction. This causes the particles of flow to accelerate and get attached to the surface. This attachment of the particles to the surface causes the viscous drag between flow particles and surface to increase whereas pressure drag is decreased due to recovery of static pressure and reduction of loss in total pressure.

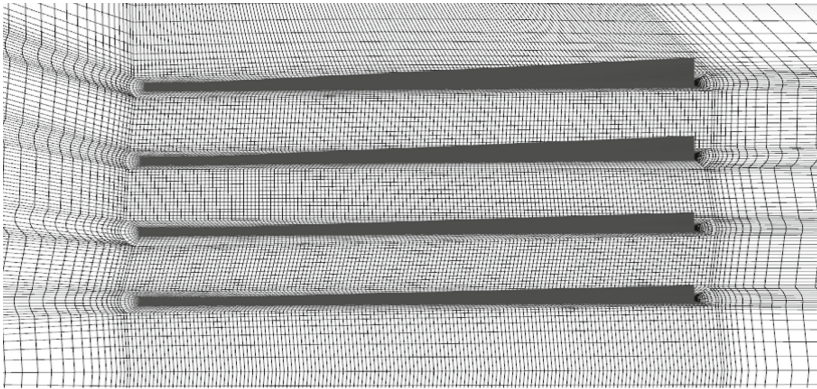


**Fig. 4.** Boundary layer changes by VGs

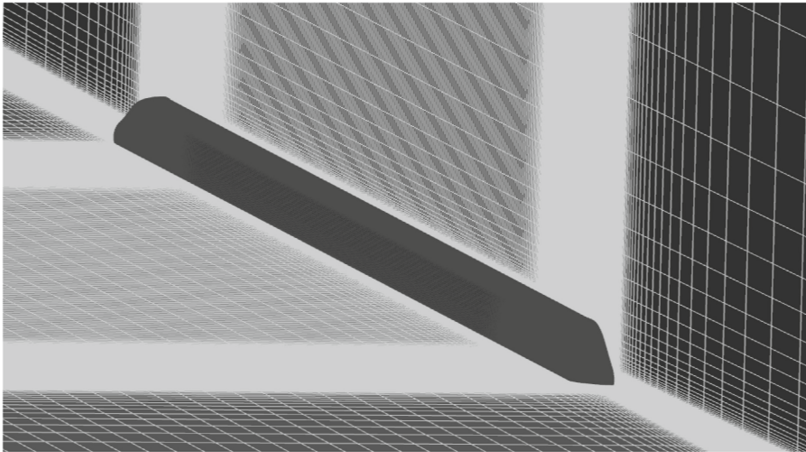
## 4 Numerical Scheme

The Reynolds-Averaged Navier-Stokes (RANS) equations were considered as the evaluated tool in present paper. RANS equations are time-averaged equations of motion for a fluid flow. These equations are based on Reynolds decomposition in which an instantaneous quantity is divided into a time-averaged quantity and a fluctuating quantity. These equations are used for solving turbulent flows as encountered in present research. These are not exact equations but modified and time-averaged equations, so they have some extra variables. These equations need turbulence models to get the solution. The detailed formulations about RANS will not be repeated here. Regarding the turbulence model, several turbulence models, such as K-Epsilon ( $k-\epsilon$ ) [20], K-Omega ( $k-\omega$ ) [21] and Spalart-Allmaras models [22] are involved in the fluent solver, which are the workhorse of present study. Then two equation model,  $k-\omega$  shear-stress model, developed by Menter [21], is chosen for this computational study ultimately. Shear stress transport  $k-\omega$  model combine the robustness of  $k-\omega$  near walls and also great capabilities of  $k-\epsilon$  away from walls.

Grid independence is investigated by making coarse, medium and fine meshes with around 15 million, 23 million and 35 million cells and it is made sure that the effect of mesh changes on results is negligible for final mesh selected. Finally a very fine structured hexahedral mesh having 35 million cells is selected as the final mesh for analysis purpose. First wall distance for whole mesh is 0.002 mm with growth rate of 1.2. Mesh is made even finer near vortex generators by having growth rate of 1.1 around VGs. Smooth transition is made for mesh moving away from the VGs location in all directions. Meshing is done by making separate O-grids on VGs and train model under analysis, so that precise results can be obtained. Figure 5 shows views of the mesh used for analysis purpose.



(a)



(b)

**Fig. 5.** Mesh views (a) Mesh around VGs (b) Mesh around complete train model

Boundary conditions used for the analysis of present train model are according to the working conditions of one of the fastest CRH high speed trains, when it moves at

its top speed. Density based solver is used for analysis showing that the flow under consideration is of compressible nature. As flow is considered compressible, so it is always preferable to use pressure far field boundary conditions at inlet and outlet of the domain with Mach number of 0.326. Bottom wall is set as slip wall moving at velocity of 111.1 m/s, showing top speed working conditions of the train model under analysis. Constant velocity is given in boundary conditions in order to avoid fluctuations due to velocity changes in boundary conditions. Symmetry boundary condition is given to the symmetry dividing the train model longitudinally into half because the other side of train model is mirror symmetry. The right side (observed from inlet) and top side of the far field domain are also given symmetry boundary conditions because these sides encounter same flow. Train and VGs are treated as stationary wall. Size of the far field can be checked from Fig. 6.

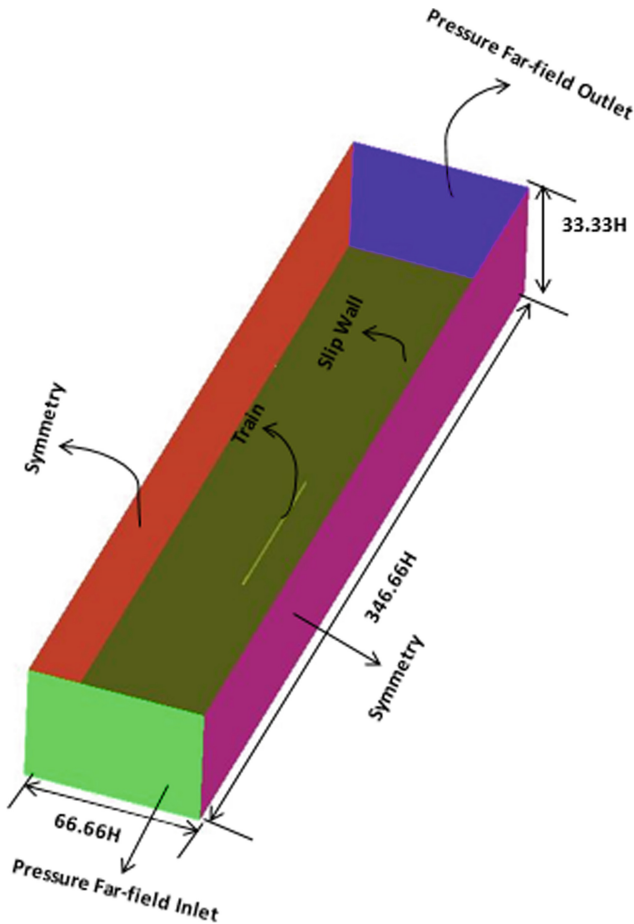


Fig. 6. Boundary conditions on flow domain



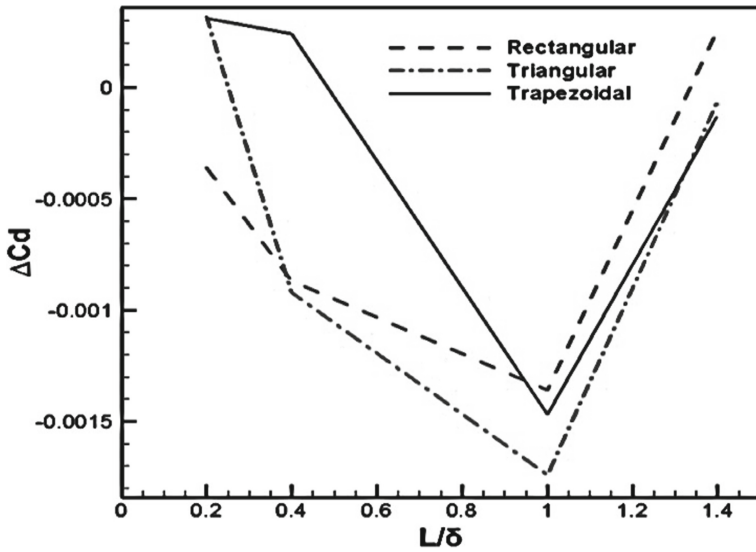
## 5 Results and Discussion

Both counter-rotating and co-rotating configurations of VGs are tested in order to get the best possible results. It is found that counter-rotating VGs both in convergent and divergent configurations do not work very well in drag reduction but co-rotating VGs placed parallel to the flow are able to reduce pressure drag significantly. Three different shapes of co-rotating VGs are analyzed and parameterization of size is also done for best results. Spacing for VGs is set as  $0.2\delta$  (20% of boundary layer thickness of train model). The results of all cases can be observed from Fig. 7. For VG length change investigation, a height of  $0.2\delta$  is fixed and for height change analysis, length equal to boundary layer thickness of train model ( $\delta$ ) at VGs location is used for analysis. VG spacing was same for all cases.

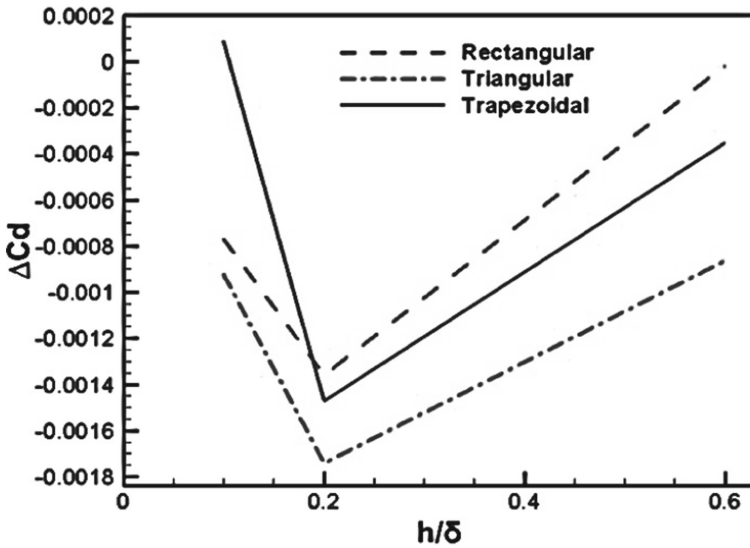
VGs perform best at a particular height and length. Location of VGs also matters a lot. Details of changes in pressure drag coefficient, viscous drag coefficient and total drag coefficient of train model by addition of VGs can be checked from Table 1. Here  $h/\delta$  and  $L/\delta$  are non-dimensional height and length of VGs shown as a portion of boundary layer thickness ( $\delta$ ) of the train model at VGs location.  $\Delta C_{dp}$  represents change in pressure drag coefficient of train model,  $\Delta C_{dv}$  shows change in viscous drag coefficient of train model and  $\Delta C_d$  shows change in total aerodynamic drag coefficient of present train model respectively, after installation of VGs on train model.

Many sizes and shapes of VGs are tested using RANS equation and simulations are performed to get results. The results show that increase in length of VGs make the vortices stronger and reduces more drag but after a particular length, the impact of these vortices starts to shade away and their effectiveness in reducing drag becomes lower. Same is the case with height. VGs perform best at a particular height and increasing or decreasing the height can make vortices less impactful and reduce VGs effectiveness. Results show that all three configurations of VGs are able to reduce aerodynamic drag but triangular VGs are the best for present train model reducing 1.03% of total drag of train model. Trapezoidal VGs have also shown good results by reducing 0.92% of total drag and rectangular VGs reduced drag by 0.85% of train model under analysis. The trends in change of drag coefficients with all three configurations are not much different but values of these drag coefficients are different for different configurations. Length of value equal to boundary layer thickness ( $\delta$ ) and height having value of 20% of boundary layer thickness ( $0.2\delta$ ) have shown the best results out of all the performed cases.

Comparison of pressure coefficients can be used as a criteria to judge the effectiveness of VGs. The purpose of VGs is to cause an increase in pressure coefficient. Comparison of the pressure coefficients at different locations after flow has passed VGs has been made. These contours show pressure coefficient distribution at top and bottom surface of the train model under analysis.



(a)



(b)

Fig. 7. Drag coefficient changes (a) with VG length (b) with VG height

Figure 8 is the distribution of pressure coefficients against non-dimensional z-coordinate ( $z/H$ ) of train model at different locations after the flow has passed VGs. VGs are installed at  $x/H = 64.33$ . Comparing the pressure coefficient distribution just after VGs installation location at  $x/H = 64.66$ , it can be noticed that the pressure coefficient curve has moved to lower values, showing decrease in static pressure just after

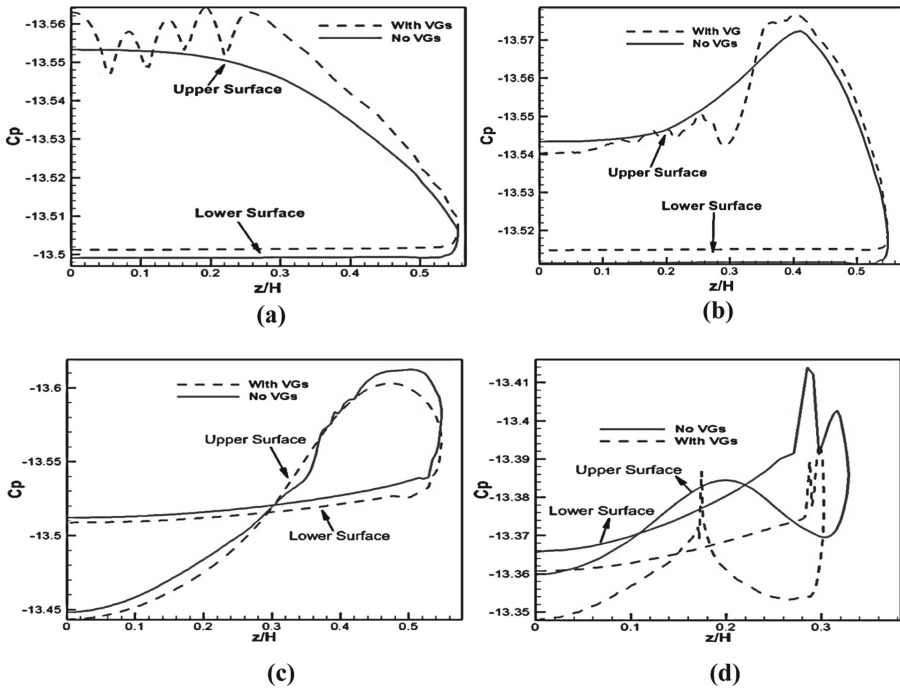
**Table 1.** Percentage change in drag coefficients with length and height of VGs

Shape	$h/\delta$	$L/\delta$	$\Delta C_{dp}$	$\Delta C_{dv}$	$\Delta C_d$	
Rectangular	0.2	0.2	-3.28%	+0.01%	-0.22%	
		0.4	-8.28%	+0.02%	-0.54%	
		1	-13.1%	+0.07%	-0.85%	
		1.4	+ 1.1%	+0.09%	+0.16%	
	0.1	1	-7.4%	+0.031%	-0.48%	
		0.2	-13.1%	+0.07%	-0.85%	
		0.6		-4.27%	+0.21	-0.084%
Triangular	0.2	0.2	+ 2.85%	+0.014%	+0.2%	
		0.4	-8.63%	+0.03%	-0.57%	
		1	-16.11%	+0.055%	-1.03%	
		1.4	-1.5%	+0.061%	-0.041%	
	0.1	1	-8.58%	+0.023%	-0.57%	
		0.2	-16.11%	+0.055%	-1.03%	
		0.6		-10.1%	+0.16%	-0.54%
Trapezoidal	0.2	0.2	-0.72%	+0.039%	+0.29%	
		0.4	-1.9%	+0.022%	+0.15%	
		1	-14.45%	+0.076%	-0.92%	
		1.4	-2.54%	+0.097%	-0.08%	
	0.1	1	-0.26%	+0.038%	+0.056%	
		0.2	-14.45%	+0.076%	-0.92%	
		0.6		-5.75%	+0.171%	-0.22%

the VGs. This curve shows that low pressure region is created just after the VGs. This low pressure region increase drag. Here  $x/H$  and  $z/H$  are non-dimensional distances in  $x$ -direction and  $z$ -direction of the train model with respect to the reference height of the train model (3 m).

Curves for pressure coefficients further away from the VGs at  $x/H = 66$  and at  $x/H = 66.66$ , illustrate the fact that pressure coefficients are increasing due to the presence of vortex generators. This is a positive effect for delaying flow separation. At  $x/H = 67.66$ , near tail end, it can be observed that there is a significant increase in pressure coefficients at that region. This increase in pressure coefficients show reattachment of the flow which delays the flow separation, hence drag decreases. Increase in static pressure at the rear end causes back pressure to increase thus it gives benefits of narrowing separation region and also increase flow pressure at separation [23, 24]. The increase in drag due to low pressure region just after VGs is compensated by more increase in static pressure region near point of separation and hence the overall drag due to VGs is reduced and overall effect is beneficial.

The values of pressure coefficients are shown negative here because zero Pascal pressure is set at inlet and outlet whereas reference pressure is set as 101325 Pa.



**Fig. 8.** Pressure distribution at different locations (a)  $x/H = 64.66$  (b)  $x/H = 66$  (c)  $x/H = 66.66$  (d)  $x/H = 67.66$

## 6 Conclusion

Vortex generators kept in co-rotating configuration at zero degree to the flow and parallel to each other is the best configuration for VGs installation on present high speed train model. Spacing of the VGs should be good enough to get good performance. Very less spacing causes the vortices to diminish. Counter-rotating configurations, both convergent and divergent, do not work very well on present model of high speed train. Best results are obtained by using triangular VGs, followed by trapezoidal VGs and then rectangular VGs have their beneficial effect. It is also noted that drag reduction is maximum around VGs height of 20–25% of boundary layer thickness ( $0.2\delta-0.25\delta$ ) for present train model and further increase adds more viscous drag than reducing pressure drag. The length of VGs should be almost equal to boundary layer thickness in order to get maximum drag reduction. The designed VGs have created low pressure region at their location on train model but also created even more high pressure region further away from installation location, near separation point, which reattach the flow. This reattachment of flow cause the separation point to move downstream and aerodynamic drag is reduced. The present analysis shows that installation of VGs on high speed trains can save a lot of electricity consumption by high speed trains. A small reduction in high speed train drag matters, as they are heavy duty trains and millions of Kilowatt-hours (KWh) electricity can be saved every year by using well designed VGs on high speed trains.

## References

1. Hucho, W.H.: *Aerodynamics of Road Vehicles*, 4th edn. SAE International, Warrendale (1998)
2. Koike, M., Naga Yoshi, T., Hamamoto, N.: Research on aerodynamic drag reduction by vortex generators. *Mitsubishi Motors Tech. Rev.* **16**, 11–16 (2004)
3. Lin, J.C., Selby, G.V., Howard, F.G.: Exploratory study of vortex-generating devices for turbulent flow separation control. In: 29th Aerospace Sciences Meeting, Reno, Nevada, Paper 91-0042. AIAA (1991)
4. Rao, D.M., Kariya, T.T.: Boundary-layer submerged vortex generators for separation control – an exploratory study. In: *Space Programs and Technologies*, pp. 839–846 (1988)
5. Pearcey, H.H.: Shock induced separation and its prevention by design and boundary-layer control. In: *Boundary layer and flow control*, vol. 2, pp. 1166–344. Pergamon Press, New York (1961)
6. Shabaka, I.M.M.A., Mehta, R.D., Bradshaw, P.: Longitudinal vortices imbedded in turbulent boundary layers. Part 1. Single vortex. *J. Fluid Mech.* **155**, 37–57 (1985)
7. Mehta, R.D., Bradshaw, P.: Longitudinal vortices imbedded in turbulent boundary layers. Part 2. Vortex pair with “common flow” upwards. *J. Fluid Mech.* **188**, 529–546 (1988)
8. Robinson, S.K.: Coherent motion in the turbulent boundary layer. *Ann. Rev. Fluid Mech.* **23**, 601–639 (1991)
9. Orlandi, P., Jiménez, J.: On the generation of turbulent wall friction. *Phys. Fluids* **6**(2), 634–641 (1994)
10. Jiménez, J., Pinelli, A.: The autonomous cycle of near wall turbulence. *Fluid Mech.* **225**, 211–240 (1999)
11. Jacobi, A.M., Shah, R.K.: Heat transfer surface enhancement through the use of longitudinal vortices: a review of recent progress. *Exp. Thermal Fluid Sci.* **11**, 295–309 (1995)
12. Torii, K., Yanagihara, J.I.: The effects of longitudinal vortices on heat transfer of laminar boundary layers. *JSME Ser. II* **32**(3), 395–402 (1989)
13. Yanagihara, J.I., Torii, K.: Enhancement of laminar boundary layer heat transfer by a vortex generator. *JSME Ser. II* **35**(3), 400–405 (1992)
14. Gebhardt, C.G., Preidikman, S., Massa, J.C.: Numerical simulations of the aerodynamic behavior of large horizontal-axis wind turbines. *Int. J. Hydrogen Energy* **35**(11), 6005e11 (2010). <https://doi.org/10.1016/j.ijhydene.2009.12.089>
15. Ashill, P., Fulker, J., Hackett, K.: Research at DERA on sub boundary layer vortex generators (SBVGs). Presented at 39th AIAA aerospace sciences meeting and exhibit, paper 2001-0887. AIAA (2001)
16. Gao, L., Zhang, H., Liu, Y., Han, S.: Effects of vortex generators on a blunt trailing-edge airfoil for wind turbines. *Renew. Energy* **76**, 303e11 (2015). <https://doi.org/10.1016/j.renene.2014.11.043>
17. Becker, R., Garwon, M., Gutknecht, C., B€arwolff, G., King, R.: Robust control of separated shear flows in simulation and experiment. *J. Process. Control* **15**(6), 691e700 (2005). <https://doi.org/10.1016/j.jprocont.2004.12.001>
18. Xue, S., Johnson, B., Chao, D., Sareen, A., Westergaard, C.: Advanced aerodynamic modeling of Vortex generators for wind turbine applications. In: *European Wind Energy Conference (EWEC)*, Warsaw, Poland (2005)
19. Ahmed, H., Chacko, S.: Computational optimization of vehicle aerodynamics. In: *Annals of DAAAM for 2012 and Proceedings of the 23rd International DAAAM Symposium*, vol. 23, no. 1, pp. 313–318 (2012)
20. Jones, W.P., Launder, B.E.: the calculation of low-Reynolds-number phenomena with a two-equation model of turbulence. *Int. J. Heat Mass Transf.* **16**, 1119–1130 (1972)

21. Menter, F.R.: Two-equation eddy-viscosity turbulence models for engineering applications. *AIAA J.* **32**(8), 1598–1605 (1994)
22. Spalart, P.R., Allmaras, S.R.: A one-equation turbulence model for aerodynamic flows. *La Recherche Ae’rospatiale* **1**, 5–21 (1994)
23. Mohan Jagadeesh Kumar, M., Dubey, A., Chheniya, S., Jadhav, A.: Effect of vortex generators on aerodynamics of a car: CFD analysis. *Int. J. Innov. Eng. Technol. (IJJET)* **2**(1), 137–144 (2013)
24. Sujith, S.K., Reddy, R.G.: CFD analysis of sedan car with Vortex generators. *Int. J. Mech. Eng. Appl. Res. IJMEAR* **3**(3), 179–184 (2012)



# The Study on Extraction of Falling Rock Source Using Aerial Laser Data to Improve the Efficiency of Falling Rock Measures

Yuqing Zhang<sup>1</sup> (✉), Koki Sakita<sup>1</sup>, Satoshi Nishiyama<sup>1</sup>, and Takeharu Sato<sup>2</sup>

<sup>1</sup> Okayama University, Okayama, Japan  
pmqj60ko@s.okayama-u.ac.jp

<sup>2</sup> Okayama University of Science, Okayama, Japan

**Abstract.** Due to the continuous rainfall, concentrated rainstorm, earthquake and so on caused by the rainy season and typhoon, the accidents caused by falling stone from hillside to road occur frequently. From these accidents, the opportunity to devote to the cause of falling stone countermeasures is improving. In the cause of falling stone countermeasures, road disaster prevention inspection and field investigation play a very important role. Selection of the survey areas and conduction the field survey is important on the project of falling rock measures. However, it is concerned that oversight of falling rock sources and waste of time at field survey, because of the diagram that cannot express the earth surface correctly. Also, it is difficult to express all data in a diagram made by aerial laser surveying although it is good at expression of the earth surface properly. So, we made micro topography highlight map to express the change in terrain finely and emphasize the steep cliff by combining diagrams. In this study, we extracted falling rock source on the desk and survey the selected area by micro topography highlight map. In addition, we verify its result by point cloud data. As a result, we report that we were able to extract steep cliffs of 1.4 m or more in height and 60° or more in terms of angle.

## 1 Introduction

In recent years, due to the continuous rainfall, concentrated rainstorm, earthquake and so on caused by Plum rains period and typhoon, the accidents caused by falling stone from hillside to road occur frequently. In the cause of falling stone countermeasures, road disaster prevention inspection and field investigation play a very important role. Now, in order to select the place of road disaster prevention and inspection, the source of falling stone is extracted by aerial photo interpretation, but it is difficult to extract the source of falling stone from the aerial photo of lush vegetation. Therefore, it is a problem to omit the source of falling stone during inspection. In addition, due to the poor accuracy of the source of falling stone in the part of the subject, it may take a lot of time to carry out the investigation. As one of the methods to solve the problem, the manufacture of high precision drawings to capture the changes of micro terrain can be given. It can be considered that the efficiency of inspection and field investigation without omission and omission can be realized by extracting the location of the source of falling stone on the

table in advance. In this study, the steep terrain below altitude is defined as the source of falling stone. By confirming the consistency between the results of table extraction based on high precision drawings and the local results, the possibility of table extraction of the source of falling stone is verified.

## 2 Purpose and Research

Establish an efficient and accurate inspection method for the source of falling rock.

- Method: Aerial laser surveying and microtopographical emphasize analysis for laser data
- Map: Microtopograph highlight map
- Validation items and research contents:
  - (1) Extraction of target parts on desk by using current inspection record
  - (2) Field survey and confirmation the validity of the map
  - (3) Evaluation of the extracted target by using laser data

## 3 Measurement Method

### Utilization of Aeronautical Laser

- Three-dimensional measurement by the nonprism-lasersnan.
- Using a helicopter, the measurement point increase.
- Following processing is done on the data (Figs. 1 and 2).



**Fig. 1.** Imaging diagram of aeronautical laser measurement

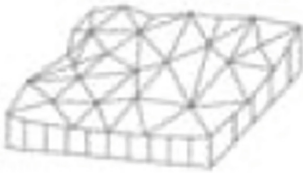


LiteMapper-6800-400		
Operating AGL	30-1600m	
Scan angle	45° ~60°	
Pulse rate	80,000Hz~400,000Hz	
Number of scans	10Hz~200Hz	
Beam diameter	0.5mrad	
Laser safety standard	Class3R	
Nominal ocular hazard area	>1.5m(NOHD),>10m(ENOHD)	
Measurable altitude	Pulse rate	Maximum operating AGL
	80,000Hz	1600m
	100,000Hz	1100m
	300,000Hz	950m
400,000Hz	800m	
Equipment	GNSS/IMU:IGI AEROcontrol- II, DigiCAM-50	



**Fig. 2.** Measuring helicopter

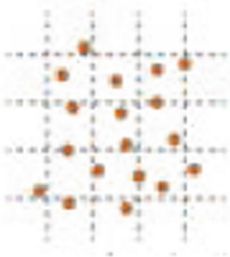
As a method of making high precision drawings to represent microtopography, aerial laser measurement is used. Aerial laser measurements can accurately capture the ups and downs of the surface even in the mountainous areas where the trees are located. In this study, the DEM data with 0.5 m interval are compiled from the aerial laser measurement data.



Terrain representation by TIN (Irregular triangle)



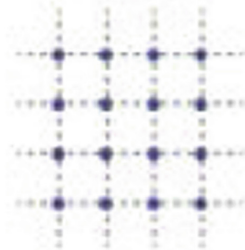
Terrain representation by Grid data



Random point cloud



Interpolation processing



Grid data

## 4 Map Overview

### Contour Map

Contour map is a curve on a map that draws a trajectory that connects to the same elevation (Fig. 3). In the dense performance, the oblique plane from the low angle to the middle angle is easier to understand, but because it cannot show the topographic change points between the contours, it is sometimes impossible to judge the micro-topography of the mountain path and so on.

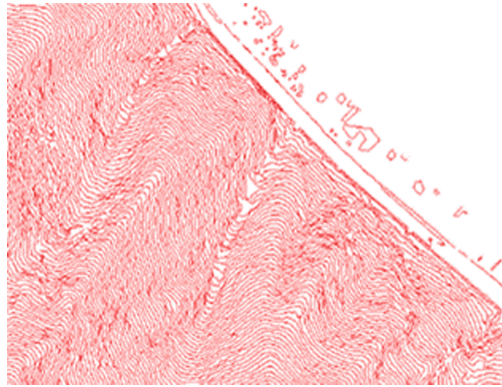


Fig. 3. Contour map

### Inclination-Amount Map

Inclination-amount map is an image that calculates the tilt of each pixel of the grid data and changes the brightness according to that value to represent the terrain (Fig. 4). This represents the tilting of the maximum tilt direction from the adjacent 9 points to the plane best described by the central point using the least square method (Fig. 5). The steep slope is bright (white) and the gentle slope is dark (black). The steep cliff can be extracted as the source of falling stone.

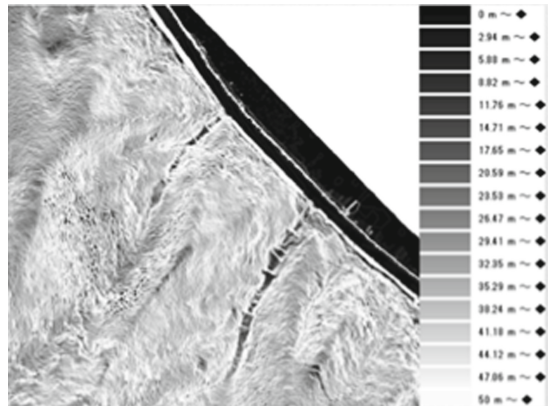


Fig. 4. Inclination-amount map

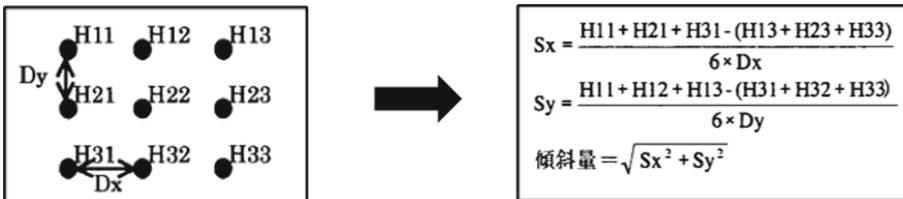
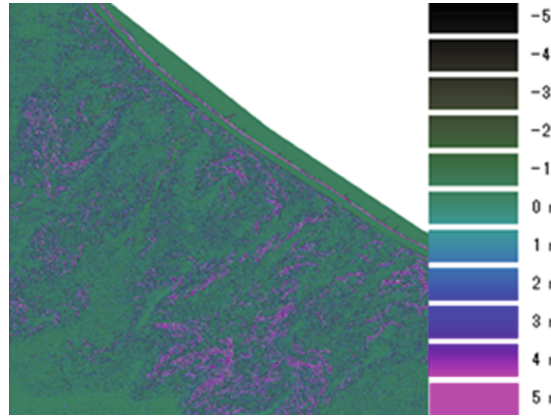


Fig. 5. Inclination-amount

**Laplacian Map**

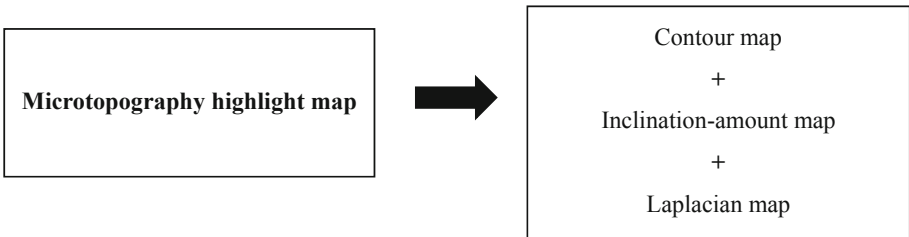
Laplacian map is an index to represent the concavity and convexity of terrain and the sharp change of tilt in grid data. Contrary to ridge valley degree, concave terrain is represented on the positive side (higher than around the target point) black, and convex terrain on the negative side (lower than around the target point) pink (Fig. 6).



**Fig. 6.** Laplacian map

**Microtopography Highlight Map**

In the microtopographic representation monomer, it is difficult to extract the source of falling stone.



- Each disadvantage will be supplemented
- Retaining the advantage of each maps (Fig. 7)

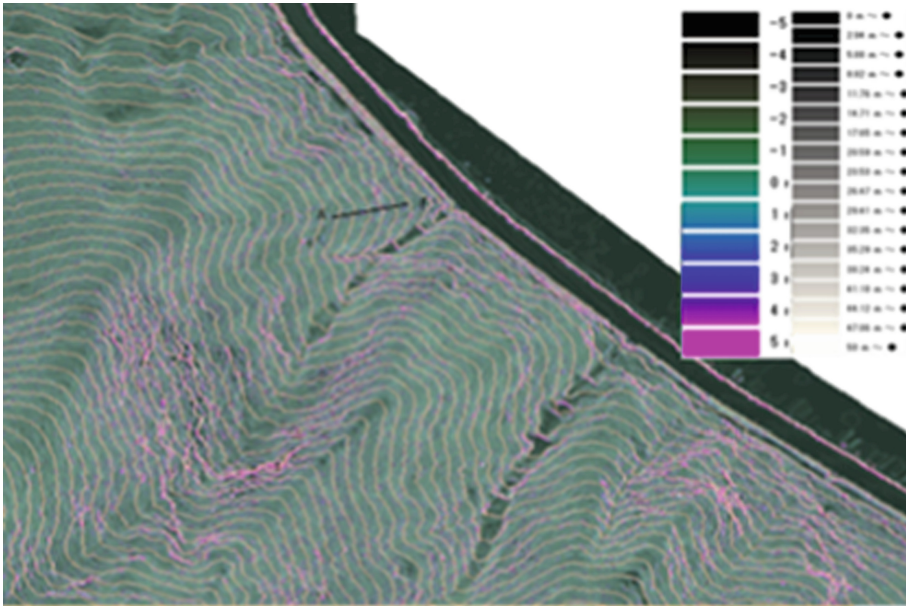


Fig. 7. Microtopography highlight map

## 5 Result

The survey site is near otukusawa, North District of Okayama, No. 53 General National Highway of Okayama (Fig. 8). In order to investigate the road to prevent falling stone, the area where the rock may fall directly from the slope is selected.



Fig. 8. Survey of land

### Extraction of Target Parts on Desk

Current inspection record were used as material for the extraction on the map (Fig. 9).

- Can create the map which express whole area.
- The reddish parts tended to mark as a target part.

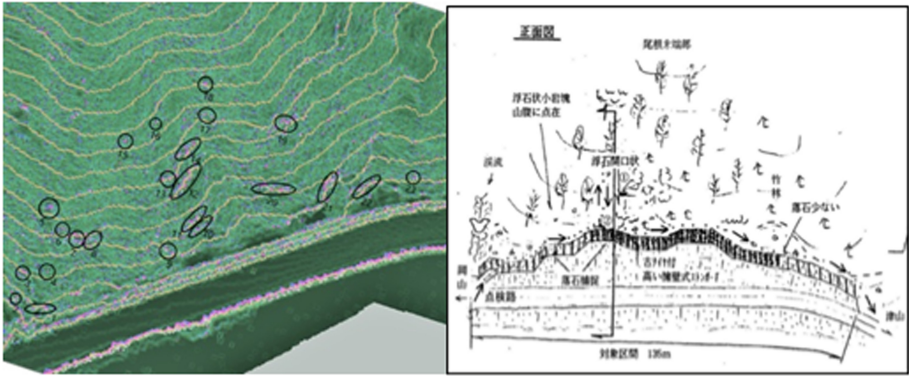
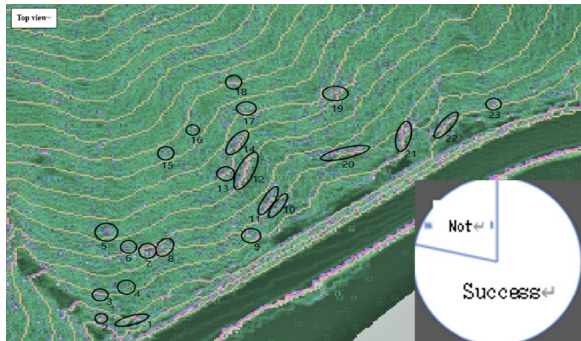


Fig. 9. Marked map. Current inspection record

**Field Survey and Confirmation on the Validity of the Map**

The images of the parts where each area corresponds to the individual survey result indicated in low right with color circle are shown.

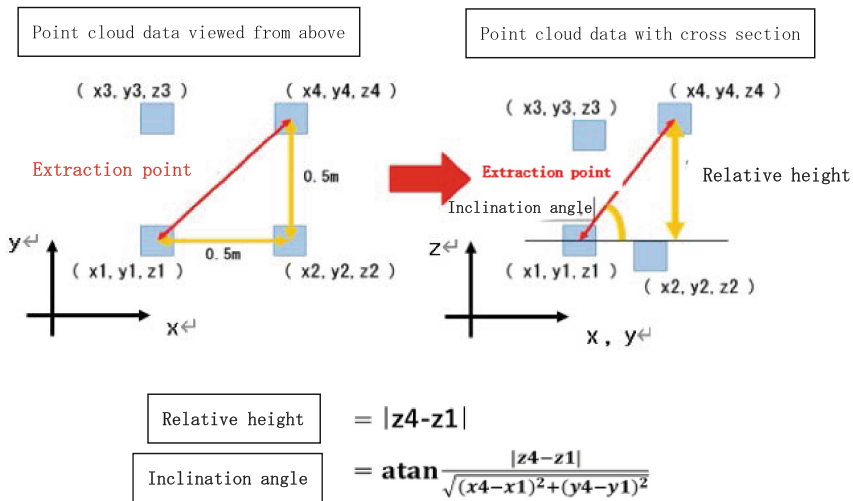


Number	Possibility of extraction	Investigation result
1	△	Stee slope
2	△	Stee slope
3	△	Hollow
4~17	○	Fallstone source
18	△	Hollow
19~22	○	Fallstone source
23	△	Valley

- Can extract the source of falling rock.
- Various terrain (steep slope or hollow) were extracted.

### Evaluation of the Extracted Target by Using Laser Data

We graphed the relationship between the relative height and inclination angle by using base laser data.



- The source of falling rocks more than 60° was extractable in the map.

## 6 Conclusion

The following conclusions were obtained.

- Can create drawings from the laser data that can see the whole of the target mountain.
- The created map can extract the source of falling rocks more than 60°.

## References

1. Kikuchi, T.: Akira Hartanto ceremony. In: Sendak, R., Nishiyama, S. (eds.) Development and Oyo of Fluctuation Vector Analysis Technology in the Landslide Place Where S—DEM Data Was Used, 57-6, pp. 277–288 (2017)
2. Kazuhiko, M., et al.: Development and the Topography of the Inner Water Flooding Assumption District Setting Technique by the Topographical Analysis Using Aerial Laser Measurement Data, 33-3, pp. 281–295 (2012)
3. Masashi, M., Masahumi, I., Takashi, M.T., Nishiyama, S.: Basic Inspection of Falling Rock Source Abstraction with 2 Periods of Different Aerial Edge Laser Data and the (69th Time) Japan Society of Civil Engineers Chinese Branch Meeting for Giving Papers Announcement Outline Collection in Fiscal Year 2017, p. 373 (2017)
4. Kaya, K., Sato, T.: The Rapurashian chart present technique in case of the mass movement geomorphic analysis and erosion control. Acad. J. **67**(1), 41–47 (2014)

# Author Index

## A

Abbasimaedeh, P., 44  
Aziz, Aqib, 95

## B

Bobade, Sudarshan, 58  
Bonelli, S., 44

## D

Dhawale, Arun, 58

## G

Gang, Chen, 95  
Garandet, A., 44  
Garg, Vaibhav, 58

## K

Kadam, Digvijay, 58  
Kimura, Yasumasa, 21

## L

Lamour, V., 44  
Lanmin, Wang, 9

## N

Nishiyama, Satoshi, 109

## P

Patil, N. K., 58

## R

Rong, Xu, 9

## S

Sakita, Koki, 109  
Sato, Takeharu, 109  
Saygili, Gokhan, 1  
Souliman, Mena I., 1  
Suzuki, Naoki, 21

## T

Tanoli, Afnan Younis, 80  
Tapase, Anand, 58  
Tatin, M., 44

## V

Vincent, H., 44

## W

Woolery, Edward W., 9

## Y

Yarrapureddi, Hari Kumar Reddy, 1  
Ye, Guan-lin, 80

## Z

Zhang, Yang, 95  
Zhang, Yuqing, 109